Smart needles for percutaneous interventions

Kirsten Henken

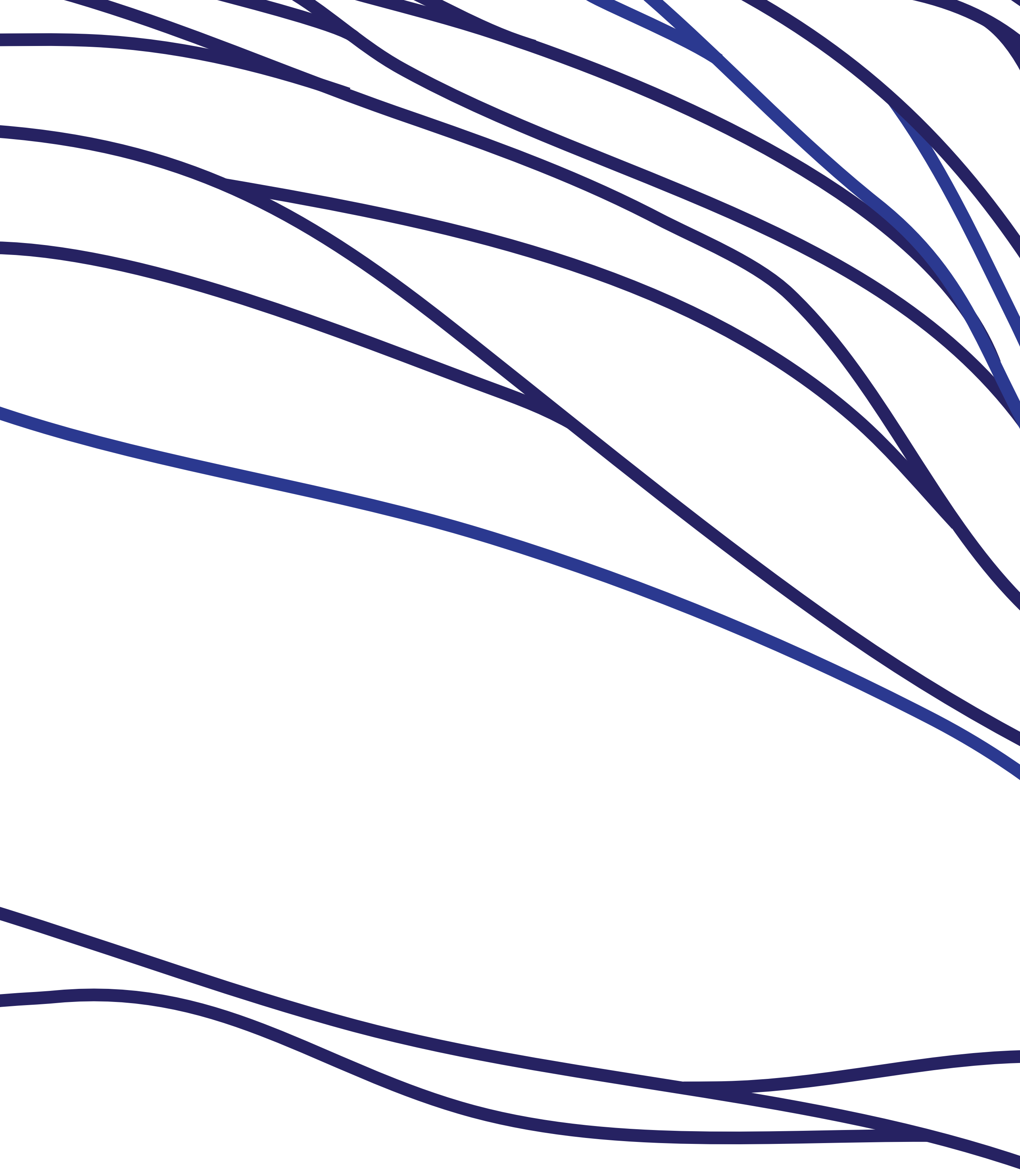

SMART NEEDLES FOR PERCUTANEOUS INTERVENTIONS

Proefschrift

ter verkrijging van de graad van doctor aan de Technische Universiteit Delft;

op gezag van de Rector Magnificus prof. ir. K.C.A.M. Luyben;

voorzitter van het College voor Promoties

in het openbaar te verdedigen op dinsdag 30 september 2014 om 15:00 uur

door

Kirsten Ruth HENKEN

werktuigbouwkundig ingenieur

geboren te Rotterdam

Dit proefschrift is goedgekeurd door de promotor:
prof. dr. J. Dankelman

Copromotor:
dr. J.J. van den Dobbelsteen

Samenstelling promotiecommissie:

Rector Magnificus,	voorzitter
prof. dr. J. Dankelman,	Technische Universiteit Delft, promotor
dr. J.J. van den Dobbelsteen,	Technische Universiteit Delft, copromotor
prof. dr. M.R. Cutkosky,	Stanford University
prof. dr. A.G.J.M. van Leeuwen,	Universiteit van Amsterdam
prof. dr. ir. R. Dekker,	Technische Universiteit Delft
prof. dr. W.J. Niessen,	Technische Universiteit Delft/Erasmus MC
dr. A. Moelker,	Erasmus MC
prof. dr. ir. P. Breedveld,	Technische Universiteit Delft, reservelid

Title: Smart needles for percutaneous interventions
Author: K.R.Henken (kirstenhenken@hotmail.com)

ISBN 978-94-6186-344-7

Table of contents

TABLE OF CONTENTS

Summary / Samenvatting

SUMMARY

The development of advanced needles for diagnostic and therapeutic purposes such as ablation and brachytherapy in the liver has offered minimally invasive therapies to patients that were previously untreatable. Nevertheless there is room for improvement regarding effectiveness and efficiency of these minimally invasive therapies. This thesis aims to contribute to these improvements and focuses on accurate placement of needles guided by magnetic resonance imaging (MRI) to maximize the effect of the treatment and to minimize unwanted side-effects. To this end, steerability is added to needles to provide active control of the needle trajectory and sensors are integrated to feedback spatial information for navigational purposes.

Needle steerability

The ability to actively steer the needle towards the target may improve endpoint accuracy and thereby optimize the clinical outcome. Chapter 2 and 3 focus on the design, optimization and evaluation of steerable needles that are compatible with MRI. The first prototype (Chapter 2) contains a steering mechanism consisting of cables and hinges that allows for adjustment of the orientation of the needle tip. The shaft of the needle is flexible and passively follows the trajectory of the needle tip. Experiments are executed to evaluate the relationship between steering angle applied at the tip and the resulting deflection of the needle. The results show that substantial steering can be achieved with this mechanism, but that the needle design needs to be adjusted to improve the directional control of steering.

Such improvement is implemented in the second prototype (Chapter 3). The hinges are replaced by compliant elements and the cables are integrated in grooves in the wall to avoid torsion. This prototype is designed to be compatible with and visible on MRI and has a handle that allows for manual control of the needle. Experiments are executed to validate the steerability of this second prototype. The possibility to control the needle path under MRI-guidance is evaluated by manually steering the needle to different targets in a gel phantom that was placed in the bore of the scanner. These experiments show that the trajectory of the needle can be adjusted after the needle has been inserted and that MRI sequences that are generally available for interventional procedures are able to visualize the needle and its tip. The steerable needle offers flexibility to the physician in control and choice of the needle path when navigating the needle towards the target position.

FBG-based needle tracking

Accurate targeting requires intra-procedural information about the needle tip position, particularly when the needle trajectory is curved. This information can be retrieved from

MR images, but real-time tracking at appropriate update rates is not feasible yet. In this work, shape sensing based on fiber Bragg grating (FBG) technology is investigated aiming at feeding back information about the position and orientation of the needle tip in real time. FBGs are strain sensors that are integrated in the core of an optical fiber and can be read out based on the wavelength they reflect.

Three fibers with multiple FBGs each need to be incorporated in a needle to allow for shape sensing. When the FBGs in the fibers are aligned with each other, strain is measured at three locations within one cross-section. Based on the strains measured by an FBG trio, the degree and direction of bending at this position can be reconstructed. The needle shape can then be reconstructed by interpolating the degree and direction of bending at the positions of the FBG trios and translating these to spatial coordinates along the needle. In Chapter 4, a first prototype for FBG-based shape sensing is presented together with the model for shape sensing. The prototype is a medical needle that contains three optical fibers with two FBGs each, which tip position can be determined with an accuracy of about 1 mm in 2-D.

Chapter 5 reports on the possibilities to optimize FBG-based shape sensing for needle tracking aiming at increased accuracy. The FBG-based shape sensing model is expanded and simulations are performed to quantify the effect of various design parameters on the position accuracy. Inputs that are investigated in the simulations include accuracy of wavelength measurement and sensor geometry as well as different sensor configurations and interpolation models. The simulations are validated with two new prototypes with different FBG configurations. The simulations show that the accuracy of FBG-based shape sensing of a needle can be in the order of 10% of the deflection at the tip, depending on the configuration. Tip deflections that are smaller than approximately 1 mm cannot be detected accurately.

Based on the findings of the simulations, a final prototype is built that contains five FBGs per optical fiber. The design of this prototype is presented in Chapter 6 together with the 3-D accuracy of FBG-based estimation of the tip position. The needle is inserted in a gelatin phantom, after which the outputs of the FBGs are measured and the needle shape is imaged with computed tomography (CT). A 3-D accuracy of <1 mm at the needle tip was determined by comparing the FBG-based shape with the shape retrieved from the CT scans.

A force sensor at the tip of the needle allows for the registration of the interaction between needle and tissue and may complement FBG-based shape sensing for navigational purposes. When an FBG is attached to the tip of the needle, the strain in the FBG is dependent on the stiffness of the needle and on the force that is exerted on the needle tip. Chapter 7 describes the design and evaluation of a needle with an FBG-based force sensor at the tip. The relation between the output of the FBG and the tip force is characterized at various temperatures. In addition, the needle is evaluated in vivo by inserting it in the liver of a porcine. When calibration and measurements are performed at the same constant temperature, the FBG is able to register peaks in the tip forces. The results also show that the magnitude of the FBG output is influenced by the mechanical properties of the supporting structure of the FBG in the needle as well as by the temperature. Solutions for compensation of the effect of temperature include adding an extra FBG.

Integration of steerability and shape sensing

Finally, steerability and shape sensing are integrated in a robotic system for needle steering in MRI-guided percutaneous interventions in the liver (Chapter 9). The master-slave system comprises a needle with a cable-actuated compliant tip to allow for readjustment of the orientation and steering angle, optical fibers with FBGs for the real-time measurement of needle shape, and a piezoelectric actuator unit to enable positioning of instruments within the MRI scanner. The driving mechanism to steer and to insert the needle is controlled by the physician through a master device. Visual feedback of the needle shape is provided based on the FBG measurements. Chapter 9 elaborates on the design of the system and on the validation of the system in a gelatin phantom.

Conclusion

The work presented in this thesis provides a framework for practical implementation of steerability and FBG-based shape sensing in needles that are controlled either manually or robotically. The main contribution of this work is the technological advancement of needles for percutaneous interventions. Future work should aim at the translation of these developments to clinically relevant devices as well as at integration of the devices in the clinical workflow. Development of practicable instruments and methods is vital for successful implementation in clinical practice. The work presented in this thesis will aid in achieving spot-on targeting and optimal therapeutic results in percutaneous liver interventions in the future.

SAMENVATTING

De ontwikkeling van geavanceerde naalden voor diagnose of behandeling van aandoeningen in de lever (bijvoorbeeld ablatie en brachytherapie) biedt behandelingsmethoden aan patiënten die eerder niet behandeld konden worden. Desalniettemin is er ruimte voor verbetering op het gebied van effectiviteit en efficiëntie van deze minimaal invasieve interventies. Het doel van dit proefschrift is een bijdrage te leveren aan deze verbeteringen. De focus ligt op het verhogen van de nauwkeurigheid waarmee de naalden geplaatst worden aan de hand van magnetic resonance imaging (MRI), zodat het effect van de behandeling maximaal is en ongewenste bijeffecten worden geminimaliseerd. Met dit doel voor ogen is de mogelijkheid tot sturen toegevoegd, zodat het pad dat de naald aflegt actief beïnvloed kan worden. Daarnaast zijn sensoren in de naald geïntegreerd om ruimtelijke informatie over de naaldvorm en -positie aan te bieden ten behoeve van de navigatie.

Stuurbare naalden

De eindpuntnauwkeurigheid -en daarmee het succes van de behandeling- kan wellicht verbeterd worden wanneer de naald actief gestuurd kan worden. Hoofdstuk 2 en 3 beschrijven het ontwerp, de optimalisatie en de evaluatie van stuurbare naalden die compatibel zijn met en zichtbaar op MRI. Het eerste prototype (Hoofdstuk 2) heeft een stuurmechanisme dat bestaat uit kabels en scharnieren waarmee de oriëntatie van de tip van de naald aangepast kan worden. De schacht van de naald is passief flexibel en volgt de richting van de tip. De relatie tussen de stuurhoek aan de tip en de resulterende afwijking van de naald is experimenteel bepaald. Het is mogelijk om een substantiële deflectie te introduceren met dit stuurmechanisme, maar het ontwerp van de naald moet worden verbeterd om volledige controle over de richting van sturen te verkrijgen.

Deze aanpassing is geïmplementeerd in het tweede prototype (Hoofdstuk 3). De scharnieren zijn vervangen door compliante elementen en de kabels lopen door groeven in de wand van de naald om torsie te voorkomen. Dit prototype is speciaal ontwikkeld voor gebruik in MRI en heeft een handvat waarmee de stuurhoek aan de tip handmatig kan worden opgelegd. Wederom zijn experimenten uitgevoerd om de stuurbaarheid van dit prototype te evalueren. Daarnaast is onderzocht of het mogelijk is om het pad van de naald te regelen onder begeleiding van MRI. Hiervoor is de naald handmatig naar targets in een gelatine fantoom gestuurd, terwijl het fantoom in de buis van de scanner geplaatst was. Deze experimenten illustreren dat het pad van de naald aangepast kan worden, nadat de naald is ingebracht en dat de naald duidelijk gevisualiseerd kan worden met courante MRI sequenties. De stuurbare naald biedt flexibiliteit aan de arts, zodat het pad vrij gekozen en aangepast kan worden tijdens het navigeren naar de target positie.

Positiebepaling van de naald met FBGs

Informatie over de positie van de tip van de naald is onmisbaar tijdens de procedure om de target met hoge nauwkeurig te bereiken, vooral wanneer het pad van de naald gekromd is. Deze informatie zou uit MRI beelden gehaald kunnen worden, maar het is nog niet mogelijk om dit zonder vertraging en op hoge snelheid te doen. Dit proefschrift onderzoekt de mogelijkheid om de vorm van de naald te reconstrueren met behulp van fiber Bragg grating (FBG) technologie, zodat deze als informatie over de positie en oriëntatie van de tip van de naald teruggekoppeld kan worden aan de gebruiker. FBGs zijn reksensoren die in de kern van een optische fiber verwerkt zijn en kunnen uitgelezen worden aan de hand van de golflengte die ze weerkaatsen.

Vormbepaling vereist de integratie van minstens drie optische fibers met elk meerdere FBGs. De rek wordt gemeten op drie verschillende plaatsen in een enkele doorsnede wanneer de FBGs in de verschillende fibers met elkaar zijn uitgelijnd. De mate en richting van buiging op de locatie van deze doorsnede kunnen worden gereconstrueerd op basis van de drie rekmetingen in de FBGs. De vorm van de naald kan daarna bepaald worden door de mate en richting van buiging te interpoleren en deze te vertalen naar ruimtelijke coördinaten op de naald. In Hoofdstuk 4 is een eerste prototype met optische fibers voor vormbepaling met FBGs gepresenteerd. Dit hoofdstuk beschrijft ook het bijbehorende model voor vormbepaling. Het prototype bestaat uit een medische naald met drie optische fibers met elk twee FBGs. De tippositie van deze naald kan bepaald worden met een nauwkeurigheid van ongeveer 1 mm in 2-D.

Hoofdstuk 5 rapporteert over de mogelijkheden om vormbepaling met FBGs te optimaliseren voor een hogere nauwkeurigheid van de positiebepaling van de naald. Het model voor vormbepaling met FBGs is verder uitgewerkt en simulaties zijn uitgevoerd om het effect van verschillende ontwerpparameters op de eindpuntnauwkeurigheid te kwantificeren. De onderzochte parameters zijn onder andere de nauwkeurigheid waarmee de door de FBGs gereflecteerde golflengte wordt gemeten, de nauwkeurigheid waarmee de geometrie van de naald en de sensors bepaald is, de configuratie van de fibers en de interpolatiemethode. Deze simulaties zijn gevalideerd aan de hand van twee verschillende prototypes. De resultaten laten zien dat de nauwkeurigheid waarmee de vorm van de naald gereconstrueerd kan worden afhankelijk is van de precieze configuratie van de sensoren en in de orde van grote van 10% van de afwijking aan de tip valt.

Een laatste prototype met vijf FBGs per optische fiber is gemaakt op basis van de bevindingen in de simulaties. Het ontwerp van dit prototype is beschreven in Hoofdstuk 6, samen met de nauwkeurigheid van vormbepaling in 3-D. De naald is in een gelatine fantoom geprikt, waarna de output van de sensoren is gemeten en een scan van het geheel is gemaakt met behulp van computed tomography (CT). Een nauwkeurigheid van minder dan 1 mm in 3-D is bepaald door de vorm van de naald bepaald op basis van de FBG metingen te vergelijken met de vorm van de naald verkregen uit de CT scans.

Een krachtsensor aan de tip van een naald biedt de mogelijkheid om de interactie tussen de naald en het weefsel vast te leggen. Zo'n sensor zou de vormbepaling kunnen aanvullen ten behoeve van de navigatie naar de target. De rek in een FBG is afhankelijk van de stijfheid van de naald en van de kracht die aangrijpt op de naald wanneer deze is vastgemaakt aan de tip van de naald. Hoofdstuk 7 beschrijft het ontwerp en de evaluatie van een naald met een FBG-krachtsensor aan de tip. De relatie tussen de output van de FBG en de tipkracht is gekarakteriseerd bij verschillende temperaturen. Daarnaast is het in vivo functioneren van de naald onderzocht door hem in de lever van een varken te prikken. Deze experimenten laten zien dat het mogelijk is om piekkrachten te detecteren, als de kalibratie en de metingen zijn uitgevoerd op dezelfde temperatuur. Daarnaast lijkt de grootte van de output van de FBG beïnvloed te worden door de mechanische eigenschappen van de constructie rondom de FBG en door de temperatuur. Een extra FBG kan als referentie dienen om te compenseren voor het verstorende effect van temperatuur.

Integratie van stuurbaarheid en positiebepaling

Tenslotte zijn de mogelijkheid tot sturen en de positiebepaling met FBGs geïntegreerd in een robotisch systeem voor percutane MRI-geleide naaldinterventies in de lever (Hoofdstuk 9). Het master-slave systeem bestaat uit een stuurbare naald met FBGs voor vormbepaling. Piezo-elektrische actuatoren sturen de kabels aan waarmee de oriëntatie van de tip wordt aangepast. De actuatoren worden aangestuurd door de arts via een master systeem. Een visualisatie van de naaldvorm gebaseerd op de FBG metingen wordt teruggekoppeld aan de arts. Hoofdstuk 9 gaat dieper in op het ontwerp van het systeem en de bijbehorende validatie in een gelatine fantoom.

Conclusie

Het onderzoek in dit proefschrift biedt een raamwerk voor de praktische implementatie van stuurbaarheid en vormbepaling met FBGs in naalden met een handmatige of robotische interface. De belangrijkste bijdrage van dit onderzoek is de technologische innovatie van naalden voor percutane interventies. Toekomstig werk zou toegespitst moeten zijn zowel op de vertaling van deze ontwikkelingen naar klinisch relevante instrumenten als op de integratie van deze instrumenten in de praktische gang van zaken in het ziekenhuis. Het onderzoek in dit proefschrift zal in de toekomst bijdragen aan het nauwkeurig bereiken van de target om optimale resultaten te boeken in percutane interventies in de lever.

1

Introduction

1.1 MOTIVATION FOR THIS THESIS

The first reports on the use of needles for medical purposes date back to 1853 in which Alexander Wood [1] and Charles Gabriel Pravaz [2] independently aimed at the administration of narcotics in a patient's vein. After that, only small refinements have been made to the original design of the needles in order to increase safety and efficacy. Over the years, a range of needles varying in size, shape and material dedicated to specific percutaneous[1] interventions has been developed. Today needles are used for regular purposes including blood sampling and vaccination as well as for advanced diagnostic (e.g. biopsy) and therapeutic (e.g. brachytherapy[2]) interventions. The target sites of these interventions can be located anywhere in the body, varying from superficial veins in case of blood sampling to deep-seated areas such as the liver.

The liver is an organ that is tucked away in the abdominal area, just below the lungs and the diaphragm, protected by the ribs (Figure 1.1) [3]. The liver plays a major role in metabolism and has many functions, including detoxification, production of proteins, and storage of energy and vitamins. Cancer of the liver is the fifth most commonly diagnosed cancer and the second most deadly form of cancer for men worldwide [4]. The diagnosis is usually made based on imaging (Figure 1.2) with ultrasound (US), computed tomography (CT), and/or magnetic resonance imaging (MRI), which is sometime supplemented by a biopsy [5]. The majority of the patients is ineligible for the preferred treatment (i.e. surgical resection[3]), because of the advancement of the disease. Liver transplantation is the second option, but unfortunately donor shortage sets limits to its application. Therefore, multiple other therapies are currently applied in clinical practice or discussed in literature to provide palliative treatment to patients who are ineligible to surgical resection or to bridge the time to transplantation [5, 6]. These interventions include locoregional[4] treatments such as ablation[5], trans-arterial chemoembolization[6], and internal radiotherapy as well as systemic treatments. A selection of these treatments are effected through percutaneous needle insertion, such as radiofrequency ablation[7], cryoablation[8], microwave ablation[9] and brachytherapy. An example of a needle that is used for radiofrequency ablation in the liver is presented in Figure 1.3.

---

1 Percutaneous: affected through the skin
2 Brachytherapy: a form of radiotherapy in which sealed sources of radioactive material are inserted temporarily into body cavities or directly into tumors
3 Surgical resection: removal of all or part of an organ, tissue, or structure through surgery
4 Locoregional: limited to a localized area
5 Ablation: removal of a body part or the destruction of its function, as by a surgery, disease, or noxious substance.
6 Trans-arterial chemoembolization: injection of chemotherapeutic agents and/or inert particles into tumor vessels administered throughan artery
7 Radiofrequency ablation: the removal of tissue by heating it with a radiofrequency current passed through a needle electrode
8 Cryoablation: the removal of tissue by destroying it with extreme cold
9 Microwave ablation: the removal of tissue by destroying it with electromagnetic microwa

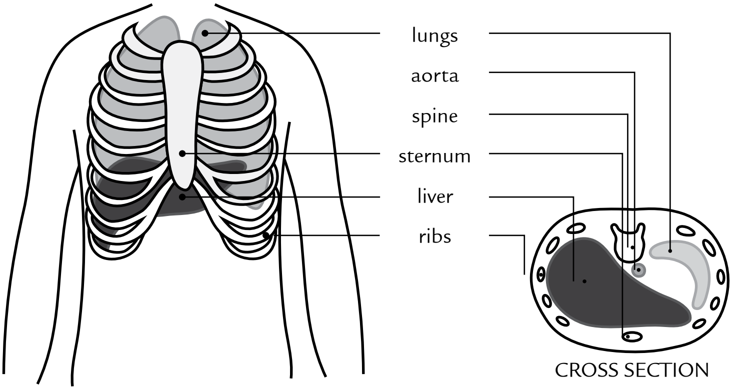

FIGURE 1.1 **Positioning of the liver in the human body.**

Accurate positioning of the needle tip is essential in these interventions to maximize their therapeutic effect and to minimize the damage to surrounding tissue, especially when essential structures (vessels or nerves) are in the vicinity of the target [7, 8]. However, accurate positioning is complicated by tissue deformation and unpredictable needle deflection during insertion due to tissue inhomogeneity and needle asymmetries [9-12]. Once the point of insertion and the initial orientation of the needle have been selected, the pathway of the needle is mainly determined by the interaction between the needle and the tissue. Undesired deviations from the intended trajectory may be corrected through manipulation of the needle orientation at the point of insertion. When the needle does not reach its target with sufficient accuracy, the needle has to be removed and reinserted. Therefore, needle placement is usually an iterative process in which the needle is advanced little by little, while it is imaged in real-time or in between each advancement.

Needle insertion in the liver is guided by US, CT or MRI [13]. US is widely used, because of its high contrast and ease of use, because the systems are mobile and the field of interest can be adjusted manually by positioning and orienting the probe. However, US only provides a 2-D view with limited spatial resolution, which makes imaging of the needle and the target at the same time difficult. Visualization of the liver is further complicated

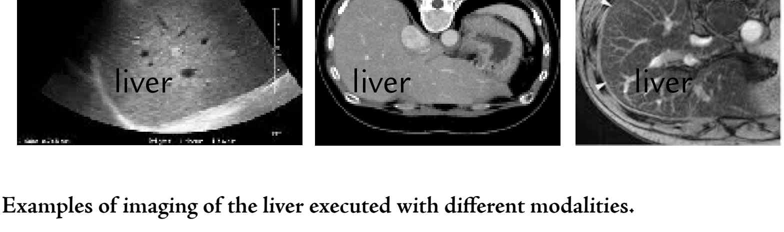

FIGURE 1.2 **Examples of imaging of the liver executed with different modalities.**

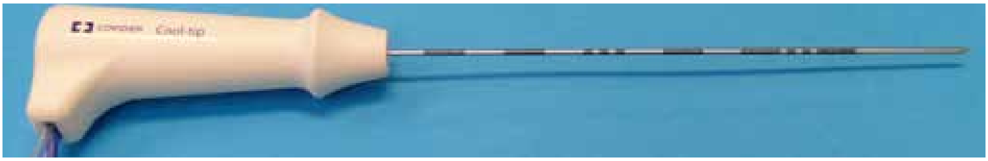

FIGURE 1.3 Example of a needle for radiofrequency ablation in the liver (15 cm/14 G).

because the ribs and the lungs obstruct the view. CT provides the possibility to make 3-D scans with high spatial accuracy and is not affected by bony structures or air. The contrast in soft tissue can be increased by fluoroscopy. Disadvantages are the limited working space in the bore of the scanner and the radiation burden to patient and professionals. In practice, the patient is moved in and out of the scanner multiple times, before the target has been reached. MRI is able to image soft tissue and the effect of the treatment with excellent contrast without using ionizing radiation. Besides that, MRI is highly flexible regarding the field of view and orientation of the images. Still, MRI is seldom used to guide percutaneous needle interventions in clinical practice due to the lack of dedicated imaging sequences and instruments that are usable in the MRI environment.

The introduction of needles for ablation and brachytherapy in the liver has offered minimally invasive therapies to patients that were previously untreatable, but there is still room for improvement regarding effectiveness and efficiency of these therapies. One of these improvements focuses on accurate placement of the needles to maximize treatment effect and minimize undesirable side-effects. Active control of the needle trajectory increases the placement accuracy of the needle. Additionally, extensive information about the needle tip position and its interaction with the surrounding tissue may increase intervention efficiency, and can partially be provided by means of MRI. This thesis aims to contribute to the improvement of the needles for MRI-guided interventions in the liver.

1.2 RECENT DEVELOPMENTS IN LITERATURE

1.2.1 Needle steering

Controlling the needle trajectory calls for a mechanism to steer the needle in the desired direction. Three categories of needle trajectory control approaches have been suggested previously: base manipulation; telescopic mechanism; and needle asymmetries. The principles of these steering strategies are visualized in Figure 1.4 and further discussed below.

The idea of base manipulation is to orient the needle tip in the desired direction by applying moments at the handle of the needle. Dimaio and Sulcudean [14] present a

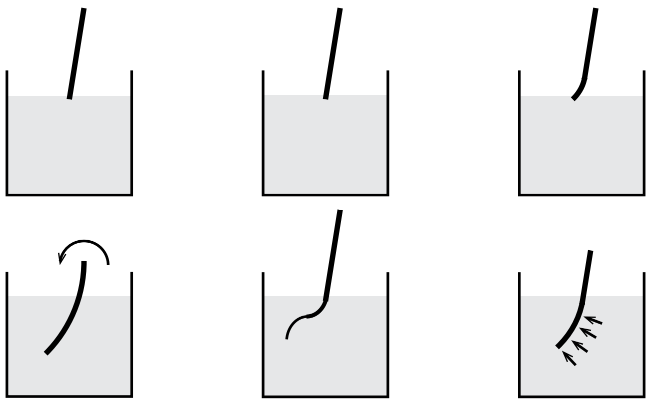

FIGURE 1.4 **The three main mechanisms for needle steering. In base manipulation, the orientation of the tip is adjusted by applying moments at the handle of the needle. In the telescopic mechanism, multiple precurved tubes are inserted through each other to create the desired needle shape. In the last mechanism, steering of the needle is initiated by the asymmetry of the forces that act on the needle tip.**

robotic system together with a corresponding model for control purposes that steers a medical needle to the target by means of base manipulation. Glozman and Shoham [15] suggest a similar system, but with a different model for planning of the trajectory and the required manipulation, aiming at a reduced computational time to allow for closed loop control. It has been argued if the strategy of base manipulation still works when the needle is further inserted without inflicting tissue damage at the incision point [16]. Highly accurate manipulation at the base is required to obtain the desired or planned trajectory.

The telescopic needles consists of multiple coaxial, precurved tubes that run through each other. The position and the orientation of the needle tip can be controlled by extrusion and rotation of the individual pre-curved tubes. Two different robotic systems consisting of three coaxial precurved tubes are presented in [17] and [18]. A large variety of trajectories can be obtained with such a needle, but the actual pathway depends to a large extent on the stiffness of the penetrated tissue, which makes it more suitable for applications in open space. In addition, not all steering actions are safe, for example, when the inner tube is completely extruded, rotation of this part is no longer an option, because it would result in large forces that could lead to tissue damage. Okazawa et al. [19] present a more simple design that is based on an existing biopsy needle and that consists of a rigid tube and a precurved probe. Actuation is either performed manually via a mechanical transmission or robotically.

The third steering strategy (i.e. needle asymmetry) utilizes the inherent steering effect of asymmetries of the needle tip (e.g. beveled and precurved tips). Webster et al. [20] present a robotic system that relies on needle bending introduced by a bevel tip. However, Majewicz et al. [21] suggest that a bevel tip does not induce sufficient needle deflection during insertion to be clinically relevant with respect to steering. A precurved tip does induce significant steering without increasing the load to the tissue or introducing damage. The degree of bending is dependent on the stiffness of the needle, the degree of asymmetry at the tip, the insertion speed, and the mechanical properties of the penetrated tissue [21, 22]. Although the steering abilities of a precurved tip are evident, controlling the steering motion with such needles is not straightforward. Several authors [23-25] suggest to combine duty-cycling with a precurved needle tip to allow for a variable degree of bending, assuming that a straight path is obtained when the needle is continuously rotated around its longitudinal axis.

The asymmetric needles that are discussed above require indirect control of the trajectory by adjusting the insertion speed and rotating the needle, since the properties of the asymmetry cannot be changed. As an alternative to this, asymmetric needles have been presented, of which the curvature of the bend and its orientation can be controlled directly. An example is a needle that consists of two interlocking segments that slide along each other, while the extremities of the two segments are connected to each other, much like the locking mechanism in a zip-lock bag [26, 27]. A forward motion of one of the segments induces a backward motion of the other segment, which will result in a curved shape. The advantage of needles of which the curvature and orientation can be controlled directly is that no rotation is required to adjust the needle trajectory. These needles may limit tissue damage and allow for intuitive manual control.

1.2.2 Tracking of needles in MRI

Magnetic resonance imaging (MRI) allows for visualization of anatomy and physiological function of the human body. MRI scans are made by subsequently aligning hydrogen atoms in the body through the application of a magnetic field, flipping the spinning direction of the hydrogen atoms by applying a radiofrequency pulse, and measuring change of the radiofrequency signal emitted by the hydrogen atoms during relaxation. MRI has excellent contrast in soft tissue and does not use ionizing radiation for imaging. Besides this, scanning planes and orientations can be freely chosen in MRI. A drawback of MRI is that the strong magnetic field limits the use of ferromagnetic materials in the vicinity of the scanner and of long conductors in the scanner.

Several methods to track equipment in MRI-guided interventions have been researched [28]. These methods either rely on the imaging system itself or on an external system that is dedicated to tracking of the needle. Tracking based on the imaging system can be passive or active. Passive tracking relies on the artefact[10] that is introduced by the instrument itself and active tracking on a coil that is integrated in the instrument. Passive tracking can be enhanced by incorporating materials in the needle that create a larger artefact with higher contrast. Passive tracking is limited to visualization of the instrument and does not quantify its position in space, whereas active tracking results in information about the position of the instrument tip and its orientation in case multiple coils are incorporated. Both methods are limited by the update frequency of the MRI.

Spatial information about the instrument can also be provided by a separate external or internal tracking system. In an external referencing system consisting of multiple cameras, light-emitting or reflecting markers that are mounted on the handle of the instrument are localized. Such a system can only detect markers that are positioned within the field-of-view of the cameras. Information about the tip of the instruments is therefore based on the inaccurate assumption that the needle remains completely straight during insertion. Information about the shape of the instrument can only be obtained based on sensors that are integrated in the instruments, such as strain sensors. Small electrical strain gauges can be added to a needle for this purpose [29], but the electrical circuit interferes with the MRI. Alternatively, optical sensing, for example with fiber Bragg gratings can be applied.

A fiber Bragg grating (FBG) is a grid etched in the core of an optical fiber [30, 31]. When a broad spectrum of light is introduced in the fiber, the FBG reflects one wavelength that corresponds to the period of the grid (Figure 1.5). When the fiber is strained at the location of the FBG, the period of the FBG and consequently the wavelength it reflects change, as a result of which an FBG functions as an optical strain sensor. Multiple FBGs can be incorporated in a single optical fiber that has a typical diameter of 250 μm. Unlike electrical strain gauges, FBGs do not require an electrical circuit, because the fiber acts as both the sensing element and the signal propagation conduit. These advantages make FBGs ideal candidates for integration in small medical equipment such as needles. However, optical fibers are usually made of glass, which is vulnerable because of its brittleness. Besides that, FBGs have a cross-sensitivity to temperature. These two factors call for a sophisticated design and manufacturing process in order to create an accurate sensor.

FBGs have been applied in various fields [32], including health monitoring of civil structures [33] and strain measurements in composite structures [34]. An overview of the use of FBGs in the medical field is provided in [35]. Medical applications include strain sensing in the musculoskeletal system, detection of physiological parameters (e.g. chemical concentration, pressure, temperature), monitoring of the effect of treatments such as high-intensity focused ultrasound, and many more. Application of FBGs for the purpose of tracking of medical devices through shape and force sensing has also been suggested.

---

[10] Artefact: distortion or fuzziness of an image caused by manipulation

FBG-based shape sensing systems typically comprise three optical fibers with multiple FBGs each. When the FBGs in the fibers are aligned with each other, strain is measured at three locations within one cross-section, based on which the curvature of the device at that location can be determined. The shape of the device and the corresponding position in space is reconstructed by combining the curvatures at the locations of the FBGs. Shape sensing based on FBGs has previously been integrated in endoscopes [36-38], laparoscopic tools [39], and needles [40-42]. However, extensive research on the implementation of shape sensing in clinical practice is lacking.

FBG-based force sensing may also be able to provide information about the location through identification of the mechanical properties of the punctured tissue type. When an FBG is attached to the tip of the needle, the strain in the FBG is dependent on the stiffness of the needle and on the force that is exerted on the needle tip. The force acting on the needle tip is introduced by the mechanical interaction with the punctured tissue and relates to the tissue-specific stiffness and toughness [43]. Once multiple optical fibers are integrated in a needle for the purpose of shape sensing, it is relatively straightforward to add FBG-based force sensing, because multiple FBGs can be incorporated in a single fiber. For example, in [44] an FBG is incorporated in the tip of an ablation catheter to measure if the catheter has punctured the cardiac wall. FBGs have also been integrated in tools for retinal surgery in order to measure the interaction forces between the instruments and the tissue [45, 46]. Finally, shape sensing has been combined with force sensing in a biopsy needle that is compatible with MRI [47].

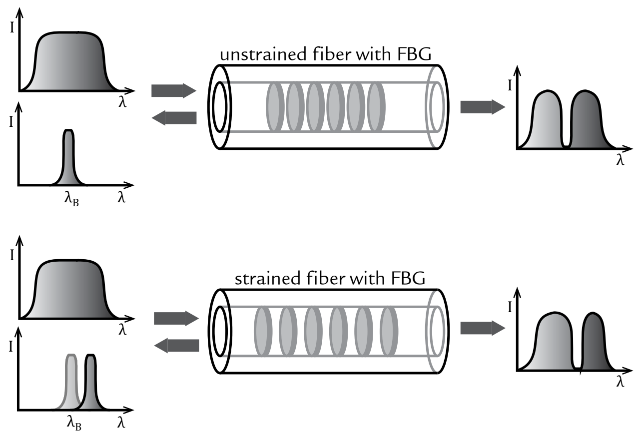

FIGURE 1.5 Working principle of a fiber Bragg grating (FBG). From the broad spectrum of light with intensity (I) that is introduced in the fiber, one wavelength (λ_B) is reflected by the FBG. When the fiber is strained, the reflected wavelength changes accordingly.

1.3 AIM

The aim of this thesis is to develop 'smart needles' by improving the needles that are used for percutaneous interventions in the liver. These smart needles will allow for dexterous navigation for accurate targeting. More specifically, the goals are:

I. To develop steerable needles that are compatible with MRI, so that the pathway of the needle can actively be adjusted during needle insertion, while local high-contrast images are obtained with MRI.
II. To develop sensorized needles for spatial tracking and tissue characterization to provide information about the needle position and the mechanical interaction with the tissue that the needle encounters during insertion.
III. To integrate steerability and sensors in a robotic needle insertion system that operates while the patient is situated in the scanner. Such a system supports the physician in accurate needle positioning and allows for continuous imaging of the target during insertion.

1.4 CONTENT, CONTRIBUTIONS AND OUTLINE

The chapters of this thesis are independent articles, which have previously been published in scientific journals or are currently under review. Because of this, the content of individual chapters is partly overlapping. Some chapters are supplemented with additional data, a more extensive explanation, or recent developments.

The key contents of this thesis are summarized as follows.

Design, optimization and evaluation of steerable needles that are compatible with MRI. A total of three prototypes were fabricated.
- Chapter 2 presents the first prototype and its evaluation. This prototype contains a steering mechanism with which the distal section of the needle can be oriented in different directions through a combination of cables and hinges. Evaluation of the steerability of this prototype shows that extensive steering can be achieved with this steering mechanism, although a number of improvements are needed to ensure optimal functioning.
- These improvements are implemented in the second prototype, which is presented in Chapter 3. This prototype is designed to be compatible with MRI and has a handle that allows for manual control of the needle. Experiments in the MRI show that the trajectory of the needle can be adjusted after the needle has been inserted.

Design, optimization and evaluation of FBG-based shape sensing needles. The purpose of shape sensing is to provide information about the position and orientation of the needle tip to the physician and/or to the controller of a robotic system.

- The first prototype of a shape sensing needle is discussed in Chapter 4. This prototype is a medical needle that contains three optical fibers with two FBGs in each needle. The needle tip position can be determined with an accuracy of about 1 mm in 2-D
- Chapter 5 reports on the possibilities to optimize FBG-based shape sensing in order to increase this accuracy. Possibilities that are investigated include optimization of the shape sensing model, an increased number of FBGs, optimization of the positions of the FBGs, and a calibration method.
- Based on the findings in this chapter, a second prototype is built that contains five FBGs per optical fiber. The design of this prototype is presented in Chapter 6 together with 3-D accuracy that is determined in a clinical setting.

Design and evaluation of a needle with an FBG-based force sensor. Tissue that is encountered during needle insertion can be characterized based on the force it exerts on the needle. Chapter 7 describes the design of a needle, which tip is equipped with an FBG to the end of force sensing. The challenges in FBG-based force sensing are discussed as well.

- The integration of a steerability and shape sensing in an MRI compatible robotic system for needle steering in percutaneous interventions in the liver. Such a system aims at remote control of a steerable needle to allow for treatment of a patient that is situated in a scanner. Chapter 8 elaborates on the development and evaluation of a robotic system.

This thesis is concluded by Chapter 9 with a discussion of the work presented in Chapter 2 to 8 together with a general conclusion and recommendation for future work.

REFERENCES

[1] Wood A. *Addresses and papers read at the twenty-sixth annual meeting of the British Medical Association: Treatment of neuralgic pains by narcotic injections.* Brit Med J. 1858; 1(87): 721.

[2] Pravaz CG. *Sur un nouveau moyen d'operer la coagulation du sang dans les arteres, applicable a la guerison des aneurismes.* Compt Rend Acad. 1853; 36: 88-89.

[3] Marieb EN, Hoehn K (2007). *Human anatomy and physiology.* Pearson Education.

[4] Jemal A, Bray F, Center MM, Ferlay J, Ward E, Forman D. *Global cancer statistics.* CA-Cancer J Clin. 2011; 61(2): 69-90.

[5] Forner A, Llovet JM, Bruix J. *Hepatocellular carcinoma.* Lancet. 2012; 379(9822): 1245-1255.

[6] King AJ, Breen DJ. Understanding the current status of image-guided ablation for metastatic colorectal disease. Abdom Imaging. 2013; 38(6): 1234-1244.

[7] Khlebnikov R, Muehl J. *Effects of needle placement inaccuracies in hepatic radiofrequency tumor ablation.* 32nd Annual International Conference of the IEEE EMBC, Argentina, Buenos Aires, 2010.
[8] Kunzli BM, Abitabile P, Maurer CA. *Radiofrequency ablation of liver tumors: Actual limitations and potential solutions in the future.* World J Hepatol. 2011; 3(1): 8-14.
[9] Abolhassani N, Patel R, Moallem M. *Needle insertion into soft tissue: A survey.* Med Eng Phys. 2007; 29(4): 413-431.
[10] Blumenfeld P, Hata N, DiMaio S, Zou K, Haker S, Fichtinger G, Tempany CMC. *Transperineal prostate biopsy under magnetic resonance image guidance: A needle placement accuracy study.* J Magn Reson Im. 2007; 26(3): 688-694.
[11] Wan G, Wei ZP, Gardi L, Downey DB, Fenster A. *Brachytherapy needle deflection evaluation and correction.* Med Phys. 2005; 32(4): 902-909.
[12] Stattaus J, Maderwald S, Baba HA, Gerken G, Barkhausen J, Forsting M, Ladd ME. *MR-guided liver biopsy within a short, wide-bore 1.5 Tesla MR system.* Eur Radiol. 2008; 18(12): 2865-2873.
[13] Crocetti L, Della Pina C, Cioni D, Lencioni R. *Peri-intraprocedural imaging: US, CT, and MRI.* Abdom Imaging. 2011; 36(6): 648-660.
[14] DiMaio SP, Salcudean SE. *Needle steering and motion planning in soft tissues.* IEEE T Bio-Med Eng. 2005; 52(6): 965-974.
[15] Glozman D, Shoham M. *Image-guided robotic flexible needle steering.* IEEE T Robotic Autom. 2007; 23(3): 459-467.
[16] Cowan NL, Goldberg K, Chirikjian GS, Fichtinger G, Alterovitz R, Reed KB, Kallem V, Park W, Misra S, Okamura AM. *Robotic needle steering: Design, modeling, planning, and image guidance.* In: Rosen J, Hannaford B, Satava R, eds. Surgical Robotics. Springer, 2011; 557-582.
[17] Webster R, Okamura AM, Cowan NJ. *Toward active cannulas: Miniature snake-like surgical robots.* International Conference on IEEE/RSJ. China, Beijing, 2006.
[18] Dupont PE, Lock J, Itkowitz B, Butler E. *Design and control of concentric-tube robots.* IEEE T Robot. 2010; 26(2): 209-225.
[19] Okazawa S, Ebrahimi R, Chuang J, Salcudean SE, Rohling R. *Hand-held steerable needle device.* IEEE/ASME T Mech. 2005; 10(3): 285-296.
[20] Webster RJ, Kim JS, Cowan NJ, Chirikjian GS, Okamura AM. *Nonholonomic modeling of needle steering.* Int J Robot Red. 2006; 25(5-6): 509-525.
[21] Majewicz A, Marra S, Van Vledder M, Lin M, Choti M, Song D, Okamura A. *Behavior of tip-steerable needles in ex vivo and in vivo tissue.* IEEE T Bio-Med Eng. 2011; 59(10): 2705-2715.
[22] Sitzman BT, Uncles DR. *The effects of needle type, gauge, and tip bend on spinal needle deflection.* Anesth Analg. 1996; 82(2): 297-301.
[23] Engh JA, Podnar G, Kondziolka D, Riviere CN. *Toward effective needle steering in brain tissue.* 28th IEEE/EMBS, USA, New York, 2006.
[24] Abolhassani N, Patel R, Ayazi F. *Effects of different insertion methods on reducing needle deflection.* 29th IEEE/EMBS, France, Lyon, 2007.
[25] Wood NA, Shahrour K, Ost MC, Riviere CN. *Needle steering system using duty-cycled rotation for percutaneous kidney access.* IEEE/EMBS, Argentina, Buenos Aires, 2010.

[26] Frasson L, Ferroni F, Ko S, Dogangil G, Rodriguez y Baena F. *Experimental evaluation of a novel steerable probe with a programmable bevel tip inspired by nature.* J Robotic Surg. 2012; 6(3): 189-197.

[27] Ko S, Rodriguez y Baena F. *Towards a miniaturized needle steering system with path planning for obstacle avoidance.* IEEE T Bio-Med Eng. 2013: 60(4); 910-917.

[28] Wendt M, Wacker FK. *Visualization, tracking, and navigation of instruments for magnetic resonance imaging-guided endovascular procedures.* Topi Magn Reson Imag. 2000; 11(3): 163-172.

[29] Robert A, Chagnon G, Bonvilain A, Cinquin P, Moreau-Gaudry A. *Toward a real-time tracking of a medical deformable needle from strain measurements.* 35th IEEE/EMBS, Japan, Osaka, 2013.

[30] Hill KO, Meltz G. *Fiber Bragg grating technology fundamentals and overview.* J Lightwave Technol. 1997; 15(8): 1263-1276.

[31] Rao YJ. *In-fibre Bragg grating sensors.* Meas Sci Technol. 1997; 8(4): 355-375.

[32] Rao YJ. *Recent progress in applications of in-fibre Bragg grating sensors.* Opt Laser Eng. 1999; 31(4): 297-324.

[33] Majumder M, Gangopadhyay TK, Chakraborty AK, Dasgupta K, Bhattacharya DK. *Fibre Bragg gratings in structural health monitoring - Present status and applications.* Sens Actuat A-Phys. 2008; 147(1): 150-164.

[34] Luyckx G, Voet E, Lammens N, Degrieck J. *Strain measurements of composite laminates with embedded fibre Bragg gratings: Criticism and opportunities for research.* Sensors. 2011; 11(1): 384-408.

[35] Mishra V, Singh N, Tiwari U, Kapur P. *Fiber grating sensors in medicine: Current and emerging applications.* Sens Actuat A-Phys. 2011; 167(2): 279-290.

[36] Kesner JE, Gavalis RM, Wong PY, Cao CGL, Kesner JE. *Multifiber optical bend sensor to aid colonoscope navigation.* Opt Eng. 2011; 50(12).

[37] Zhang L, Qian J, Shen L, Zhang Y. *FBG sensor devices for spatial shape detection of intelligent colonoscope.* IEEE ICRA. 2004; 1: 834-840.

[38] Zhang L, Qian J, Zhang Y, Shen L. *On SDM/WDM FBG sensor net for shape detection of endoscope.* IEEE ICMA. 2005; 4: 1986-1991.

[39] Ledermann C, Hergenhan J, Weede O, Woern H. *Combining shape sensor and haptic sensors for highly flexible single port system using Fiber Bragg sensor technology.* IEEE/ASME MESA. China, Suzhou, 2012.

[40] Park YL, Elayaperumal S, Daniel B, Ryu SC, Shin M, Savall J, Black RJ, Moslehi B, Cutkosky MR. *Real-time estimation of 3-D needle shape and deflection for MRI-guided interventions.* IEEE ASME Trans Mechatron. 2010; 15(6): 906–915.

[41] Park YL, Elayaperumal S, Daniel BL, Kaye E, Pauly KB, Black RJ, Cutkosky MR. *MRI-compatible Haptics: Feasibility of using optical fiber Bragg grating strain-sensors to detect deflection of needles in an MRI environment.* Int Soc Magn Res Med. 2008.

[42] Park YL, Elayaperumal S, Ryu S, Daniel B, Black RJ, Moslehi B, Cutkosky M. *MRI-compatible Haptics: Strain sensing for real-time estimation of three dimensional needle deflection in MRI environments.* Int Soc Magn Res Med. 2009.

[43] Misra S, Reed KB, Douglas AS, Ramesh K, Okamura AM. *Needle-tissue interaction forces for bevel-tip steerable needles.* 2nd IEEE RAS & EMBS, USA, Scottsdale, 2008.

[44] Ho SCM, Razavi M, Nazeri A, Song G. *FBG sensor for contact level monitoring and prediction of perforation in cardiac ablation*. Sensors. 2012; 12(1): 1002-1013.
[45] Iordachita I, Sun Z, Balicki M, Kang JU, Phee SJ, Handa J, Gehlbach P, Taylor R. *A sub-millimetric, 0.25 mN resolution fully integrated fiber-optic force-sensing tool for retinal microsurgery*. Int J Comput Assist Radiol Surg. 2009; 4(4): 383-390.
[46] Sun ZL, Balicki M, Kang J, Handa J, Taylor R, Iordachita I. *Development and preliminary data of novel integrated optical micro-force sensing tools for retinal microsurgery*. IEEE ICRA. 2009; 1: 4149-4154.
[47] Elayaperumal S, Bae JH, Christensen D, Cutkosky MR, Daniel BL, Black RJ, Costa JM, Faridian F, Moslehi B. *MR-compatible biopsy needle with enhanced tip force sensing*. World Haptics Conference. China, Daejeon, 2013.

2

Steerability of a fully actuated needle tip

Kirsten R. Henken, Luca G. Paroni, Jules S. Scheltes, Jenny Dankeman, John J. van den Dobbelsteen

ABSTRACT

BACKGROUND In percutaneous needle interventions, the success of the treatment is dependent on the accuracy with which the tip of the needle is positioned at the target. Currently, straight needles are used, which deflect unpredictably during insertion due to asymmetries in the needle and unknown properties of the surrounding tissue. The ability to actively steer the needle towards the target may improve endpoint accuracy and thereby optimize the clinical outcome. The aim of this research is to evaluate the steerability of a needle with an actuated tip.

METHOD The needle consists of an actively bendable tip with hinges and a passively compliant shaft. The deflection and orientation of the tip can be controlled by pulling cables that run through the needle and are attached at the tip. Experiments are executed to evaluate the relationship between steering angle and the resulting deflection of the needle. The steering angle of the tip is fixed and the needle is inserted in an ex vivo model multiple times, while the deflection of the needle tip is monitored with ultrasound.

RESULTS The degree of deflection depends on the steering angle that is applied at the tip. Deflections up to 17 mm occur at an insertion depth of 40 mm when a steering angle of 3° is applied to the steerable tip. The direction of the needle deflection is highly variable in these experiments.

CONCLUSION Needle steering using an actuated needle tip is feasible. To improve directional control the design of the needle needs to be adjusted. Future designs should be stiffer to withstand high stiffness forces in the tissue.

2.1 INTRODUCTION

Target accuracy is essential for the success of many needle interventions, such as tumor ablation in the liver. If the needle tip is not positioned correctly, healthy tissue is destroyed, while diseased tissue remains [1]. Besides this, patients can be excluded for the treatment when the target cannot be reached with a straight needle (e.g. certain regions in the liver are surrounded by the lungs and ribs). Positioning of the needle is complicated by unpredictable deflection of the needle caused by asymmetries of the needle and inhomogeneities of the tissue [2]. It commonly occurs in current clinical practice that the needle needs to be inserted multiple times to reach the target. This results in longer treatment times and more discomfort for the patient.

Proposed strategies to improve the accuracy of needle placement include path planning based on tissue models that predict needle deflection [2-5] and robotic systems for controlled needle steering [6-10]. An actively steerable needle may allow for higher target accuracy and enlarge the accessible area. Several designs of steerable needles have been proposed previously. Sears and Dupont [11] presented a steerable needle that consists of a number of curved concentric tubes that can be pushed out. Frasson et al. [12] designed a flexible multi-part probe with a programmable bevel tip. In the approach of Misra et al. [13], a needle with a bevel tip is rotated to control the degree and direction of bending during insertion. Rotation of these needles is required to reorient the steering direction.

This research aims to evaluate the feasibility of needle steering by means of an actuated tip. The controllability of the degree and direction of bending of the needle is quantified. The steerability of the prototype is tested in an ex vivo environment by fixing the steering angle and monitoring the corresponding deflection of the needle with ultrasound (US).

2.2 MATERIALS AND METHODS

2.2.1 Design of the steerable needle

The prototype consists of an actively steerable tip and a compliant shaft that passively follows (Figure 2.1). The steerable tip consists of nine stainless steel hinges produced by laser cutting and a conical stainless steel tip. The length of the complete tip is 24 mm. The hinges have a total length of 8.0 mm and the maximal steering angle is approximately 7°. The shaft is a PEEK tube with an inner and outer diameter of 1.5 mm and 2.0 mm, respectively. A ring of steering cables is positioned in the shaft and connected at the very end of the tip to provide actuation to the steering segment. This actuation system is according to the system described by Breedveld et al. [14].

The steering cables are stainless steel cables (0.32 mm, 1x12). A core cable (0.54 mm, 7x7) is added in the middle to fill up the tube and keep the steering cables in place. Deflection of the tip is achieved by pulling one or multiple steering cables (Figure 2.2). The orientation of the tip can be adjusted by pulling different cables.

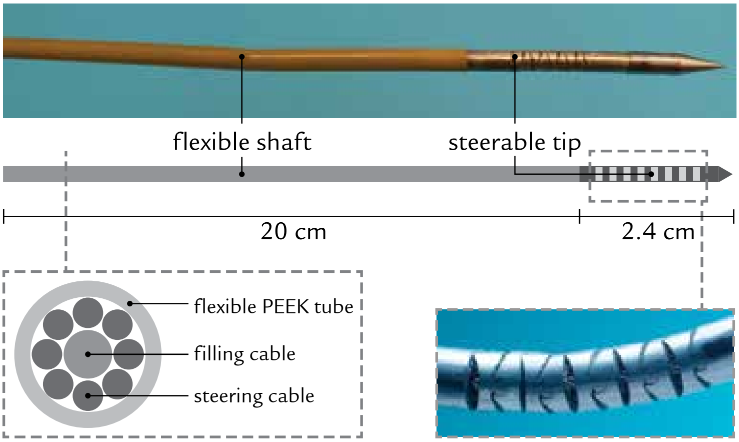

FIGURE 2.1 Schematic view of the needle. The needle consists of a passively compliant shaft and an actively steerable tip. Actuation of the steerable tip is provided by a ring of steering cables that run through the shaft and are attached to the tip.

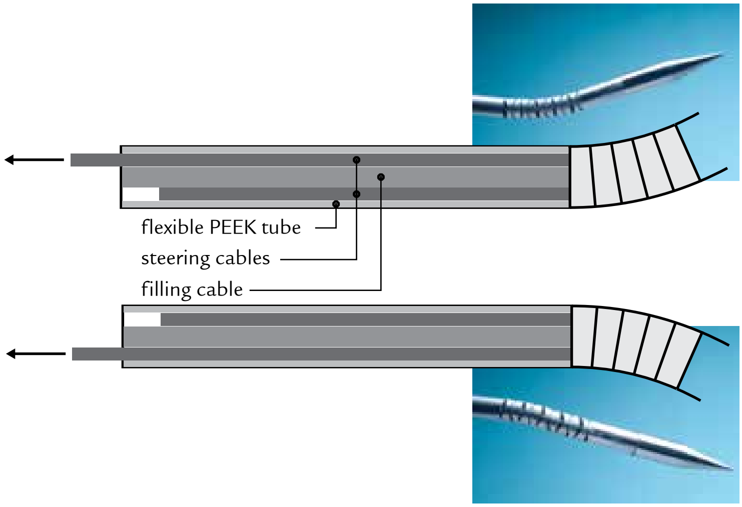

FIGURE 2.2 Working principle of the steerable needle. The tip bends when a cable is pulled. Each of the eight steering cables forces the tip to bend in a different direction.

2.2.2 Experimental set-up

The prototype was tested in an ex vivo environment according to the set-up shown in Figure 2.3. The needle was attached to a vertically positioned linear stage (PRO 115, Aerotech, USA) by means of a custom made steering unit. The linear stage was actuated with a motor (EC 40, Maxon Motor, Switserland) and the position of the stage was measured with an optical incremental encoder (2RMHF, Scancon, Denmark). The motor was controlled with a dSPACE board (DS1104, dSPACE, Germany) with a user-interface (ControlDesk 3.4, dSPACE, Germany). A rigid arm that holds the US transducer was attached to the stage, so that the field-of-view was continuously aligned with the needle tip during insertion.

The ex vivo model consisted of a porcine liver lobe embedded in gel (1% Agar-Agar, 0.9% NaCl solution in water). The model was prepared in a Plexiglas box (230x110x80 mm) of which one side can be removed to allow direct contact between the model and the US transducer. During the experiments, the box with the porcine liver was placed in a water tank that was positioned under the stage to optimize transmission. The US transducer was positioned in plane with the needle tip. Outside the tissue, the needle was guided by a rigid tube to avoid buckling of the needle. First the needle was inserted approximately 2 cm into the model. Then a fixed steering angle of 0°, 1°, 2° or 3° to the right was applied to the tip of the needle with the steering unit. After that, the needle was inserted into the

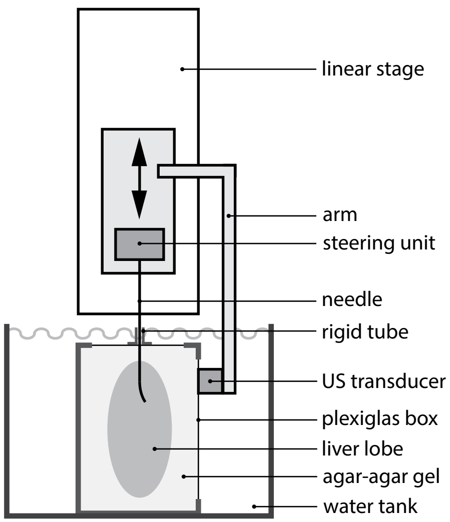

FIGURE 2.3 **Schematic view of the experimental set-up. The needle is connected to a steering unit that is mounted on a linear stage. A rigid arm that holds the ultrasound transducer is also connected to the linear stage. The needle passes a rigid tube before it enters the model to avoid buckling. The ex vivo model consists of a porcine liver lobe that is embedded in gel. The model is placed in a box that is put in a water tank during the experiments.**

FIGURE 2.4 An example of an ultrasound image on which the needle tip is visible (indicated by white circle). The images are provided at 25 frames per second with an accuracy of 0.375x0.333 mm.

model with a constant velocity of 5 mm/s aiming at a penetration depth of approximately 60 mm. The measurements were repeated six times per steering angle. During insertion the needle tip was tracked with a transducer (6C2 Ultrasound Transducer, Siemens) and a US imaging system (Acuson Sequoia 512, Siemens, Germany) at a rate of 25 frames per second with a calibrated accuracy of 0.375x0.333 mm. Figure 2.4 shows an example of an ultrasound image of the needle tip during insertion.

2.3 RESULTS

During insertion of the needle in the ex vivo model, the insertion depth and the deflection of the needle tip are monitored. We aimed at a constant insertion depth of 60 mm, but in most experiments the insertion needed to be aborted prematurely, because the tissue could not be penetrated further or because the needle tip moved out of the field of view of the US.

Figure 2.5 shows the insertion paths of the needle when the steering angle was set to 0° and to 3°. When the needle tip was straight, the path of the needle during insertion was almost straight. When a steering angle was applied, the needle deflects during insertion.

Figure 2.6 shows the total deflection of the needle at an insertion depth of 40 mm. The experiments in which the total insertion depth did not exceed 40 mm were disregarded. Data was linearly interpolated when no data was available at the exact insertion depth of 40 mm. When a steering angle of 0, 1°, 2°, and 3° is applied to the tip, the ranges of needle

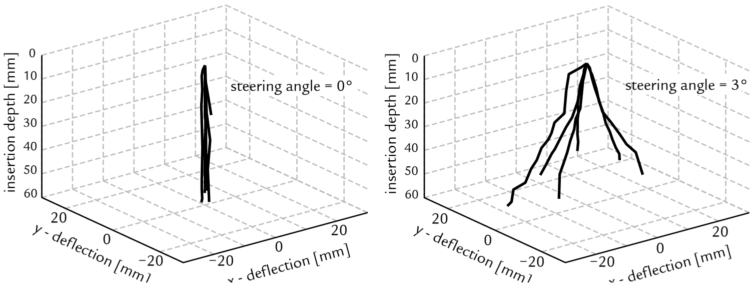

FIGURE 2.5 **Deflection of needle in x-direction and y-direction during insertion in z-direction for six repeated tests with a steering angle of 0° (left) or 3° (right). When the steering angle is set to 0°, the needle moves almost straight through the tissue. Deflection occurs when a steering angle is applied, but the direction of deflection does not correspond to the steering direction of the tip.**

deflection were 0.58-1.2 mm, 1.1-4.1 mm, 4.3-9.6 mm, and 10-17 mm, respectively, at an insertion depth of 40 mm. The deflection of the needle increases when the steering angle at the tip is increased. This indicates that steering of a needle with an actuated tip is feasible.

Figure 2.7 shows the deflections in x-direction and y-direction of the needle tip at an insertion depth of 40 mm for each experiment. Although the degree of steering of this prototype is related to the steering angle applied at the tip, the direction of deflection was unpredictable. The needle tip was expected to follow a path that was in the direction of the steering angle (only deflections in positive x-direction), but the actual direction differed in each measurement. This effect is especially present when a large steering angle was applied to the actuated tip.

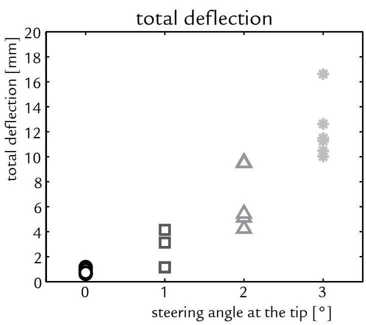

FIGURE 2.6 **Total deflection of the needle at an insertion depth of 40 mm. When the needle was not inserted over 40 mm, the measurement was disregarded. Deflection of the needle increases when the steering angle is increased.**

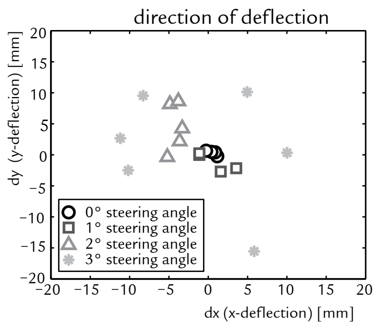

FIGURE 2.7 **Deflection of the needle in x-direction and y-direction at an insertion depth of 40 mm. Although the degree of deflection is related to the steering angle, the direction of bending was not controllable in this set-up.**

2.4 DISCUSSION

This research aimed at evaluating the feasibility of steering by means of an actuated needle tip. A prototype consisting of a steerable tip and a compliant shaft that passively follows the tip was produced and evaluated in an ex vivo set-up. Results showed that a needle with an actuated tip does allow for steering and that the degree of deflection of the needle is related to the steering angle applied at the tip. Only small tip angles were needed to initiate the deflection that is required for steering. However, the direction of movement could not be controlled well with this prototype and became particularly unpredictable when a large steering angle was applied to the tip. The properties of the tissue that the needle encounters during insertion may play a role in this. For example, when the needle tip runs into a stiff membrane or vessel and the tip is not sharp enough to puncture this structure, the needle will deviate from its original trajectory.

Properties of the needle itself also affect the direction of steering. The steering angle is set with the steering unit, but this is not translated one-to-one to the needle tip due to irregular tensioning of the cables. In addition, friction occurs between the cables and the cables can twist during the experiments. Besides this, the alignment of the hinges can be disturbed during the experiments due to wear. To solve these issues, the design of the needle has to be adjusted. Friction between and torsion of the steering cables needs to be eliminated. The stiffness of both the flexible shaft and the needle tip has to be increased to allow penetration of real tissue that can be stiff and strong. The cutting tip needs to be sharper to enable the passage through tough tissues. The improved steering mechanism allows for full control of the needle trajectory without introducing the need for rotation of the needle.

Apart from improvements to the design, the ability to control the path of the needle could be improved by real-time monitoring of needle deflection. One possibility to do so is the implementation of fibers with fiber Bragg gratings (FBGs) in the needle. FBGs measure strain and can be used to acquire information on the direction of the deflection [15]. When three fibers with multiple FBGs each are incorporated in the needle, strain at three positions in one cross-section are provided. The bending radius and the direction of bending at that position can be reconstructed by combining these three strain measurements. Based on this shape information, a clinician can adjust the tip orientation to follow the correct path to the target when the improved needle design allows for controllable steering.

Unlike the steerable needles that are proposed previously [11-13], a needle with a steerable tip that is equipped with FBGs for shape sensing that allows for controllable steering does not need a priori trajectory planning. The location of the needle tip and the path of the needle are monitored in real-time and can be adjusted at any moment during insertion. When the needle encounters unexpected structures, the path of the needle can be adjusted accordingly and withdrawing of the needle is not necessary.

2.5 CONCLUSION

The steerability of a needle with an actuated tip is evaluated. For this prototype only small steering angles are needed to enable significant deflection of the needle. The resulting degree of bending is related to the steering angle that is applied to the tip, but the direction of bending cannot be controlled well in this prototype. A redesign is needed to withstand internal (friction and torsion of the cables) and external (mechanical interaction with the punctured tissue) disturbances.

REFERENCES

[1] Khlebnikov R, Muehl J. *Effects of needle placement inaccuracies in hepatic radiofrequency tumor ablation*. 32nd Annual International Conference of the IEEE EMBC, Argentina, Buenos Aires, 2010.
[2] Misra S, Reed K, Schafer B, Ramesh K, Okamura A. *Mechanics of flexible needles robotically steered through soft tissue*. Int J Robot Res. 2010; 29(13): 1640–1660.
[3] Glozman D, Shoham M. *Flexible needle steering and optimal trajectory planning for percutaneous therapies*. In: Barillot C, Haynor DR, Hellier P, eds. Lect Notes Comput Sc. Berlin: Springer-Verlag Berlin, 2004. 137–144.
[4] Duindam V, Xu J, Alterovitz R, Sastry S, Goldberg K. *Three-dimensional motion planning algorithms for steerable needles using inverse kinematics*. Iny J Robot Res. 2010; 29(7): 789-800.
[5] Chui CK, Teoh SH, Ong CJ, Anderson JH, Sakuma I. *Integrative modeling of liver organ for simulation of flexible needle insertion*. 9th IEEE ICARCV, USA, New York, 2006.
[6] Glozman D, Shoham M. *Flexible needle steering for percutaneous therapies*. Comput Aided Surg. 2006; 11(4): 194–201.
[7] Hata N, Hashimoto R, Tokuda J. *Needle guiding robot for MR-guided microwave thermotherapy of liver tumor using motorized remote-center-of-motion constraint*. 8th IEEE ICARCV, USA, New York, 2005.
[8] Seifabadi R, Song SE, Krieger A, Cho N, Tokuda J, Fichtinger G, Iordachita I. *Robotic system for MRI-guided prostate biopsy: feasibility of teleoperated needle insertion and ex vivo phantom study*. Int J Comput Assist Radiol Surg. 2012; 7(2): 181-190.
[9] Krieger A, Susil RC, Menard C, Coleman JA, Fichtinger G, Atalar E, Whitcomb LL. *Design of a novel MRI compatible manipulator for image guided prostate interventions*. IEEE Trans Biomed Eng. 2005; 52(2): 306-313.
[10] Masamune K, Ohara F, Matsumiya F, Liao H, Hashizume M, Dohi T. *MRI compatible robot for needle placement therapy with accurate registration*. In: Springer, 2007, pp. 3056-3059.
[11] Sears P, Dupont P. *A steerable needle technology using curved concentric tubes*. IEEE/RSJ, China, Beijing, 2006.

[12] Frasson L, Ferroni F, Ko S, Dogangil G, Rodriguez y Baena F. *Experimental evaluation of a novel steerable probe with a programmable bevel tip inspired by nature.* J Robotic Surg. 2012; 6(3): 189-197.
[13] Misra S, Reed KB, Douglas AS, Ramesh K, Okamura AM. *Needle-tissue interaction forces for bevel-tip steerable needles.* 2nd IEEE RAS & EMBS, USA, Scottsdale, 2008.
[14] Breedveld P, Scheltes JS, Blom EM, Verheij JEI. *A new, easily miniaturized steerable endoscope.* IEEE Eng Med Biol Mag. 2005; 24(6): 40–47.
[15] Henken K, Van Gerwen D, Dankelman J, Van den dobbelsteen JJ. *Accuracy of needle position measurements using fiber Bragg gratings.* Minim Invasiv Ther, 2012; 21(6): 408-414.

3

Manually controlled steerable needle for MRI-guided percutaneous interventions

Kirsten R. Henken, Peter R. Seevinck, Luca G. Paroni, Jenny Dankelman, John J. van den Dobbelsteen

This chapter has been submitted for publication.

ABSTRACT

BACKGROUND To develop and evaluate a manually controlled steerable needle that is compatible with and visible on MRI to facilitate full intra-procedural control and accurate navigation in percutaneous interventions, such as high-dose-rate brachytherapy.

METHOD The steerable needle has a working channel that provides a lumen to a cutting stylet or a regular therapeutic instrument. A steering mechanism based on cable-operated, compliant elements is integrated in the working channel. The needle can be steered by adjusting the orientation of the needle tip through manipulation of the handle. The shaft of the needle is flexible and passively follows the trajectory of the needle tip. The relationship between the steering angle at the tip and the path curvature is investigated in a gel phantom by fixing the steering angle and tracking the resulting trajectory of the needle tip. The possibility to control the needle path under MRI-guidance is evaluated by manually steering the needle to different targets in a gel phantom that was placed in the bore of the scanner.

RESULTS The degree of deviation from a straight trajectory is related to the steering angle applied to the needle tip. Furthermore, the possibility to steer a needle to targets at different locations while starting from the same initial position and orientation under MRI-guidance is demonstrated. Sequences that are generally available for interventional procedures are able to visualize the needle and its tip.

CONCLUSION A manually controlled steerable needle compatible with and visible on MRI was developed to allow for intra-procedural trajectory optimization in percutaneous interventions. The design offers flexibility to the physician in control and choice of the needle path when navigating the needle towards the target position. This introduces the possibility to optimize the individual treatment and may increase target accuracy.

3.1 INTRODUCTION

Liver cancer is the fifth most commonly diagnosed cancer and the second most deadly form of cancer in men worldwide [1]. In addition to the preferred treatment options (surgical resection and transplantation [2]), multiple other therapies are suggested including high-dose-rate (HDR) brachytherapy. HDR brachytherapy as a therapy for liver cancer is still in an experimental phase [3, 4], but its effectiveness has been shown previously in prostate cancer [5, 6]. HDR brachytherapy is not influenced by the heat losses through blood flow like ablative techniques and is more flexible regarding the number of tumors and the tumor size, so this treatment could be beneficial for patients that are otherwise untreatable.

The success of HDR brachytherapy and other percutaneous needle interventions is highly dependent on accurate positioning of the needle tip. However, this can be complicated by unpredictable needle deflection and target movement due to tissue deformation and breathing [7]. Source placement in brachytherapy is most commonly guided by ultrasound or CT [3, 8], but nowadays interest in MRI is increasing because of its lack of ionizing radiation and its excellent soft tissue contrast [9, 10]. Additionally, MRI can provide structural, functional and physiological tissue parameters, which facilitates immediate visualization of the effect of the treatment [11, 12]. Currently, needles are navigated to the target position by means of an iterative process in which the needle is advanced and imaged subsequently in case of image-guidance through CT or fluoroscopy. In interventions guided by ultrasound, needle insertion and imaging are executed simultaneously. Irrespective of the imaging modality, the direction of insertion can hardly be adjusted once the needle has penetrated the tissue, which limits the control options to either advancing or retracting and reinserting the needle.

This research aims at the development of a manually controlled steerable needle that is compatible with and visible on MRI to provide active control of the needle trajectory during insertion for accurate tip positioning. Multiple steering strategies have been proposed previously, which include base manipulation [13, 14], telescopic mechanism [15, 16], and asymmetric (beveled and precurved) needle tips [17-19]. Most of these approaches involve simultaneous control of multiple degrees of freedom, computer controlled path planning and predictive models, which is not yet attainable for implementation in clinical practice. This work describes the design and the validation of a needle that can be manually actuated and controlled by the physician under image guidance and thereby offers flexibility in navigation to the target position. The performance of the instrument is further evaluated by an in vitro MRI-guided intervention.

3.2 MATERIALS AND METHODS

3.2.1 Steerable needle

The manually controlled steerable needle consists of three main parts (Figure 3.1): cutting stylet, working channel, and handle with slider to lock the steering mechanism. The distal part of the working channel can actively be oriented into the right direction with the handle, while the flexible needle shaft passively follows as the needle progresses through the tissue. The cutting stylet runs through the working channel and can be replaced by a diagnostic or therapeutic instrument when the target has been reached. The working principle of the manually controlled steerable needle is visualized in Figure 3.2. The extremities of four steering cables are attached to the middle part of the handle and to the tip of the working channel, respectively. The distal part of the needle can be locked in a straight position by pushing the slider forward. When the lock is released, the handle can be rotated with respect to the needle, so that at least one of the cables is pulled, which causes the needle to deflect at the distal end. Rotation of the handle is bounded through a mechanical stop in the handle which limits the bending angle at the distal end to 20° in all directions.

The cutting stylet with a diameter of 1.9 mm consists of three parts: a flexible polyether ether ketone (PEEK) tube; a highly flexible part made out of Teflon; and a titanium conical tip connected to each other by means of press fittings. The titanium tip generates a larger artefact than other parts, which enhances its visibility. The working channel is a PEEK tube with an outer and inner diameter of 3.2 and 2.0 mm, respectively. Four grooves are milled along the working channel to provide space for the Dyneema steering cables

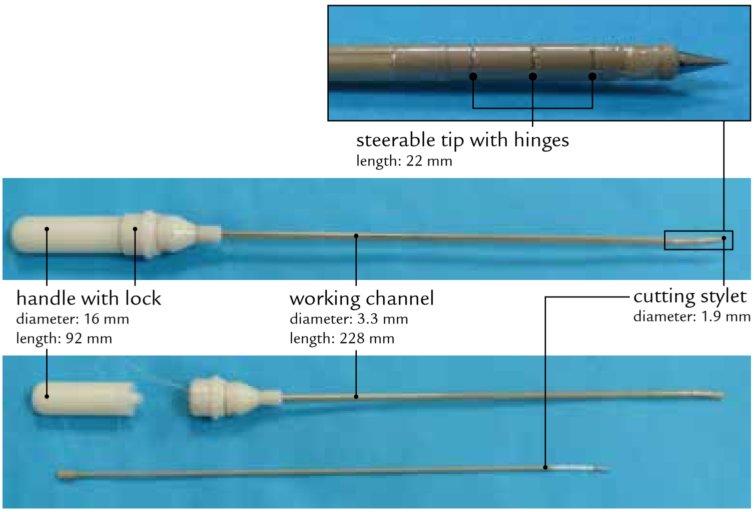

FIGURE 3.1 **The steerable needle: handle, steerable shaft, and cutting stylet; b) working principle.**

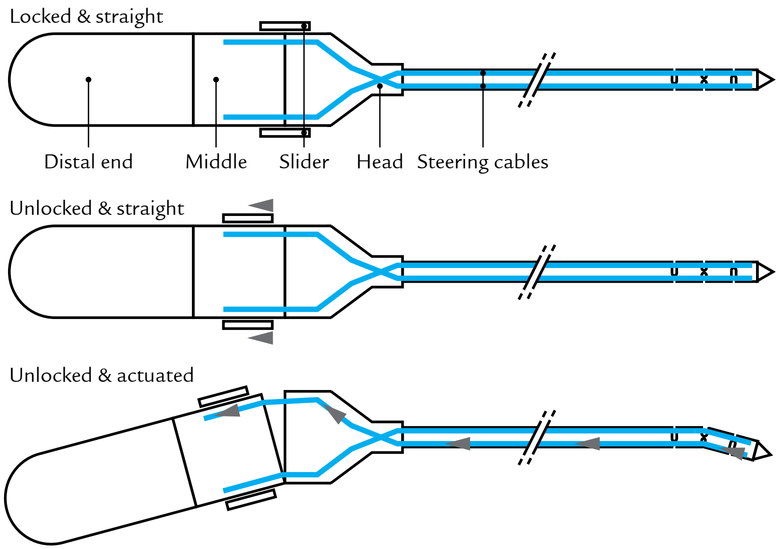

FIGURE 3.2 **Working principle of the steerable needle.**

(Nanofil, Berkeley, USA). In addition, three pairs of radial grooves are milled in the distal part of the working channel to create compliant elements in the steerable tip with a length of 22 mm. The three pairs are positioned with a spacing of 5.0 mm and oriented in 120° with respect to each other to allow for bending of the tip in all directions. The working channel is covered with a biocompatible polyethylene terephthalate (PET) shrinking tube (103-0302, Vention Medical – Advanced Polymers, USA). The polyoxymethylene (POM) and PEEK handle consists of four main parts (Figure 3.1): 1. the distal end that provides an easy pencil grip; 2. the middle part to which the cables are attached; 3. the head of the handle that contains a hinge and connects to the needle; 4. The slider with which the needle can be fixed in the straight position.

3.2.2 Validation of steering

The relationship between the steering angle of the tip and the resulting path curvature was evaluated in an in vitro set-up (Figure 3.3). The needle was attached to a linear stage (Aerotech PRO 115, Aerotech Inc., USA) and the steering angle at the distal end of the needle was fixed. Then the needle was moved down with a constant speed of 5 mm/s into a gel phantom (1% Agar-Agar and 0.9% NaCl in 2L water), until the needle had reached an insertion depth of approximately 60 mm. During insertion in y-direction, the needle was registered with an optical camera with a resolution of 0.12 mm. The resulting images were stored for analysis of the deflection of the needle afterwards. Three steering angles (4.7°, 12.6°, 20.3°) were applied to the needle tip in x-direction. After this, the gel phantom was replaced by a tissue phantom that consisted of a porcine liver embedded

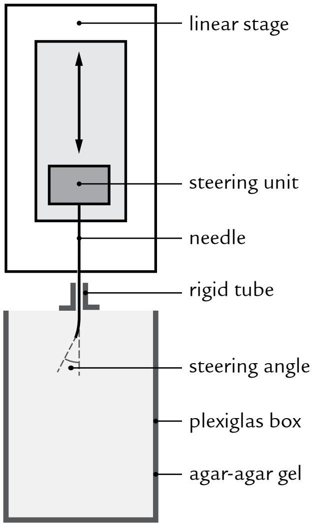

FIGURE 3.3 Schematic views of the experimental set-up to evaluate the steering mechanism using a linear stage.

in gel. The optical camera was replaced by a transducer (6C2 Ultrasound Transducer, Siemens) and an ultrasound imaging system (Acuson Sequoia 512, Siemens, Germany) that registered the needle tip at a rate of 25 frames per second with a calibrated accuracy of 0.375x0.333 mm. Each experiment was repeated six times per steering angle.

3.2.3 MRI-guided intervention

The aim of the in vitro MRI-guided intervention was to show how the needle trajectory can be controlled using real-time feedback obtained by MRI. The needle was inserted in a gel phantom (15% gelatin in 5L water in a 15x17x21 cm transparent box) to reach targets at different locations while starting from the same entry point and initial orientation. The targets were positioned at a depth of 120 mm. The first target was positioned 31 mm to the right and 2 mm below the point of insertion. The second target was positioned 4 mm to the left and 24 mm above the point of insertion. The phantom was positioned in the middle of the bore of the 1.5 T whole body MRI scanner (Philips Healthcare, The Netherlands) and the open side of the box was aligned with the opening of the bore. A coil setup consisting of two elliptical elements of 14×17 cm was applied for signal reception. One of the researchers was positioned next to the scanner and inserted the needle in the phantom to subsequently reach two targets starting at the same point of insertion. Figure 3.4 provides an overview of the set-up of this experiment.

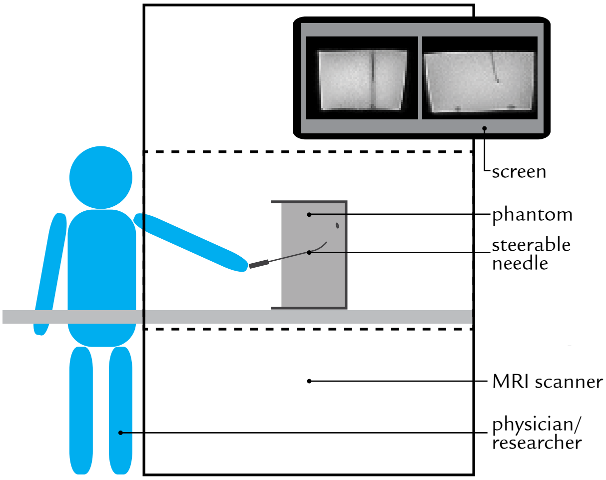

FIGURE 3.4 Schematic views of the experimental set-up to evaluate of the integration of the steerable needle in an MRI-guided treatment.

A volume scan was made for planning. Based on the volume scan, angulated coronal and sagittal planes were selected in such a way that both the needle tip and the target were enclosed in the interception of the planes. These planes visualized the deflections of the needle to the left and to the right and deflections upward and downward. The fast dual-plane dynamic scans of these planes were shown on a display in the MRI-room to provide insight in the required steering motion to the researcher during the procedure. The scan parameters of the volume scan and the intra-procedural dual-plane dynamic scans are provided in Table 3.1. Advancement of the needle was executed iteratively by subsequently updating the dual-plane dynamic scans, deciding on the manipulation required to reach the target (left-right and up-down), and applying the manipulation while advancing the needle approximately 1-2 cm. Both the volume and the dual-plane scans obtained during the procedure were stored for post-procedural analysis to verify if the targets had been reached.

The 3-D volume scans were post-processed according to a reconstruction method known as center-out radial sampling with off-resonance (coRASOR) reconstruction. This reconstruction aims at selective depiction of the needle with high positive contrast. CoRASOR reconstructions were performed in Matlab (The MathWorks, USA) using an off-resonance value of 5000 Hz. A detailed description of both the principles and the workflow of the coRASOR reconstruction method can be found elsewhere [20-22]. Background suppression was obtained by subtracting the on-resonance image from the coRASOR reconstructed image [20].

TABLE 3.1 **MRI scan parameters.**

	Volume scan	Dual-plane dynamic scan
Type	3-D, ultra-short echo time, free induction decay sampling with a center-out radial read-out	2-D, free induction decay sampling with a center-out radial read-out [22]
Field of view	192x192x192 mm^3	192x192 mm^2
Slice thickness	-	10 mm
Acquired/reconstructed isotropic voxel size	1.5/1.0 mm	1.5/1.0 mm
Echo time (TE)	0.34 ms	0.75 ms
Repition time (TR)	3.27 ms	3.34 ms
Flip angle	15°	25°
Read-out bandwidth	1332 Hz/pixel	1332 Hz/pixel
Scan duration	1min 48s	2.1 s/dynamic scan

3.3 RESULTS

3.3.1 Validation of steering

Figure 3.5 shows the trajectories that the tip of the needle followed during insertion in the gel as monitored by the optical camera. Deflection is defined as the perpendicular distance between the actual needle trajectory and a straight vertical trajectory. As expected, a larger steering angle results in more deflection, although variation is present. After the needle was advanced over 60 mm in the gel phantom, the deflections ranged from 2.2-3.8 mm, 6.3-9.6 mm, and 9.1-13.3 mm for a steering angle of 4.7°, 12.6°, and 20.3°, respectively. The deflections of the needle at an insertion depth of 60 mm in the liver phantom ranged from 1.3-5.1 mm, 0.8-15.7 mm, and 4.6-18.9 mm for a steering angle of 4.7°, 12.6°, and 20.3°, respectively.

3.3.2 MRI-guided intervention

First the needle was inserted and a volume scan was made to determine the location of the needle tip and the target. Based on this scan, the two imaging planes to be displayed intra-procedurally were selected. An example of the dual-plane dynamic scans is shown in Figure 3.6c. These images demonstrate that the needle can clearly be visualized, without inducing large image distortions of signal voids. The first plane was an oblique plane between the coronal plane and the transversal plane. This plane provided information about steering actions in the left-right direction. In this plane, the tip visualization is enhanced through its artefact. The second plane was orthogonal to the first plane and

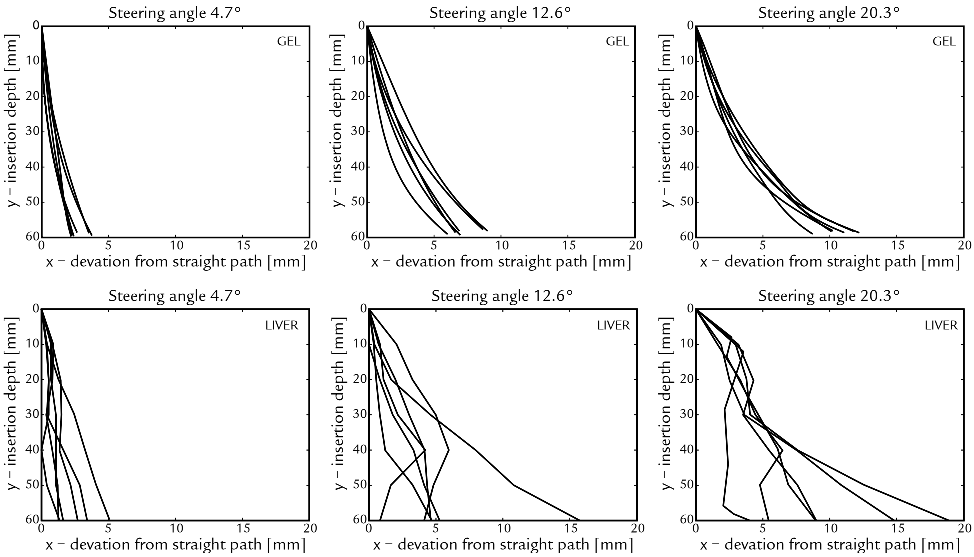

FIGURE 3.5 The trajectories that the needle tip followed during insertion in the gel or liver phantom. Generally, a larger steering angle results in more deflection of the needle than a smaller angle.

provided information about upward and downward steering. Both planes included the entry point and the target. The hypointense band that is visible in the second plane indicates the cross section of the first imaging plane and is caused by saturation effects present due to the short acquisition times of the dual-plane imaging sequence.

Figure 3.6 provides a selection of dynamic images of the second plane obtained in between the iterative insertion steps to reach the two targets. The first three images (Figure 3.6a-c) show three out of the seven steps in which the needle is approaching the first target. After the first target has been reached, the needle is retracted and new planes are selected that include the second target. Figure 3.6d-i show six out of eleven steps that were required to target the second target. The first attempt to target the second target (Figure 3.6d-f) was not successful, because steering was only initiated when the needle tip was already close to the target. Therefore, the needle was withdrawn and the target was reached in a second attempt (Figure 3.6g-i).

After the intervention, the MRI scans were subjected to post-processing. CoRASOR-recontructed 3-D volume scans enabled positive contrast visualization of the needle trajectories in 3-D, as shown in Figure 3.7. The targets are depicted with relatively high intensity as compared to the gel medium on the maximum intensity projections, but the needle is presented hyperintense. The orthogonal maximum intensity projections confirm that both targets are successfully reached from a single entry point while solely supported by 2-D MRI guidance.

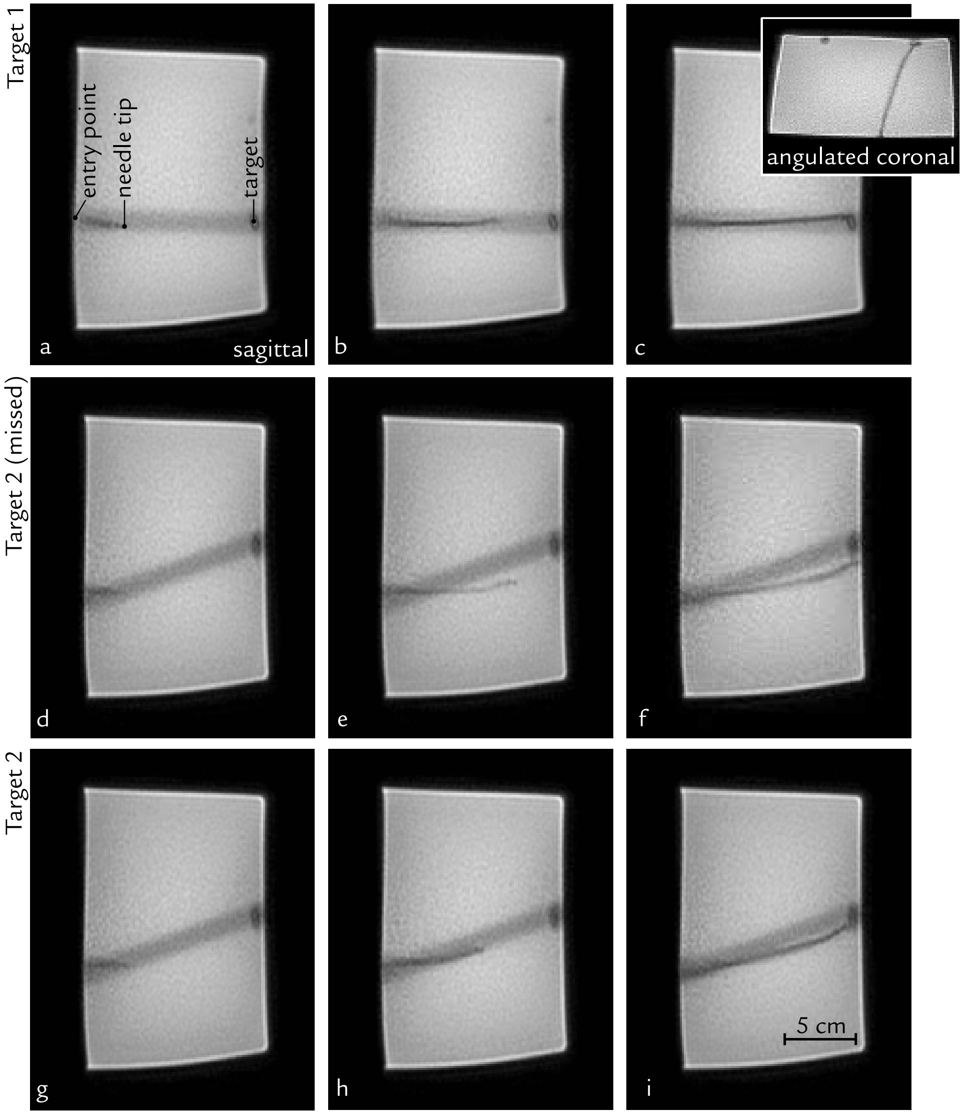

FIGURE 3.6 A selection of the two-plane images provided to the researcher during needle insertion: a-c) show the iterative process in which the first target is targeted; d-f) show the first attempt to target the second target; and g-i) show the final and successful attempt to target the second target.

3.4 DISCUSSION

This work aimed at the development and evaluation of a manually controlled steerable needle to provide active control in MRI-guided interventions that require accurate targeting, such as HDR brachytherapy. The orientation of the tip of the proposed needle could be adjusted by manipulating the handle thereby steering the needle in the

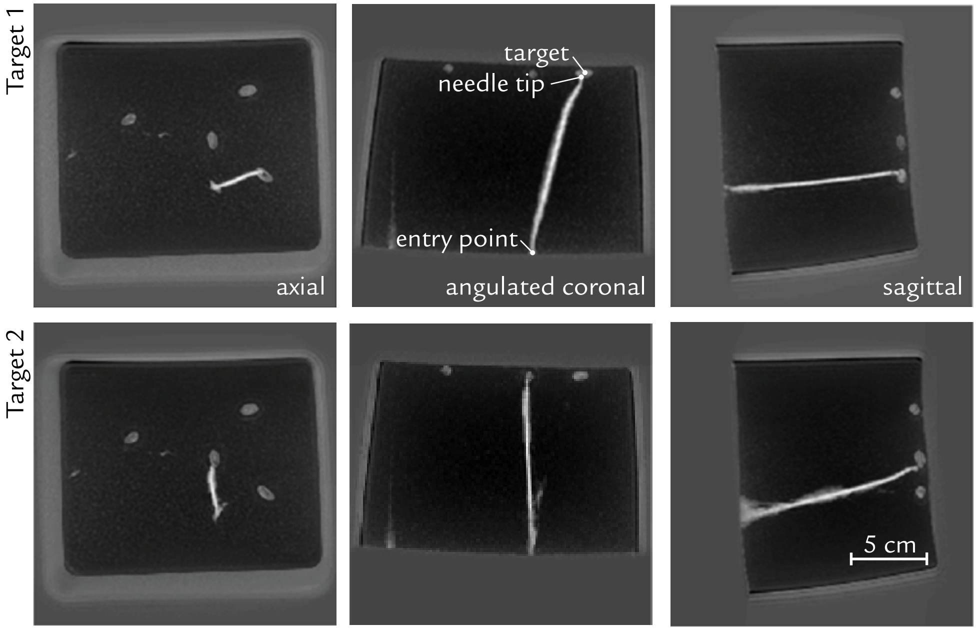

FIGURE 3.7 **Orthogonal scans of the final needle trajectory obtained through post-processing by means of the coRASOR reconstruction.**

required direction. The shaft of the needle passively followed. The needle was designed to be compatible with MRI and mainly consists of plastics. The titanium tip was the only exception and generated an artefact that improved its visibility on MRI.

In vitro experiments in gel showed that the steering angle applied to the tip of the needle determined the degree of deviation from a straight trajectory during insertion, which indicated that the needle trajectory could be adjusted by manipulating the tip orientation. Variations in deflection resulting from the same steering angle at the tip may have been due to variable friction and other mechanical losses in the needle. This did not necessarily affect the target accuracy since the trajectory could be adjusted at any time during insertion.

A second set of in vitro experiments was performed to further evaluate the needle in an MRI-guided procedure. In these experiments, the needle was successfully navigated to two targets at different locations starting from the same entry point with the same orientation, illustrating several important findings: 1) the developed needle can be visualized using a generally available dynamic MR imaging technique using a clinically relevant and realistic slice thickness of 10 mm; 2) the needle does not induce large image distortions or signal voids, enabling the simultaneous depiction of both the needle and surrounding soft tissue; 3) the steering abilities of the needle facilitates accurate navigation, enabling MR-guided targeting of predefined locations; 4) the paramagnetic properties of the titanium tip facilitate selective positive contrast visualization when increased specificity is necessary.

A steerable needle offers active control to the physician, so that the trajectory of the needle can be adjusted intra-procedurally. This reduces the need for retraction and reinsertion when the planned trajectory is not resulting in the correct position of the needle tip due to unforeseen needle deflection or tissue deformation. The steerability of the needle also introduces the possibility to reach multiple targets from a single point of insertion, which could be of added value when therapy needs to be applied to multiple locations (e.g. in case of multiple tumors). In addition, curved paths can be obtained so that penetration of critical and vulnerable structures (e.g. blood vessels or the lungs) can be avoided. The proposed needle could therefore facilitate individual treatment optimization and contribute to the accuracy of needle placement in image-guided interventions such as HDR brachytherapy in the liver.

The steering mechanism presented in this work has a number of advantages with respect to previously described steerable needles. In needle steering by means of base manipulation [13, 14], moments are applied around the point of insertion to reorient the needle tip. This can result in large forces around the entry point and along the needle. In the current mechanism, the forces that are required for steering are only initiated at the needle tip. When needle steering is obtained through a telescopic mechanism in which multiple concentric pre-curved tubes protrude through each other [15, 16], extensive pre-operative planning is required to translate the planned trajectory into control inputs that are needed to realize this trajectory. Operation of the current needle is more simple: the orientation of the needle tip can be adjusted at any time during insertion by reorienting the handle in the preferred direction. Operation of other needles that rely on the steering effects of asymmetries at the tip [17-19] is similar, but additional rotation around the longitudinal axis is required to adjust the direction of steering and to control the degree of steering.

Although the needle provides control of the trajectory, some demerits need to be taken into account. The experiment in the MRI showed that steering becomes more difficult when the needle is inserted deeper. This suggests that timely steering is preferred over last-minute adjustments. In addition, the freedom of movement of the physician is limited by the confined space in the bore of the scanner, which may affect the control options. Finally, applicability may be limited when it is expected that avoiding critical structures will most likely lead to inaccurate targeting.

The current study evaluated the steering capabilities of the needle in a gel phantom and in a tissue phantom. Neither of the phantoms contained critical structures that need to be avoided. This simplifies navigation thoroughly compared to an in vivo situation. The controllability of the needle is affected by the heterogeneity of tissue. The large heterogeneity of real tissue causes needles to deflect more, which stresses the need for active control of the needle trajectory. Besides this, the needle was controlled by one of the researchers, while one can expect more dexterity from an experienced physician, who could simultaneously insert the needle, control the tip direction, and verify the resulting trajectory on the continuously updated MR images. Extensive testing is required to gain insight in these factors. In such experiments, target accuracy, the number of attempts, and duration of the intervention should be measured to quantify the added value of this technology.

An important challenge for implementation in practice will be the selection of the imaging planes or volumes. In some cases, the imaging strategy as described here may be sufficient. In other cases, more sophisticated selection of imaging planes may be necessary, for example when the trajectory is expected or planned to be curved. Automatic selection of imaging plane could be guided by real-time tracking of the needle. This can be accomplished through shape sensing by means of fiber Bragg gratings that are integrated in the instrument, which is work in progress [23, 24]. The imaging planes of the MRI can in this case be matched real-time with the position and orientation of the needle and its tip as measured with the fiber Bragg gratings. However, from a safety perspective, visualization of the tip on MRI with respect to the target area will remain indispensable to assure that the tip is at the intended location when the treatment is started. Therefore, further research should also focus on optimization and validation of needle tip visualization using MRI.

3.5 CONCLUSION

A manually controlled steerable needle has been developed successfully. This needle provides active control of the needle trajectory and may increase the accuracy of needle positioning. Steering is initiated by adjusting the orientation of the needle tip. The needle was demonstrated to be compatible with MRI. The image quality in the direct vicinity of the needle was not affected, while the needle and its tip could be visualized clearly.

REFERENCES

[1] Jemal A, Bray F, Center MM, Ferlay J, Ward E, Forman D. *Global cancer statistics*. CA-Cancer J Clin. 2011; 61(2): 69-90.

[2] Forner, A., J.M. Llovet, and J. *Bruix, Hepatocellular carcinoma*. Lancet, 2012. 379(9822): p. 1245-1255.

[3] Mohnike K, Wieners G, Schwartz F, Seidensticker M, Pech M, Ruehl R, Wust P, Lopez-Hänninen E, Gademann G, Peters N. *Computed tomography-guided high-dose-rate brachytherapy in hepatocellular carcinoma: Safety, efficacy, and effect on survival.* Int J Radiat Oncol. 2010; 78(1): 172-179.

[4] Ricke J, Wust P. *Computed tomography-guided brachytherapy for liver cancer.* Semin Radiat Oncol. 2011; 21(4): 287-293.

[5] Yoshioka Y, Nose T, Yoshida K, Inoue T, Yamazaki H, Tanaka E, Shiomi H, Imai A, Nakamura S, Shimamoto S. *High-dose-rate interstitial brachytherapy as a monotherapy for localized prostate cancer: Treatment description and preliminary results of a phase I/II clinical trial.* Int J Radiat Oncol. 2000; 48(3): 675-681.

[6] Martinez AA, Pataki I, Edmundson G, Sebastian E, Brabbins D, Gustafson G. *Phase II prospective study of the use of conformal high-dose-rate brachytherapy as monotherapy for the treatment of favorable stage prostate cancer: A feasibility report.* Int J Radiat Oncol. 2001; 49(1): 61-69.

[7] Abolhassani N, Patel R, Moallem M. *Needle insertion into soft tissue: A survey.* Med Eng Phys. 2007; 29(4): 413-431.

[8] Ricke J, Wust P, Stohlmann A, Beck A, Cho CH, Pech M, Wieners G, Spors B, Werk M, Rosner C, Hanninen EL, Felix R. *CT-guided interstitial brachytherapy of liver malignancies alone or in combination with thermal ablation: Phase I-II results of a novel technique.* Int J Radiat Oncol. 2004; 58(5): 1496-1505.

[9] Ricke J, Thormann M, Ludewig M, Jungnickel K, Grosser O, Wybranski C, Peters N, Hass P, Bunke J, Fischbach F. *MR-guided liver tumor ablation employing open high-field 1.0 T MRI for image-guided brachytherapy.* Eur Radiol. 2010; 20(8): 1985-1993.

[10] Rothgang E, Gilson WD, Wacker F, Hornegger J, Lorenz CH, Weiss CR. *Rapid freehand MR-guided percutaneous needle interventions: An image-based approach to improve workflow and feasibility.* J Magn Reson Im. 2013; 37(5): 1202-1212.

[11] Rieke V, Pauly KB. *MR thermometry.* J Magn Reson Im. 2008; 27(2): 376-390.

[12] Lin ZY, Chen J, Deng XF. *Treatment of hepatocellular carcinoma adjacent to large blood vessels using 1.5 T MRI-guided percutaneous radiofrequency ablation combined with iodine-125 radioactive seed implantation.* Eur J Radiol. 2012; 81(11): 3079-3083.

[13] DiMaio SP, Salcudean SE. *Needle steering and motion planning in soft tissues.* IEEE T Bio-Med Eng. 2005; 52(6): 965-974.

[14] Glozman D, Shoham M. *Image-guided robotic flexible needle steering.* IEEE T Robotic Autom. 2007; 23(3): 459-467.

[15] Webster R, Okamura AM, Cowan NJ. *Toward active cannulas: Miniature snake-like surgical robots.* International Conference on IEEE/RSJ. China, Beijing, 2006.Dupont PE, Lock J, Itkowitz B, Butler E. Design and control of concentric-tube robots. IEEE T Robot. 2010; 26(2): 209-225.

[16] Webster RJ, Kim JS, Cowan NJ, Chirikjian GS, Okamura AM. *Nonholonomic modeling of needle steering.* Int J Robot Red. 2006; 25(5-6): 509-525.

[17] Majewicz A, Marra S, Van Vledder M, Lin M, Choti M, Song D, Okamura A. *Behavior of tip-steerable needles in ex vivo and in vivo tissue.* IEEE T Bio-Med Eng. 2011; 59(10): 2705-2715.

[18] Engh JA, Podnar G, Kondziolka D, Riviere CN. *Toward effective needle steering in brain tissue.* 28th IEEE/EMBS, USA, New York, 2006.

[19] Seevinck PR, De Leeuw H, Bos C, Bakker CJG. *Highly localized positive contrast of small paramagnetic objects using 3-D center-out radial sampling with off-resonance reception.* Magnet Reson Med. 2011; 65(1): 146-156.

[20] De Leeuw H, Seevinck PR, Bakker CJG. *Center-out radial sampling with off-resonant reconstruction for efficient and accurate localization of punctate and elongated paramagnetic structures.* Magnet Reson Med. 2013; 69(6): 1611-1622.

[21] De Leeuw H, Moerland MA, Van Vulpen M, Seevinck PR, Bakker CJG. *A dual-plane co-RASOR technique for accurate and rapid tracking and position verification of an Ir-192 source for single fraction HDR brachytherapy*. Phys Med Biol. 2013; 58(21): 7829.

[22] Henken K, Van Gerwen D, Dankelman J, Van den dobbelsteen JJ. *Accuracy of needle position measurements using fiber Bragg gratings*. Minim Invasiv Ther, 2012; 21(6): 408-414.

[23] Henken KR, Dankelman J, Van den Dobbelsteen JJ, Cheng LK, Van der Heiden MS. *Error analysis of FBG-based shape sensors for medical needle tracking*. ASME/IEEE T Mech. Published online 2013 Nov 11; doi: 10.1109/TMECH.2013.2287764.

4

Accuracy of needle position measurements using fiber Bragg gratings

Kirsten R. Henken, Dennis J. van Gerwen, Jenny Dankelman, John J. van den Dobbelsteen

This chapter is an adaptation of [1], reprinted with permission.

ABSTRACT

BACKGROUND Accurate placement of the needle tip is essential in percutaneous therapies such as radiofrequency ablation (RFA) of liver tumors. Use of a robotic system for navigating the needle could improve the targeting accuracy. Real-time information on the needle tip position is needed, since a needle deflects during insertion in tissue. Needle shape can be reconstructed based on strain measurements within the needle. In the current experiment we determined the accuracy with which the needle tip position can be derived from strain measurements using Fiber Bragg Gratings (FBGs).

METHOD Three glass fibers equipped with two FBGs each were incorporated in a needle. The needle was clamped at one end and deformed by applying static radial displacements at one or two locations. The FBG output was used for offline estimation of the needle shape and tip position.

RESULTS During deflections of the needle tip up to 12.5 mm, the tip position was estimated with a mean accuracy of 0.89 mm (std 0.42 mm). Adding a second deflection resulted in an error of 1.32 mm (std 0.48 mm).

CONCLUSION This accuracy is appropriate for applications like RFA of liver tumors. The results further show that the accuracy can be improved by optimizing the placement of FBGs.

4.1 INTRODUCTION

Liver cancer is highly fatal and resection of the liver is the only established treatment that may cure patients. Unfortunately, a lot of patients are ineligible for this treatment, because of the presence of multifocal tumors or insufficient liver function [2]. Therefore, multiple alternative treatments are studied, including percutaneous radiofrequency ablation (RFA) [3, 4]. RFA is mainly suitable for small tumors sized up to 3 cm in diameter, because of its limited effective range [4]. Recurrence rates up to 41% are reported after RFA of liver tumors, which is related to incomplete tumor ablation [5]. Accurate positioning of the tip of the RFA-needle is essential to ensure maximal effect of the treatment [6], but this is complicated by bending of the needle during insertion. Bending of the needle is caused by asymmetry of the needle and inhomogeneities of the tissue. The needle can deflect up to a third of the insertion depth [7]. In current clinical practice, the needle is inserted manually under guidance of radiography. During the insertion, the physician applies slight oscillation and rotation of the needle to avoid deflection. Deflection of the needle from the target leads to correction of the subcutaneous insertion pass or reinsertion.

Use of a robotic system for inserting and directing the needle could improve the targeting accuracy. Such a system could use natural bending by rotating the needle in such way that the needle bends towards the target area [7]. Alternatively, the robotic system could actively bend the needle when active steering elements are added to the needle [8]. Several robotic systems have been proposed for accurate navigation of the needle [9-16]. In one of these systems [14-16], MR images are used to compensate for prostate deformation during needle insertion. MRI has multiple advantages regarding visualization of tissue and treatment [17], but automatically retrieving the needle tip position from MR images for robotic control is still time-consuming [18-20].

A promising method to obtain real-time information on needle position for robotic control is fiber Bragg grating (FBG) technology. FBGs are optical strain sensors that can be incorporated in a needle and their read-out can be performed at high sampling rates (>20 kHz). This study aims to determine the accuracy with which the needle tip position can be estimated based on FBG measurements. We equipped a needle with a number of FBGs and recorded their output in an experimental setup in which radial displacements are applied. The accuracy with which the position of the tip of the needle could be reconstructed is determined.

4.2 MATERIALS AND METHODS

4.2.1 Needle and equipment

In the inner stylet of a trocar needle (18G/20cm, Cook Medical, Bloomington, IN), three grooves with a diameter of 300 μm were milled over the length at an angle of 120° with respect to each other. The depth of the grooves is assumed to be constant, so that the distance from the heart of the fibers to the heart of the needle d is constant as well. A glass fiber equipped with two FBGs (HI 780 (acrylate recoating), Corning Incorporated, Corning, NY) was glued in each of the grooves with an epoxy that is approved for medical applications (Loctite M-21HP, Henkel Nederland, The Netherlands). A schematic view of the needle is shown in Figure 4.1. Due to insufficient accuracy during assembly, the fibers were shifted relative to each other in longitudinal direction, so that the positions of the FBGs at a single location varied up to 17 mm. Figure 4.1 displays the averaged position of the three FBGs for each location.

4.2.2 Experimental set-up

An overview of the experimental set-up is shown in Figure 4.2. The handle of the needle was fixed and one or two displacements along the needle were applied to the needle with a knob attached to a translational platform (PT1/M, Thorlabs, Newton, NJ). The movement of the needle was restricted to the horizontal plane. The fibers were connected to an interrogator (Deminsys, Technobis, the Netherlands) that measured reflected wavelength with a sample frequency of 20 kHz. The measured wavelengths were registered and saved on a laptop computer for further processing.

4.2.3 Experimental procedure

In the first experiment, a static displacement of -12.5, -8.3, -4.2, 4.2, 8.3 or 12.5 mm was applied to the tip of the needle (Δy_t) in randomized order and the reflected wavelengths λ were measured with the interrogator. In the second experiment, two

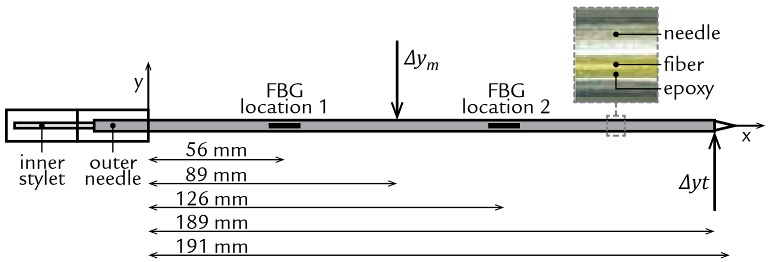

FIGURE 4.1 Schematic view of the needle.

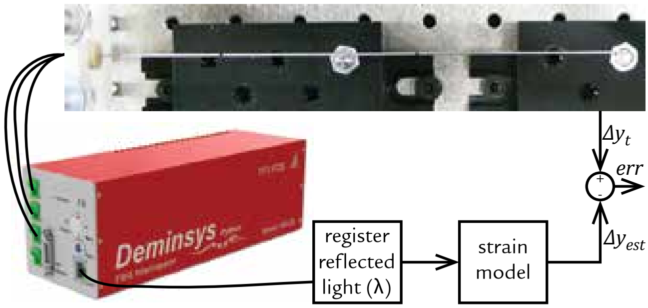

FIGURE 4.2 **Overview of experimental set-up. The handle of the needle (on the left) is fixed and one or two displacement knobs are placed tangent to the needle. The knobs are fixed on two (black) translational stages. The fibers are connected to an interrogator which measures wavelengths λ. These wavelengths are registered and used as input for the strain model, which computed the estimated tip position $\Delta\lambda_{est}$. This position is compared to the displacement applied at the tip $\Delta\lambda_t$.**

static displacements were applied to the needle: one at the tip (Δy_t) and one in the middle at 100 mm from the tip (Δy_m). The displacements were 12 and 3.3, 6.7 and 1.1, 1.1 and -1.1, -1.1 and 1.1, -6.7 and -1.1, and -12 and -3.3 mm at the tip and in the middle, respectively. The applied displacements resulted only in elastic deformation of the needle. In between the measurements, the displacement was removed and the reference wavelength $\lambda_{B,i}$ was measured. Both experiments were repeated five times.

4.2.4 Strain model

The period of the grating Λ in an FBG determines the Bragg wavelength λ_B that is reflected,

$$\lambda_B = 2n_{eff}\Lambda \quad (4.1)$$

where n_eff is the effective refractive index. By bending the needle the fibers are strained. We assume that the strain transfers completely from the needle to the fibers. The strain in the FBGs ε is proportional to the wavelength shift $\Delta\lambda_B$,

$$(\Delta\lambda_B)/\lambda_B = (1 - P_\varepsilon)\,\varepsilon \quad (4.2)$$

where P_ε is the photoelastic coefficient of the FBG. In this experiment, the wavelength shift is calculated by

$$\Delta\lambda_B = \lambda - \lambda_B \quad (4.3)$$

where λ and λ_B are the wavelengths measured during bending and in the preceding reference situation, respectively. Combining Equation (1) and (2) shows that strain is linearly related to $\Delta\lambda_B$ by a constant C, which includes all FBG-specific characteristics.

$$\Delta\lambda_B = 2n_{eff}\,\Lambda\,(1 - P_\varepsilon)\,\varepsilon = C\,\varepsilon \tag{4.4}$$

When the characteristics of each FBG are known, strain in that sensor can be calculated based on the measured wavelengths. The maximal strain ε_{max} at each FBG location in the needle is defined by

$$\varepsilon_A = \varepsilon_{max}\ \cos(-\alpha) + \varepsilon_0 \tag{4.5}$$

$$\varepsilon_B = \varepsilon_{max}\ \cos(120 - \alpha) + \varepsilon_0 \tag{4.6}$$

$$\varepsilon_C = \varepsilon_{max}\ \cos(240 - \alpha) + \varepsilon_0 \tag{4.7}$$

in which ε_A, ε_B, and ε_C are the calculated strains in Fiber A, B, and C at one location, respectively. ε_0 is the axial strain of the needle and α is the direction of ε_{max} with respect to Fiber A (Figure 4.3). In pure bending, no axial strain is present ($\varepsilon_0 = 0$). Therefore, the set of equations is over defined (three equations, two unknowns) and ε_{max} and α are calculated three times and averaged.

In the first experiment, strain was linearly regressed over the length of the needle based on ε_{max} measured at two locations and on the strain at the tip which must be zero. In the second experiment, the location of the applied displacement in the middle Δy_m was assumed to be known. First, the strain between that location and the tip was linearly regressed based on ε_{max} at the second FBG location and $\varepsilon = 0$ at the tip. Secondly, the strain between the base of the needle and the location of Δy_m was linearly regressed based on ε_{max} at the first FBG location and the strain at the location of Δy_m derived from the previous regression. In each experiment, ε_{max} at 100 locations along the needle was calculated. The curvature κ is dependent on the distance between the heart of the fiber and the heart of the needle d.

$$\kappa = \varepsilon_{max} / d \tag{4.8}$$

Frenet-Serret formulas with Euler integration are used to translate curvature and torsion into positions along the needle.

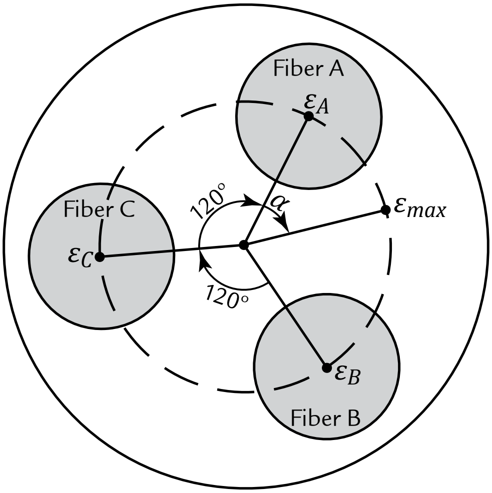

FIGURE 4.3 **Cross section of the inner stylet. ε_A, ε_B, and ε_C are the strains measured in Fiber A, B, and C, respectively. ε_{max} is the maximal strain and α is the direction of the ε_{max} with respect to Fiber A. d is the distance between the heart of the needle and the heart of the fibers.**

4.2.5 Calibration

The FBG-specific constant C in (4.4) was determined for each FBG location using the first twelve data points from both experiments. The theoretical strain distribution was determined for each loading situation. Assuming that there is no torsional loading and the deflections are small (<10% of the length), the needle can be approximated by a cantilever beam. This means that there is no displacement or rotation at the fixed support, and that the strain at the free end is zero. The theoretical ε_{max} at each FBG location was calculated and compared to ε_{max} calculated based on the wavelength measurements. C is calculated for each of the twenty-four loading situations and averaged. In the remaining measurements, $\Delta\lambda_B$ was multiplied by this averaged C to compute ε.

4.2.6 Error estimation of tip position

The absolute error in estimation of the tip position err in direction of the applied displacement is

$$\text{err} = |\Delta y_{est}(x = 189) - \Delta y_t| \tag{4.9}$$

where Δy_{est} (x = 189) is the y position estimated based on the FBG measurements and Δy_t is the actual applied tip displacement.

4.3 RESULTS

Figure 4.4 and Figure 4.5 show the pixel positions that correspond to the wavelengths reflected by two FBGs. On the left, pixel positions of an FBG at Position 1 during the complete first experiment are shown. No disturbance seems to be present and the measurements appear to be repeatable. On the right, pixel positions of an FBG at Position 2 during the complete second experiment are shown. From measurement 15 on, the pixel position seems to be disturbed and the measurements from the same loading situations are fluctuating.

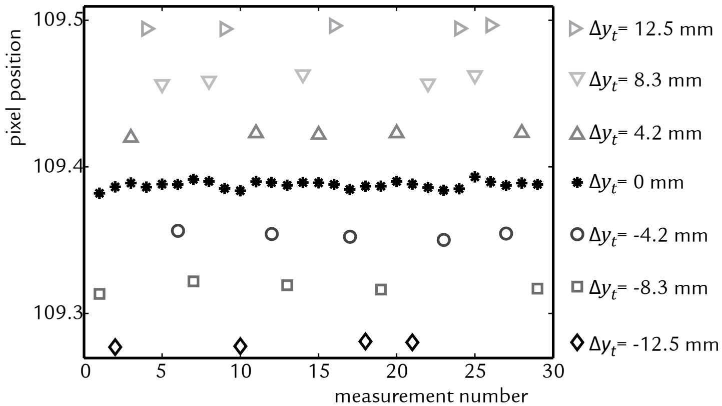

FIGURE 4.4 **Raw data: wavelengths measured with an FBG at Position 1 during the first experiment. Each symbol represents the output of one of the six FBGs.**

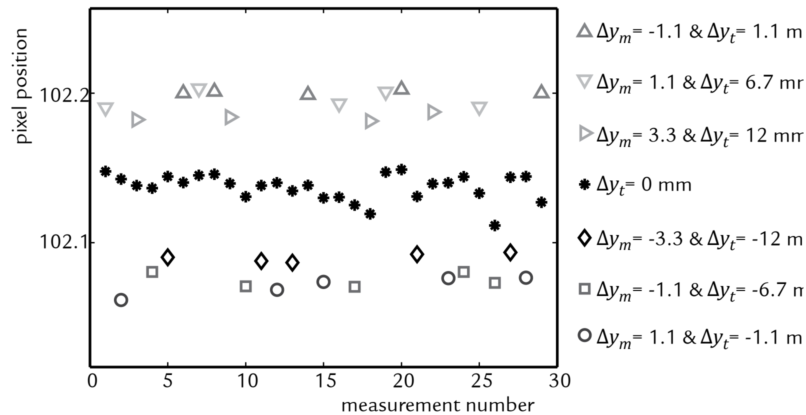

FIGURE 4.5 **Raw data: wavelengths measured with an FBG at Position 2 during the second experiment. Each symbol represents the output of one of the six FBG.**

Figure 4.6 and Figure 4.7 show the theoretical and estimated strain distribution along the needle in the two experiments. The estimated strain distribution follows the theoretical strain distribution, but the deviations in the measured strains from theory are magnified by the regression.

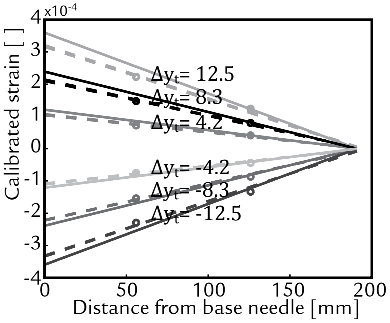

FIGURE 4.6 **Strain distribution along needle in the first experiment with one displacement applied at the tip (Δy_t): theoretical strain distribution (solid lines) and estimated strain distributions (dotted lines) per measured strains (dots).**

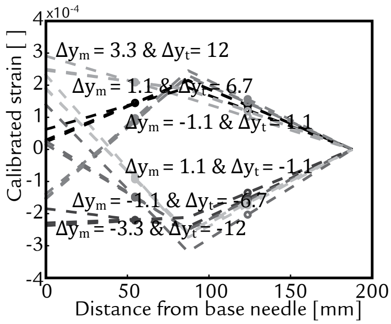

FIGURE 4.7 **Strain distribution along needle in the second experiment with one displacement applied in the middle and one at the tip (Δy_m and Δy_t): theoretical strain distribution (solid lines) and estimated strain distributions (dotted lines) per measured strains (dots).**

In Figure 4.8 and Figure 4.9, the absolute error in estimated y-position of the tip is shown. The mean errors were 0.89 mm and 1.32 mm with standard deviations of 0.42 and 0.48 mm in the first and second experiment, respectively. The total mean error was 1.10 mm. The RMS errors were 0.98 and 1.40 mm in the first and second experiment, respectively.

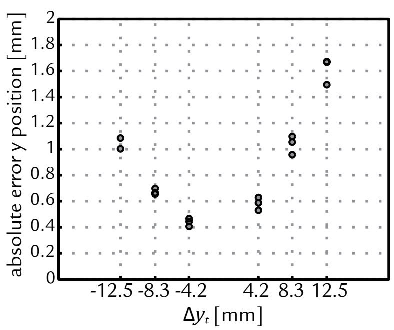

FIGURE 4.8 **Absolute error in estimated defection in y-direction in first experiment in which one displacement is applied to the tip of the needle (Δy_t).**

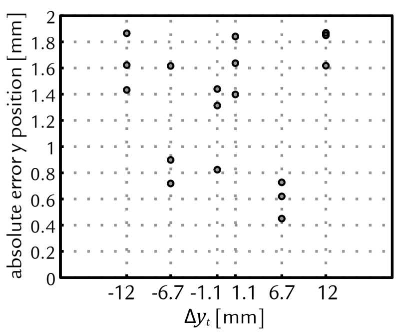

FIGURE 4.9 **Absolute error in estimated defection in y-direction in the second experiment with one displacements applied in the middle and one at the tip (Δy_m and Δy_t).**

4.4 DISCUSSION

A needle deflects when it is inserted in tissue. We incorporated FBGs in a needle to investigate the accuracy with which the tip position of a deflected needle can be estimated based on strain measurements. Deflections up to 12.5 mm resulted in an average error in estimation of the tip position of 1.10 mm.

The required accuracy of positioning of the needle for percutaneous RFA of liver tumors is depending on the size of the lesions. Because the treatment range of RFA is limited, RFA is only effective in lesions with sizes up to 3 cm. When the size of the tumor is close to the treatment range of RFA or when the tumor is very small, more accurate positioning is needed. Khlebnikov et al. [6] report that a 5 mm deviation from advised tip position can already result in inadequate ablation of the tumor tissue. We estimate the required accuracy to be in the order of magnitude of 1 mm. Our results indicate that the accuracy of this technology is suitable for needle tip detection in RFA of liver tumors, although other factors like movement of tissue during needle insertion affect the accuracy of tip positioning as well.

The estimation errors are attributed to the limited number of sensors used. Increasing the number of FBG locations to three or more will result in a reduced error in estimation of the tip position. In addition, the current variability in the placement of the fibers in each groove contributes to a lower accuracy of the measurement. This can easily be overcome by a more accurate alignment of the FBGs during assembly. On top of this, disturbances during the last measurements in the second experiment cause unreliable wavelength measurements, resulting in high errors. The exact cause of this additional variability still needs to be determined, but it was probably due to local heating of the needle and fibers caused by touching.

The RMS errors in the current study were 0.98 mm in case of one applied displacement and 1.40 mm in case of two applied displacements. Park et al. [21] used a similar approach to measure needle deflection and reported an RMS error of 0.26 mm to 0.39 mm in the estimation of tip deflection for deflections up to ±15 mm. They attribute the estimation errors to the limited number of FBGs and to inaccuracy in FBG placement. The exact degree of inaccuracy of sensor placement is not reported by these authors. Possibly, the deviations in sensor placement are larger in the current study, which could explain the larger errors reported here. Differences in the results can also be attributed to the chosen position of the FBGs. The tip position is computed by integrating estimated curvatures along the needle. Consequently, inaccuracies in estimated curvatures closer to the base of the needle have greater effect on the error in estimation of the tip position than those closer to the tip of the needle. Therefore, more accurate strain measurements closer to the base of the needle will result in a more accurate estimation of the tip position. Since in the needle of Park et al. [21] the FBGs are placed closer to the base of the needle, the strain estimations will be more accurate there, which results in a higher accuracy of the estimated tip position.

Despite the limitations mentioned earlier, the accuracy of the estimated tip position of the current device is already comparable to the accuracy obtained with passive tracking based on MR images, but the sample rate is much higher (20 kHz). Görlitz et al. [18] and De Oliveira et al. [20] report an accuracy of 4 and 1.5 mm, respectively, both at an update speed of 1 frame per second. Future devices that incorporate more FBGs will enable even more accurate measurements.

FBG technology cannot replace imaging, because movement of tissue is not registered. Imaging is still needed to provide continuous information about the exact position of the target. Since FBGs are not affected by electromagnetic signals, it is possible to combine MRI with the FBG measurements. MR images can provide accurate information about the target at lower sample rate, whereas the FBG system allows high-frequency measuring of the needle tip position. FBGs incorporated in a needle may also enable measurement of needle-tissue interaction forces. Such development could contribute to tissue characterization and diagnostic purposes in the future.

A robotic system that actively controls the orientation of the needle tip to navigate the needle to the target location may improve the accuracy of tip positioning and also avoid reinsertion after uncontrollable needle bending. Such a system will not prevent natural bending of the needle, but makes use of natural bending or actively bends the needle to navigate to the target location. FBG measurements may offer a suitable method for registering needle tip position automatically for robotic control. Further research is needed to investigate the accuracy with which a robotic system can navigate a needle tip to a target location based on FBG measurements.

REFERENCES

[1] Henken K, Van Gerwen D, Dankelman J, Van den dobbelsteen JJ. *Accuracy of needle position measurements using fiber Bragg gratings.* Minim Invasiv Ther, 2012; 21(6): 408-414.

[2] Chiu ST, Chiu JH, Lui WY, Chau GY, Loong CC, Wu CW. *Prognostic factors affecting long-term survival after partial hepatectomy for human hepatocellular carcinoma.* Chin Med J (Taipei), 1997; 59: 177-185.

[3] Huo TI, Huang YH, Wu JC. *Percutaneous ablation therapy for hepatocellular carcinoma: current practice and future perspectives.* J Chin Med Assoc. 2005; 68(4): 155-159.

[4] Lau WY, Lai ECH. *The current role of radiofrequency ablation in the management of hepatocellular carcinoma a systematic review.* Ann Surg. 2009; 249: 20-25.

[5] Minami Y, Kudo M. *Radiofrequency Ablation of Hepatocellular Carcinoma: A Literature Review.* Int J Hepatol. 2011; Published online 2011 May 11; doi: 10.4061/2011/104685.

[6] Khlebnikov R, Muehl J. *Effects of needle placement inaccuracies in hepatic radiofrequency tumor ablation.* 32nd Annual International Conference of the IEEE EMBC, Argentina, Buenos Aires, 2010.

[7] Misra S, Reed K, Schafer B, Ramesh K, Okamura A. *Mechanics of flexible needles robotically steered through soft tissue.* Int J Robot Res. 2010; 29(13): 1640–1660.

[8] Breedveld P, Scheltes JS, Blom EM, Verheij JEI. *A new, easily miniaturized steerable endoscope.* IEEE Eng Med Biol Mag. 2005; 24(6): 40–47.

[9] Glozman D, Shoham M. *Image-guided robotic flexible needle steering.* IEEE Trans Robot. 2007; 23(3): 459–467.

[10] Glozman D, Shoham M. *Flexible needle steering and optimal trajectory planning for percutaneous therapies.* In: Barillot C, Haynor DR, Hellier P, eds. Lect Notes Comput Sc. Berlin: Springer-Verlag Berlin, 2004; 137–144.

[11] Glozman D, Shoham M. *Flexible needle steering for percutaneous therapies.* Comput Aided Surg. 2006; 11(4): 194–201.

[12] Kallem V, Cowan NJ. *Image guidance of flexible tip-steerable needles.* IEEE Trans Robot. 2009; 25(1): 191–196.

[13] Reed KB, Kallem V, Alterovitz R, Goldberg K, Okamura AM, Cowan NJ. *Integrated planning and image-guided control for planar needle steering.* Proc IEEE/RAS-EMBS Int Conf Biomed Robot Biomechatron. Scottsdale, Arizona, USA; 2008. 819–824.

[14] Tokuda J, Fischer GS, DiMaio SP, Gobbi DG, Csoma C, Mewes PW, Fichtinger G,Tempany CM, Hata N. *Integrated navigation and control software system for MRI-guided robotic prostate interventions.* Comput Med Imag Grap. 2010; 34(1): 3–8.

[15] Xu H, Lasso A, Vikal S, Guion P, Krieger A, Kaushal A, Whitcomb LL, Fichtinger G. *MRI-guided robotic prostate biopsy: a clinical accuracy validation.* Lect Notes Comput Sc. 2010; 13: 383–391.

[16] DiMaio S, Fischer G, Maker S, Hata N, Iordachita I, Tempany C, Kikinis, R, Fichtinger G. *A system for MRI-guided prostate interventions.* IEEE RAS-EMBS International Conference on Biomedical Robotics and Biomechatronics Pisa, Italy; 2006.

[17] Kühn JP, Langner S, Hegenscheid K, Evert M, Kickhefel A, Hosten N, Puls R. *Magnetic resonance-guided upper abdominal biopsies in a high-field wide-bore 3-T MRI system: feasibility, handling, and needle artefacts.* Eur Radiol. 2010; 20: 2414–2421.

[18] Gorlitz RA, Tokuda J, Hoge SW, Chu RX, Panych LP, Tempany C, Hata N. *Development and validation of a real-time reduced field of view imaging driven by automated needle detection for MRI-guided interventions.* In Wong KH, Miga MI, eds. Medical imaging 2010: visualization, image-guided procedures, and modeling. Bellingham: Spie-Int Soc Optical Engineering, 2010.

[19] Wonneberger U, Schnackenburg B, Streitparth F, Walter T, Rump J, Teichgraber UKM. *Evaluation of magnetic resonance imaging-compatible needles and interactive sequences for musculoskeletal interventions using an open high-field magnetic resonance imaging scanner. Cardiovasc Interv Radiol.* 2010; 33(2): 346–351.

[20] De Oliveira A, Rauschenberg J, Beyersdorff D, Semmler W, Bock M. *Automatic passive tracking of an endorectal prostate biopsy device using phase-only cross-correlation.* Magn Reson Med. 2008; 59(5): 1043–1050.

[21] Park YL, Elayaperumal S, Daniel B, Ryu SC, Shin M, Savall J, Black RJ, Moslehi B, Cutkosky MR. *Real-time estimation of 3-D needle shape and deflection for MRI-guided interventions.* IEEE ASME Trans Mechatron. 2010; 15(6): 906–915.

5

Error analysis of FBG-based shape sensors for medical needle tracking

Kirsten R. Henken, Jenny Dankelman, John J. van den Dobbelsteen, Lun K. Cheng, Maurits S. van der Heiden

This chapter is an adaptation of [1], reprinted with permission.

ABSTRACT

BACKGROUND Robotic needle steering requires accurate spatial information about the needle tip. Presumably, fiber Bragg gratings (FBGs) can provide this information at an appropriate update rate. We performed an extensive error analysis to quantify the accuracy of needle tip tracking with FBGs and to assess the suitability of this method for robotic needle steering.

METHOD An FBG-based shape sensing model was determined and simulations were performed to quantify the effect of design parameters on the position accuracy. Inputs that were investigated include accuracy of wavelength measurement and sensor geometry as well as different sensor configurations and interpolation models. For the purpose of validation of the simulations, two needles with two different configurations of FBGs were built and evaluated.

RESULTS The simulations show that the accuracy of FBG-based shape sensing of a needle can be in the order of 10% of the deflection at the tip, depending on the configuration. However, tip deflections that are smaller than approximately 1 mm cannot be detected accurately. Calibration of the needle reduces the bias, but does not improve the accuracy, because of drift in read-out of the FGBs.

CONCLUSION The analysis shows that the combined sources of errors limit the accuracy of tip estimation to approximately 1 mm, although the accuracy is influenced by the sensor configuration as well. This accuracy is suitable for common medical applications like taking biopsies or performing ablation.

5.1 INTRODUCTION

Needle insertion in soft tissue has numerous medical applications, including biopsy, ablation and brachytherapy. Several image-guided robotic systems for needle insertion have been proposed to increase the target accuracy, reduce treatment time, and limit the burden to patients and clinical staff [2-5]. These systems require accurate information about the location of the needle with respect to the target in order to navigate the needle with high precision.

Since needle interventions are usually image-guided, the tip position could be retrieved from the US, MR [4] or CT images. However, contrast in soft tissue is poor in US and CT, the update rate in MRI is too low for high-precision robotic needle steering [6, 7], and CT exposes patients and clinical staff to radiation. A different option is to model the needle shape based on forces and torques measured at the handle of the needle, but this requires accurate information about the forces that act on the needle inside the body as well. These forces are difficult to predict, since tissue is inhomogeneous and the properties are specific for each patient. Complicated loading patterns can occur, which result in multimodal deflection of the needle. In case the intervention is guided by MRI, an active tracker could provide spatial information about the tip [8, 9]. However, the complete shape of the needle cannot be registered with this method.

This research focuses on optical tracking of the shape of a needle based on fiber Bragg gratings (FBGs) [10, 11]. An FBG is a periodical change or grating applied to the core of a glass fiber, which reflects one specific wavelength [12]. This wavelength changes when the fiber is elongated or compressed due to mechanical loading or due to a change in temperature or humidity. The small size of the fibers and the possibility to incorporate multiple FBGs in one fiber make them suitable for implementation in small devices like needles. In addition, FBG technology is purely based on optics and does not interfere with other electrical or magnetic systems such as MRI or electrosurgery. The use of FBGs in medical instruments has already been proposed in literature for the purpose of force, pressure, and shape sensing [13-17].

Shape sensing requires at least three fibers with a number of FBGs each to be incorporated in the needle. When the FBGs in the fibers are aligned, strain is measured at three locations within one cross-section, and the bending radius and the direction of bending at that position can be reconstructed. Interpolating the bending radii and directions and converting it to deflection enables shape estimation and consequently tip position estimation. The accuracy with which the shape can be estimated depends on numerous factors that include the sensor configuration (geometry of the needle and the number and positioning of FBGs) and the interpolation method. Previous research [10] has shown that the tip position of a 20 cm needle can be estimated with an accuracy in the order of 1 mm. It is generally assumed that even higher accuracy can be obtained by adding sensors and by optimizing the interpolation model. However, the final endpoint accuracy is the cumulative result of multiple sources of errors and will not only be determined by these two factors.

The aim of this research is to determine the highest accuracy that is currently achievable and to identify the appropriateness of FBG-based shape sensing for high-precision robotic needle systems. First, the model for estimating the shape of a needle based on FBG measurements is defined, together with the required input parameters and potential error sources. The input parameters include the sensor configuration (number and position of FBGs) and the interpolation model that estimates deflection in between the sensor locations. The error sources include the read-out of the wavelengths reflected by the FBGs and the accuracy with which the sensors are assembled. Second, simulations are performed to optimize the geometry and interpolation model and to quantify the effect of the error sources on the accuracy. Third, accuracy of shape sensing is simulated for two specific designs that are built and evaluated in an experimental setting. The first prototype is a needle that is equipped with three separate fibers as proposed in [10]. The second prototype consists of three fibers that are glued together. This triplet can be introduced in the lumen of a needle and serve as an independent shape sensor [18].

5.2 MATERIALS AND METHODS

5.2.1 Shape Sensing Model

For the purpose of shape sensing with FBGs, the output of the FBGs needs to be translated to positions in 3-D space. This shape sensing model is schematically presented in Figure 5.1 and will be explained thoroughly in this section.

The grating period (Λ) in an unstrained FBG determines the Bragg wavelength (λ_B) that is reflected,

$$\lambda_B = 2n_{eff}\Lambda \tag{5.1}$$

where n_{eff} is the effective refractive index. When stress results in strain (ε) or when the temperature changes (ΔT), the FBG will elongate and the reflected wavelength will shift ($\Delta\lambda_B$) accordingly

$$\Delta\lambda_B/\lambda_B = (1-P_\varepsilon)\ \varepsilon + (\alpha_T+\xi)\ \Delta T \tag{5.2}$$

where P_ε, α_T and ξ are the photo-elastic factor, the thermo-expansion coefficient and

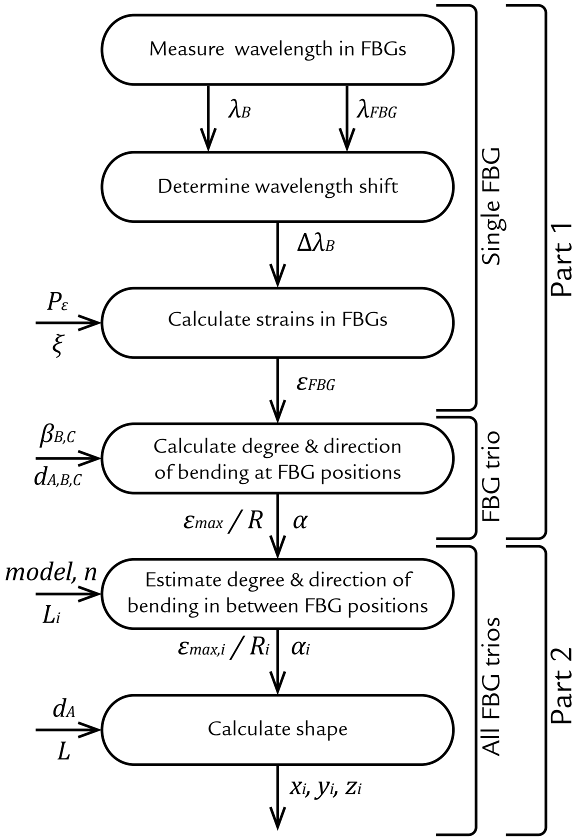

FIGURE 5.1 **Flow scheme of shape sensing model with a finite number of FBGs in three fibers. The strain in each FBG (ε_{FBG}) is determined based on the shift in wavelength ($\Delta\lambda_B$) reflected by the FBG. By combining the strains of the FBG of one trio, the degree of bending (ε_{max} or R) and the direction of bending (α) at the location of the FBG trio can be determined. After interpolating the degree and direction of bending in between the trio positions, the shape can be reconstructed.**

thermo-optic coefficient of the FBG, respectively. The effect of temperature is disregarded in this work, but elaborated on in [18]. The photo-elastic factor P_ε or photo-elastic coefficient $k = 1 - P_\varepsilon \approx 0.78$ can be found by calibration.

Bending can only be detected when the FBGs are placed away from the neutral bending line, which is the case in the two prototypes. A schematic cross section of such a configuration is shown in Figure 5.2. The three FBGs in the three fibers in one cross section form an FBG trio. By relating the strain in the FBGs of one trio, the degree and the direction of bending can be determined. The degree of bending is represented by the maximal strain (ε_{max}) within the cross section of the needle. The direction of bending (α) is determined with respect to Fiber A. As described in [10], ε_{max} and α are implicitly defined by

$$\varepsilon_A = \varepsilon_{max} \cos(\alpha) + \varepsilon_0 \tag{5.3}$$

$$\varepsilon_B = d_A/d_B \ \varepsilon_{max} \cos(\beta_B + \alpha) + \varepsilon_0 \tag{5.4}$$

$$\varepsilon_C = d_A/d_C \ \varepsilon_{max} \cos(\beta_C + \alpha) + \varepsilon_0 \tag{5.5}$$

in which ε_A, ε_B, and ε_C are the strains in Fiber A, B, and C at the location of the FBG trio, respectively. β_B and β_C are the orientations of Fiber B and C with respect to Fiber A. d_A, d_B, and d_C are the distances between the centerline of each FBG and the centerline of the needle or triplet. ε_0 includes strain due to axial stress and axial temperature changes. ε_0 equals zero in case of pure bending at a constant temperature. Axial stresses and axial gradients in temperature result in a uniform wavelength shift for all three FBG sensors in the FBG trio. This is accounted for in ε_0 and does not affect the shape estimation. On the contrary, the estimated degree and direction of bending is affected by radial temperature gradients, where different wavelengths are measured by the FBGs in one trio. This situation is less likely to occur because of the small diameter of the sensor. Therefore effect of temperature is not further elaborated on in this work. The bending radius R is the radius of the curvature of the needle and is a function of the maximal strain.

$$R = d_A/\varepsilon_{max} \tag{5.6}$$

The geometrical properties (β_B, β_C and d_A, d_B, d_C) can be found by calibration, but the variation in d_A, d_B, d_C cannot be distinguished from the variation in k.

By interpolation, the degree and direction of bending can be determined at n locations along the needle or triplet. Possible interpolation models include a piecewise linear fit, a second order polynomial fit, a fit of a polynomial of highest order, and a spline fit. The shape of the needle is geometrically dependent on the n bending radii that relate to the maximal strain and the n bending directions (Figure 5.3). For each of the n segments, the displacement in three directions (d_x, d_y and d_z) is calculated

$$d_x = \mathrm{L/n} \sin(\alpha) \sin(\varepsilon_{max}(\mathrm{L/n})/2d_A)) \tag{5.7}$$

$$d_y = \mathrm{L/n} \cos(\alpha) \sin(\varepsilon_{max}(\mathrm{L/n})/2d_A) \tag{5.8}$$

$$d_z = \mathrm{L/n} \cos(\varepsilon_{max}(\mathrm{L/n})/2d_A) \tag{5.9}$$

where d_A is the distance between the centerline of the needle and the centerline of FBG A. The displacements are rotated and summed to obtain the estimated 3-D position along the needle or triplet.

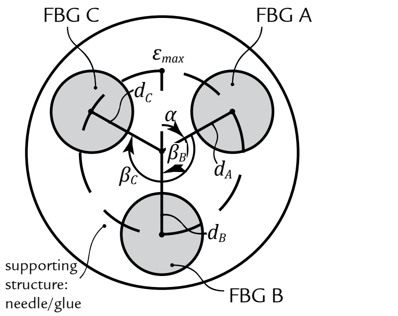

FIGURE 5.2 **Cross section of the needle or triplet at the location of a sensor trio. FBG A, B and C are the sensors that measure the strains ε_A, ε_B, and ε_C, respectively. ε_{max} is the maximal strain due to bending at a distance d_A from the centerline, that is determined based on strains ε_A, ε_B, and ε_C. α is the direction of ε_{max} with respect to FBG A and β_B and β_C are the locations of FBG B and C with respect to FBG A.**

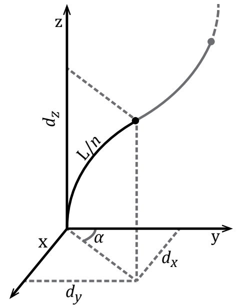

FIGURE 5.3 **Geometry of shape reconstruction based on degree and direction of bending. The deflection (d_x, d_y, and d_z) at one of the n locations along the needle with length L depends on the radius R and the angle α of the needle at that location. The 3-D shape is reconstructed by rotating and summing these deflections.**

5.2.2 Simulations

The aim of the simulations was to quantify the maximum theoretically achievable accuracy of the shape sensor as configured by the two prototypes described in next section, based on assumed inaccuracies of the input parameters for shape sensing explained in the previous section. The simulations were divided in two parts that are indicated in Figure 5.1.

Part 1 encompasses the measurement of the reflected wavelengths, the calculation of strain in the FBGs based on these wavelengths, and the estimation of the degree and the direction of bending at the locations of the FBG trios that is based on the strains in the FBGs. The simulations in this part aim to investigate the effect of the resolution of the wavelength measurement and of the inaccuracies in the assumptions about the geometrical properties introduced during assemblage on the estimated bending.

Part 2 includes the estimation of bending in between the FBG locations and the translation of bending to a shape. The simulations in part 2 aim to investigate the effect of the interpolation model and the distribution and number of FBG trios for the purpose of optimization of shape sensors in general. In addition, the effect of inaccurate alignment of the FBGs within a trio is evaluated.

PART 1: SINGLE FBG AND FBG TRIO

The wavelengths that are reflected by the FBGs in a trio (λ_{FBG}) were simulated by

$$\lambda_{FBG,A} = \lambda_{B,A} + \delta\lambda_{in} \cos\alpha_{in} \tag{5.10}$$

$$\lambda_{FBG,B} = \lambda_{B,B} + \delta\lambda_{in} \cos(2\pi/3 + \alpha_{in}) \tag{5.11}$$

$$\lambda_{FBG,C} = \lambda_{B,C} + \delta\lambda_{in} \cos(4\pi/3 + \alpha_{in}) \tag{5.12}$$

where λ_B are the known Bragg wavelengths and $\delta\lambda_{in}$ and α_{in} are the maximal simulated wavelength shift and bending direction, respectively.

The following simulations were executed to find the separate and combined effect of inaccuracies in the parameters on the bending radius and direction. In each step in each of the simulation, variables and errors are set to new values that are selected from a range of values. To quantify the effect of the inaccuracies, the simulated degree (R) and direction of bending (α) are calculated in- and excluding the inaccuracies and the resulting R's and α's are compared to each other.

Resolution of the interrogator:
- $\delta\lambda_{in}$ was stepwise (10^6 steps) increased from 0 to 0.5 nm or 0.24 nm for needle and triplet, respectively, and α_{in} is set to 0 rad. These wavelengths correspond to a realistic range of bending radii for the needle and triplet.
- Inaccuracies of 6 and 4 pm were added to the λ_{FBG} for the needle and triplet, respectively. These inaccuracies correspond to the resolutions of the interrogators. Other inaccuracies were set to zero.

Inaccuracies in the photo-elastic coefficient (k) and the geometrical properties (β_B, β_C and d_A, d_B, d_C):
- $\delta\lambda_{in}$ was set to a value that was randomly selected from a uniform distribution between -0.5 and 0.5 nm or 0.24 and 0.24 nm for the needle and triplet, respectively. α_{in} was set to a value randomly selected from a uniform distribution between 0 and 2π.
- The inaccuracy of one of the variables of interest set to a value randomly selected from a uniform distribution with a range that is stepwise enlarged from 0 to 0.04 for k, from 0 to 0.04 mm for d, from 0 to 4° or 40° for β for needle or triplet, respectively. The inaccuracies for the other variables were set to zero.
- The simulation was repeated 10^4 times for each step in the range of each variable for both the needle and triplet.

Combined effect of the inaccuracies:

- $\delta\lambda_{in}$ was set to a value randomly selected from a uniform distribution between -0.5 and 0.5 nm or -0.24 and 0.24 nm for the needle or triplet, respectively.
- The inaccuracies were randomly selected from a normal distribution according to the realistic 3σ-values from Table 5.1.
- The simulation was repeated $50 \cdot 10^4$ times for both the needle and the triplet.

PART 2: ALL FBG TRIOS

The effect of the interpolation model, the number of sensors, the distribution of the sensors, and the inaccuracy in placement of the sensors along the entire instrument on the estimated shape were simulated in part 2. In these simulations, the shape of the needle was determined analytically and compared to the shape that would be estimated with the actual model that is based on bending radii at the sensor locations, as shown in Figure 5.4.

$$q(x) = \sum_{(i=1)}^{10} a_i \sin(i\pi x/L + \varphi_i) \tag{5.13}$$

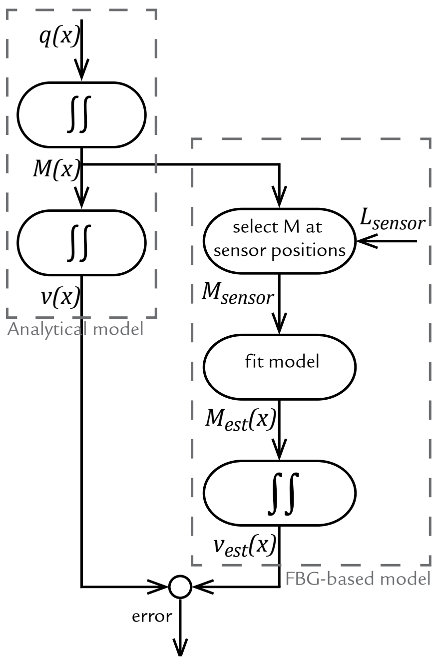

FIGURE 5.4 **Schematic overview of the approach in the second part of the error analysis. A distributed load $q(x)$ is simulated to be exerted on the needle. In the analytical model, the moment $M(x)$ along the needle is derived by integrating $q(x)$ twice based on which the shape $v(x)$ can be derived by integrating twice more. In the FBG-based model, the moments M_{sensor} at the locations of the sensor trios L_{sensor} are selected from $M(x)$, because the moments at the sensor trios correspond to the maximal strain, shown in (5.6) and (5.14). After interpolating in between these position (for example by fitting a spline), and integrate twice, the shape of the needle can be reconstructed.**

Only 2-D loading situations were considered to limit the computation time. The needle was approximated as a cantilever beam with a flexural modulus E that was measured to be 120 GPa and a moment of inertia $I = \pi/(32D_{out}^{\ 4})\ m^4$ that is clamped at the base. A distributed force $q(x)$ was simulated to act on the needle where a_i is the amplitude that is selected randomly from a uniform distribution between 0 and 1 and φ_i is the phase that is randomly selected from a uniform distribution between 0 and 2π. $q(x)$ represents the mechanical interaction between needle and tissue well, because it consists of multiple distributed forces with randomly selected amplitudes, periods and phases, which results in multimodal deflection. This distributed force was integrated twice to find the moment $M(x)$ along the needle, which is proportional to the bending radius R. The theoretical needle shape $v(x)$ was determined by integrating twice more. The simulated deflections at the tip did not exceed 10% of the length of the needle or triplet. In the FBG-based model, the needle shape was estimated by selecting the moments M_{sensor} at the locations of the sensor trios, interpolating in between these locations, and integrating twice. M_{sensor} is related to the bending radius at the location of the sensor location (R_{sensor}) by the stiffness of the needle or triplet.

$$M_{sensor} = R_{sensor} \cdot EI \tag{5.14}$$

The following simulations were executed to find the separate and combined effect of the interpolation model, the number of sensors, the distribution of the sensors, and the inaccuracy in placement of the sensors on the estimated needle shape. For each simulation the needle shape and tip position were calculated based on the analytical model and compared to the needle shape and tip position simulated with the FBG-based model. Each set of simulations was repeated for two to nine sensor trios to quantify the effect of adding sensor trios to the needle.

Interpolation model:

- The interpolation model was piecewise linear, polynomial up to 3rd order, polynomial with highest possible order, or spline.
- Sensor trio distribution was optimized by means of least-squared-error fit.
- 50 simulations per model were executed.

Sensor trio distribution:

- The sensor distribution was optimized by means of a least-squared-error fit or equal with the first sensor located at the base or equal with the first sensor located away from the base.
- Splines were used as interpolation model.
- 50 simulations per distribution were executed.

Inaccurate placement of the sensor trios:

- An inaccuracy was randomly selected from a uniform distribution and added to the assumed sensor position. The range of the distribution was stepwise increased from 0 to 10 mm.
- The actual sensor distribution and spline as interpolation model were used.
- 104 simulations per range were executed.

Combined effect:

- The amplitude a_i was set to a value randomly selected from a uniform distribution between 0 and 2 N/m and between 0 and 12 N/m for needle and triplet, respectively. The phase φ_i was set to a value randomly selected from a uniform distribution 0 and 2π. The distributed forces resulted in a realistic deflection at the tip (up to 16 and 5.8 mm for needle and triplet, respectively).
- The actual sensor distribution of the needle with optical fibers and of the optical fiber triplet were used as input. Interpolation was performed by means of a spline.
- The inaccuracies in sensor position were set to multiplication factor randomly selected from a normal distribution according to the 3σ-values in Table 5.1, which were retrieved from the first simulations.
- $50{\cdot}10^3$ simulations for needle and triplet were executed.

TABLE 5.1 **Simulated inaccuracies in sensor**

	Variation (3σ) in	Needle	Triplet
λ	Measured wavelength	$6{\cdot}10^{-6}$ mm	$4{\cdot}10^{-6}$ mm
k	Photoelastic coefficient	0.01	0.01
β	Relative orientation of fibers	2°	20°
d	Distance between the centerline of the needle and the centerline of the FBG	0.02 mm	0.02 mm
L_{sensor}	Position of FBG trio	2 mm	2 mm
M_{sensor}	Measured moment at sensor trio	6%	24%

5.2.3 Prototypes

NEEDLE WITH OPTICAL FIBERS

Three grooves with a diameter of 0.3 mm were milled at an angle of approximately 120° with respect to each other over the length of the inner stylet of a trocar needle (18G/20cm, Cook Medical, Bloomington, USA) with a diameter of 1.35 mm. An optical fiber equipped with five FBGs (HI-780 (acrylate recoating), Corning Incorporated, Corning, USA) was glued in each of the grooves in such way that the FBGs were aligned. Dimensions of the needle and the locations of the FBGs are listed in Table 5.1. The minimal bending radius of the needle is 500 mm. Wavelengths reflected by the FBGs are read-out with a Deminsys interrogator (Technobis, Uitgeest, the Netherlands) that has an accuracy of 6 pm, which was verified experimentally.

OPTICAL FIBER TRIPLET

Three fibers (Polyimide coated SMF-28 fiber, Alxenses, Hong Kong) with three FBGs each were glued together. First the coating of the fibers was removed over a length of 100 mm symmetrically around the FBGs, reducing the fiber diameter to 0.125 mm. Then two of the fibers were placed adjacent in a 0.3 mm groove in an acrylic assemblage tool and polyimide glue was added. After that the third fiber was placed on top of the two fibers and glue was added again. The space between the fibers was minimized to ensure accuracy and linearity, despite the large difference between the Young's moduli of the fibers and the glue (75 GPa and 3 GPa, respectively). The glue was cured in an oven according to a heating cycle further described in [18]. Finally, the excessive glue is removed with a squeegee to ensure a constant thickness along the triplet.

Dimensions of the triplet and the locations of the FBGs are listed in Table 5.2. The minimal bending radius of the triplet is 25 mm. The three fibers are connected to an interrogator (MicronOptics - sm130, Alanta, USA) that has an experimentally determined accuracy of 4 pm.

TABLE 5.2 Specifications of the needle with optical fibers (18G/20cm trocar needle) and the optical fiber triplet.

	Property	Needle	Triplet
d_{out}	Outer diameter of instrument	1.35 mm	0.22 mm
λ_B	Typical Bragg wavelength	850 nm	1550 nm
P_e	Photo-elastic coefficient	0.22	0.22
L	Length of instrument	200 mm	100 mm
-	Number of FBG trios	5	3
L_{sensor}	Positions FBG trios	20, 60, 100, 140, 180 mm	23, 46.5, 70 mm
d	Distance between the centerline of the needle and the centerline of the FBG	0.35 mm	0.10 mm

CALIBRATION

The prototypes were calibrated to determine the actual geometrical properties of the FBG trios (Figure 5.5). The calibration procedure was slightly different for the needle than for the triplet. The needle was positioned in 1.4 mm grooves (straight or with a constant radius of 350 or 700 mm) and rotated stepwise around its longitudinal axis from 0° to

350° with steps of 10° to simulate a varying bending direction, while the wavelength shifts in the FBGs were measured for 10 s at a frequency of 100 Hz. The Bragg wavelength (λ_B) was assumed to be equal to the average of the wavelengths that were reflected by the FBGs while the needle was located in the straight groove. For the measurements where the needle was located in one of the curved grooves, strains in the FBGs were calculated according to (5.2). Plotting the strains that occurred in two FBGs within one trio results in elliptical curves. The angulation of the ellipse corresponds to the orientation of the FBGs relative to each other. The horizontal and vertical extremes relate to the distances of the two FBGs to the centerline of the sensor.

Detailed information about the calibration of the triplet is available from [18]. The triplet was first positioned in a straight v-shaped groove to find the Bragg wavelength (λ_B). After that, the triplet was clamped on one side and manually rotated continuously along a ring with a radius of 85 mm, while the wavelength shifts in the FBGs were measured at a frequency of 250 Hz. Approximately 5.5 rotations were measured in approximately 150 s. The geometrical properties of the triplet can be determined based on these measurements in a similar way as explained for the needle. However, compensation is needed in this set-up for the fact that the bending radius is linearly increasing along the triplet.

Inaccuracies in d and k cannot be distinguished, so k was assumed to be exactly 0.22 and deviations in k were incorporated in the calibration of d. The actual geometrical properties (β_B, β_C and d_A, d_B, d_C) were derived from the parameters of the fitted ellipse.

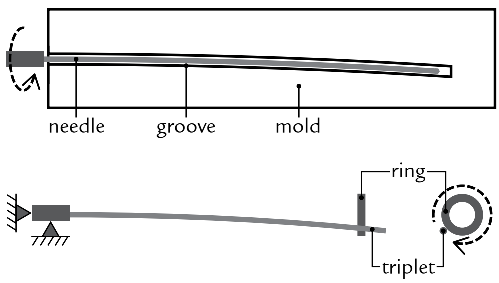

FIGURE 5.5 Schematic view of the set-ups for calibration. The needle is calibrated by rotating the needle in a groove with a constant radius. The triplet is calibrated by rotating the tip around a ring with constant radius.

5.3 RESULTS

5.3.1 Simulations

PART 1: SINGLE FBG AND FBG TRIO

The relative error in estimated bending radius is the error in estimated bending radius due to inaccuracies in the variable(s) relative to the bending radius. Note that the bending radius is inversely proportional to the maximal strain (5.6) and the amount of deflection. The relative error in estimated bending radius due to inaccuracies in wavelength measurement is shown in Figure 5.6 as a function of the bending radius. Errors in bending radius and direction are inversely proportional to the wavelength shifts in the FBGs. For large radii (when the deflection is small and the needle or triplet is almost straight) the error is very large, because the shift in wavelength is smaller than the resolution of the measurement systems. An error smaller than 1% caused by an inaccurate wavelength measurement occurs at radii smaller than 38 m, which corresponds to a tip deflection 0.5 mm in case of a constant bending radius along a 20 cm needle. This means that in this case, the degree of bending can be estimated with a relative accuracy of at least 1% for tip deflections larger than 0.5 mm when only disturbances in wavelength are considered.

The errors in bending radius and direction of bending are linearly related to the errors in the assumed photo-elastic constant and geometry. Errors due to inaccuracies in assumed k only occur when differences in FBG-specific k's are present within a trio. The effect of the inaccuracies in assumed k and β on the errors in the bending radius and direction are

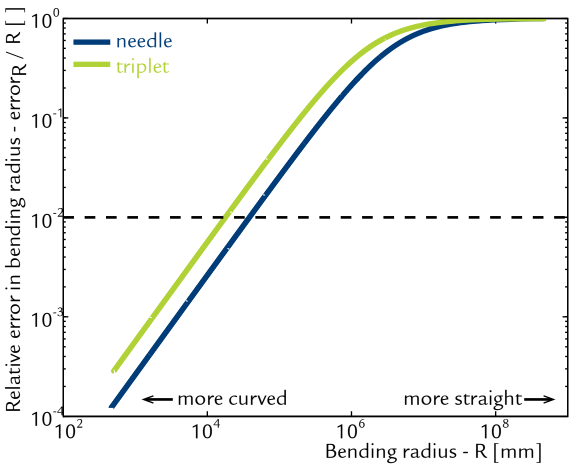

FIGURE 5.6 **Relation between bending radius and the error in bending radius estimated based on the wavelength measurements in the FBG trio. When the bending radius is large (and the deflection is small), the wavelength shift in the FBGs becomes smaller than the resolution of the interrogators, which results in very large errors.**

TABLE 5.3 Overview of the effects of expected inaccuracies in assumption of variables (d, k, and β) on the relative error in bending radius and absolute error in bending direction.

	Inaccuracy in	Relative error R	Absolute error α
Needle	d = 0.02mm	6.5%	5.9°
	k = 0.01	1.3%	0.5°
	β = 2°	3.1%	2°
Triplet	d = 0.02mm	23.9%	19.7°
	k = 0.01	1.3%	0.5°
	β = 20°	31.6%	20°

the same for the needle as for the triplet. However, the inaccuracy in β in the triplet is expected to be larger, because it is more difficult to orient the fibers precisely when there is no guiding structure like a needle with grooves. The maximal errors in bending radius and bending direction that occur at expected inaccuracies in assumed variables are shown in Table 5.3.

The combined effect of all inaccuracies in wavelengths, photo-elastic constant, and geometry is shown in Figure 5.7 for bending radii that range from approximately 0.5 m to $5 \cdot 10^6$ m. Errors in bending radius and direction of bending increase exponentially when the bending radius increases. Outliers are not shown, because they occur at large bending radii where the needle can be assumed to be straight. The maximum error in relative bending radius is 5.7% and 24% for the needle or triplet, respectively. The maximum error in bending direction is 2.4° and 12° for needle and triplet, respectively. The errors for the triplet are larger than for the needle due to smaller d and larger expected error in β.

PART 2: ALL FBG TRIOS

In case the interpolation is performed by means of a piecewise line fit, a highest order polynomial fit or a spline fit, the error decreases when an extra sensor trio is added. This is not the case for the polynomial interpolation with a maximal order of 3 for 5 FBG trios or more. The shape errors are lowest in case interpolation is executed based on a polynomial with the highest order that is possible (depends on number of sensor trios) or based on splines, but interpolation with a highest order polynomial is less stable at the boundaries.

One single optimal sensor distribution does not exist in practice, because the optimal distribution is different for each loading situation. Placing a sensor trio at the base of the instrument improves the accuracy, but in practice the base of the needle moves during insertion. The error resulting from interpolation for a needle with equally distributed sensors is minimal when the first sensor is located at the base and increases as the first sensor moves away from the base.

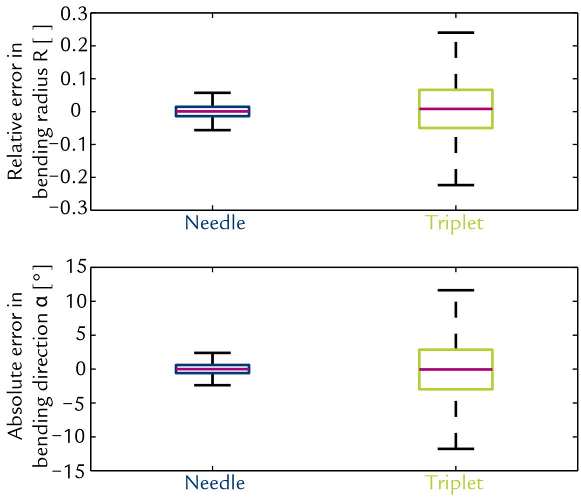

FIGURE 5.7 **Simulated effect of inaccuracies in measured wavelengths and geometry (n = 50·10^4) on bending radius and direction. Bending radius (ranges between 0.5 m and 5·10^6 m) can be estimated with an accuracy of 5.7% and 24% for the needle and triplet, respectively. Bending direction (ranges between 0 and 2π) can be estimated with an accuracy of 2.4° and 12° for the needle and triplet, respectively.**

The effect of the inaccuracies in the locations of the sensor trios is related to the error that is introduced by interpolation. When the inaccuracy of sensor placement is 2 mm, the error estimated shape is 6.3% or 6.1% of the interpolation error for the needle or triplet, respectively. The combined effect of the errors in shape estimation due to inaccuracies in estimated bending radius and sensor position and due to interpolation are shown in Figure 5.8. Cases with a tip deflection smaller than 1 mm are excluded, because the errors are larger for small deflections and the needle can be assumed to be straight (Figure 5.6). The maximum error in estimation of the tip position is 7.1% and 46% for the needle and triplet, respectively.

5.3.2 Calibration

The calibrated geometry of the FBG trios in the needle and triplet is shown in Figure 5.9. Only the calibrated geometries of the first two FBG trios are shown for the needle with optical fibers. Table 5.4 shows the geometries of the needle that are based on the measurements in the groove with a radius of 700 mm and 350 mm.

The fibers were expected to be placed 0.35 mm and 0.10 mm away from the centerline of the needle and triplet, respectively, and oriented in angles of 120° with respect to each other. The calibrated distance of the fibers to the centerline of the needle range from 0.15 mm to 0.32 mm and the orientation of the fibers deviate op to 16.1° from their expected orientation. This shows that accurate assembly is difficult and that calibration is necessary.

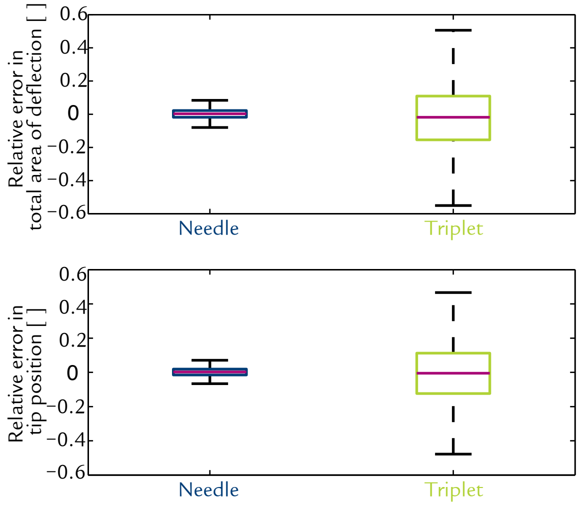

FIGURE 5.8 **Simulated effect of inaccuracies in sensor position, bending radius and direction at sensor positions and of interpolation on the estimated shape and tip position of the needle ($n=50\cdot10^3$). The tip position can be estimated with an accuracy of 7.1 and 46% for the needle and triplet, respectively.**

In addition, different geometries are found for different calibration radii. Possible causes include temperature differences during the calibration measurements, drift in the interrogator, and variations in strain transfer through the glue. This indicates that this calibration method does not improve the accuracy with which the geometry can be defined.

5.4 DISCUSSION

The aim of this research was to quantify the accuracy with which the shape of a needle can be reconstructed based on FBG measurements and to identify the limitations of FBG-based shape sensing. Therefore, the effect of various error sources (the resolution of the

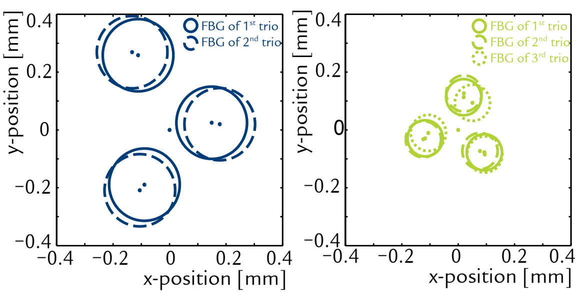

FIGURE 5.9 **Calibrated geometry of the needle for a constant calibration radius of 700 mm (left) and of the triplet for a constant calibration deflection of 8.5 mm (right).**

TABLE 5.4 Calibrated geometry of the needle with optical fibers based on two different calibration radii (700 mm and 350 mm)

		Radius of 700 mm		Radius of 350 mm	
		d [mm]	β[°]	d [mm]	β [°]
Fiber A	Trio 1	0.2815	0	0.3068	0
	Trio 2	0.2999	0	0.3222	0
Fiber B	Trio 1	0.2091	131.5	0.2051	128.5
	Trio 2	0.2337	127.0	0.2302	124.6
Fiber C	Trio 1	0.1512	256.1	0.1609	251.1
	Trio 2	0.1787	250.2	0.1865	249.2

read-out of the reflected wavelengths and inaccuracies in the geometry of the sensor), the sensor configuration (number and location of FBGs) and the interpolation model were simulated. In addition, two prototypes (a needle equipped with optical fibers and an optical fiber triplet) were fabricated and evaluated by simulations and in practice.

The simulations indicate that with the current state-of-the-art the tip position can be estimated with an accuracy of 7.1% and 46% for the needle and triplet, respectively, which is based on the maximal relative error. The actual error can be lower in practice, but is dependent on multiple factors (i.e. shape and geometry of the needle) and cannot be predicted on beforehand. Accuracy of shape sensing with the needle is much higher than with the triplet, because geometrical inaccuracies are relatively smaller for the needle. In addition, the wavelength shifts in the needle are larger for the same bending radii, because the fibers are placed further away from the neutral bending line. On the other hand, the triplet can be bended more without exceeding the maximally allowable strain in the fibers (1% for glass) because of this. Torsion also limits the accuracy of shape sensing with a triplet. The triplet has preferred bending directions, because the cross section is not circularly symmetrical and the torsional stiffness is limited. This disadvantage does not occur in the other configuration, because the optical fibers are supported by the torsional stiff needle.

Other main factors that should be taken into account when optimizing the shape sensor include the accuracy of wavelength measurement with the interrogator, the precision of manufacturing and calibration and the number of sensors. Limited accuracy of wavelength measurements is especially a problem for small deflections. When the needle is almost straight, the wavelength shift in the FBGs is of the same magnitude as the resolution of the interrogator, which results in very inaccurate estimation of the degree and direction of bending. The accuracy is further affected by drift in the interrogators used in this study, which is due to environmental factors that include heating of the interrogation system.

Additionally, the reflected wavelengths themselves are affected by other factors than the degree and direction of bending of the instrument. These factors include losses in strain transfer through the glue, losses of light in the fiber due to bending, and changes in temperature and humidity. A threshold for the wavelength shifts can be incorporated in the control scheme, below which the instrument is assumed to be straight. To actually improve the accuracy of FBG-based shape sensing, more stable read-out of the FBGs is necessary.

Errors in assumed geometry affect the accuracy of shape sensing greatly. Calibration identifies the actual geometry and reduces the bias, but does not improve the accuracy. However, accurate alignment of the FBGs in the longitudinal direction of the instrument will affect the accuracy positively. In addition, precisely assembling the fibers in the instrument allows for a sensor that is according to the original design and required measurement range. When the read-out of the reflected wavelength is more stable, calibration of the needle will provide more certainty about the actual geometry of the shape sensor.

The accuracy of shape sensing increases when an FBG trio is added to the instrument, but the effect becomes small when using in excess of five FBG trios for a 20 cm needle. When shape sensing is integrated in longer instruments (e.g. laparoscopic tools), more FBGs are needed to achieve sufficient accuracy. Besides this, the configuration of the fibers needs to be optimized for the range of bending radii that are expected to occur in such instrument (i.e. place the fibers away from the centerline of the instrument to measure small deflections and the other way around).

Other FBG-based shape sensors are becoming available in the (near) future as well. These include multicore fibers and triplets of small-diameter fibers. The distances between the FBGs in such sensor configurations are even smaller than in the triplet discussed in this work and thus smaller wavelength shifts will occur. Consequently, a higher measurement accuracy of the wavelength shifts can be required to detect large radii. Then again, multicore fibers or triplets of small diameter fibers are circularly symmetrical, which will limit the torsion problems. In addition, challenges in gluing of the fibers are avoided when a multicore fiber is readily available. These multicore fibers or small diameter fiber triplets can be introduced separately in existing instruments and are appropriate for instruments that experience relatively large deflections. A shape sensor of plastic fibers will ease the assembly and make other sensor configurations possible, because plastic fibers allow for higher strains and are less brittle. Such sensors are more suitable for regular use in dynamic systems in daily practice, because they are less prone to damage due to extensive bending.

The accuracy with which the tip of the needle can be estimated based on FBG measurements is in the order of magnitude of 1 mm. In practice, the accuracy might be lower than expected on the basis of the simulations, because the simulations only accounted for 2-D deformations. In addition, temperate changes, drift in the read-out, and variations in the strain transfer in the glue are not accounted for in the simulations. However, practical experiments [10] have shown that the order of magnitude of 1 mm is realistic.

The reported accuracy is slightly better compared to the accuracy of 4 mm and 1.5 mm at an update rate of 1 frame per second that has been reported for passive needle tip tracking based on MR images reported by [6] and [7]. Spatial resolution of coil-based active tip tracking is in the order of 1 mm [8, 9]. Alternatively, a resolution smaller than 0.1 mm is achievable in a measuring time of 0.3 s with active tracking with a silicon chip of less than 2 mm^3 [19]. The drawback of all active tracking systems is that no information about the shape of the complete instrument is available, unless multiple trackers are integrated, which requires space for wiring in the instrument.

Instead of feeding shape information back to a robotic system, the control system can also be based on a predetermined path planning. Such a system requires accurate information about the tissue and the needle and about the interactions between the tissue and needle on beforehand [20]. This information is difficult to obtain, because the penetrated tissue is inhomogeneous and differences in tissue characteristics are present between human beings. For example, [21] has shown that a deviation up to 50% of the actual Young's modulus results in a target error of 2.5 mm. To overcome this problem, image guidance can be incorporated to provide real-time information on the shape and position of the instrument as proposed in [2] and [4].

Requirements of current clinical practice depend on the application. One of the applications could be radiofrequency ablation of liver tumors that measure up to 4 or 5 cm in diameter [22]. The authors of [23] report that a misplacement of 5 mm of the needle tip will result in insufficient ablation of the tissue. This indicates that the 1 mm accuracy that is feasible with FBG-based shape sensing may already be sufficient. However, higher accuracy may be demanded for high-precision applications such as eye or brain surgery. Moreover, future treatments may require higher accuracy to minimize damage to healthy tissue that surrounds healthy tissue.

To conclude, the current state-of-the-art of FBG-based shape sensing allows for sensor designs that can track the needle tip position with sufficient accuracy for most common needle therapies. The sensor system will need to be improved for applications in the future that require higher accuracy.

REFERENCES

[1] Henken KR, Dankelman J, Van den Dobbelsteen JJ, Cheng LK, Van der Heiden MS. *Error analysis of FBG-based shape sensors for medical needle tracking.* ASME/IEEE T Mech. Published online 2013 Nov 11; doi: 10.1109/TMECH.2013.2287764.

[2] Glozman D, Shoham M, *Image-guided robotic flexible needle steering.* IEEE T Robotic Autom. 2007; 23(3): 459-467.

[3] Kallem V, Cowan NJ, *Image guidance of flexible tip-steerable needles.* IEEE T Robotic Autom. 2009; 25(1): 191-196.

[4] Tokuda J, Fischer GS, DiMaio SP, Gobbi DG, Csoma C, Mewes PW, Fichtinger G, Tempany CM, Hata N. *Integrated navigation and control software system for MRI-guided robotic prostate interventions.* Comput Med Imag Grap. 2010; 34(1): 3-8.

[5] Xu H, Lasso A, Vikal S, Guion P, Krieger A, Kaushal A, Whitcomb LL, Fichtinger G. *MRI-guided robotic prostate biopsy: a clinical accuracy validation.* Lect Notes Comput Sc. 2010; 13: 383-391.

[6] De Oliveira A, Rauschenberg J, Beyersdorff D, Semmler W, Bock M. *Automatic passive tracking of an endorectal prostate biopsy device using phase-only cross-correlation.* Magn Reson Med. 2008; 59(5): 1043–1050.

[7] Gorlitz RA, Tokuda J, Hoge SW, Chu RX, Panych LP, Tempany C, Hata N. *Development and validation of a real-time reduced field of view imaging driven by automated needle detection for MRI-guided interventions.* In Wong KH, Miga MI, eds. Medical imaging 2010: visualization, image-guided procedures, and modeling. Bellingham: Spie-Int Soc Optical Engineering, 2010.

[8] Alt S, Homagk AK, Umathum R, Semmler W, Bock M. *Active microcoil tracking in the lungs using a semisolid rubber as signal source.* Magnet Reson Med. 2010; 64(1): 271-279.

[9] Schmidt EJ, Yoneyama R, Dumoulin CL, Darrow DR, Klein E, Kiruluta AJM, Hayase M. *3-D coronary motion tracking in swine models with MR tracking catheters.* J Magn Reson Imaging. 2007; 29(1): 86-98.

[10] Henken K, Van Gerwen D, Dankelman J, Van den dobbelsteen JJ. *Accuracy of needle position measurements using fiber Bragg gratings.* Minim Invasiv Ther, 2012; 21(6): 408-414.

[11] Park YL, Elayaperumal S, Daniel B, Ryu SC, Shin M, Savall J, Black RJ, Moslehi B, Cutkosky MR. *Real-time estimation of 3-D needle shape and deflection for MRI-guided interventions.* IEEE ASME Trans Mechatron. 2010; 15(6): 906–915.

[12] Hill KO, Meltz G. *Fiber Bragg grating technology fundamentals and overview.* J Lightwave Technol. 1997; 15(8): 1263-1276.

[13] He XC, Balicki MA, Kang JU, Gehlbach PL, Handa JT, Taylor RH, Iordachita II. *Force sensing micro-forceps with integrated fiber Bragg grating for vitreoretinal surgery.* In optical fibers and sensors for medical diagnostics and treatment applications XII, Gannot I, Bellingham: SPIE-Int Soc Optical Engineering, 2012.

[14] Iordachita I, Sun Z, Balicki M, Kang JU, Phee SJ, Handa J, Gehlbach P, Taylor R. *A sub-millimetric, 0.25 mN resolution fully integrated fiber-optic force-sensing tool for retinal microsurgery.* Int J Comput Assist Radiol Surg. 2009; 4(4): 383-390.

[15] Su H, Fischer GS. *A 3-axis optical force/torque sensor for prostate needle placement in magnetic resonance imaging environments.* IEEE Int Conf TePRA, Woburn, Massachusetts, USA, 2009.

[16] Zhang L, Qian J, Shen L, Zhang Y. *FBG sensor devices for spatial shape detection of intelligent colonoscope.* IEEE ICRA. 2004; 1: 834-840.
[17] Zhang L, Qian J, Zhang Y, Shen L. On SDM/WDM *FBG sensor net for shape detection of endoscope.* IEEE ICMA. 2005; 4: 1986-1991.
[18] Van der Heiden MS, Henken KR, Cheng LK, Van den Bosch BG, Van den Braber R, Dankelman J, Van den Dobbelsteen JJ. *Accurate and efficient fiber optical shape sensor for MRI compatible minimally invasive instruments.* Proc SPIE-Int Soc Opt Eng. 2012; 8550.
[19] Anders J, SanGiorgio P, Deligianni X, Santini F, Scheffler K, Boero G. *Integrated active tracking detector for MRI-guided interventions.* Magnet Reson Med. 2012; 67(1): 290-296.
[20] Abolhassani N, Patel R, Moallem M. *Needle insertion into soft tissue: A survey.* Med Eng Phys. 2007; 29(4): 413-431.
[21] DiMaio SP, Salcudean SE. *Needle steering and motion planning in soft tissues.* IEEE T Bio-Med Eng. 2005; 52(6): 965-974.
[22] Kunzli BM, Abitabile P, Maurer CA. *Radiofrequency ablation of liver tumors: Actual limitations and potential solutions in the future.* World J Hepatol. 2011; 3(1): 8-14.
[23] Khlebnikov R, Muehl J. *Effects of needle placement inaccuracies in hepatic radiofrequency tumor ablation.* 32nd Annual International Conference of the IEEE EMBC, Argentina, Buenos Aires, 2010.

6

Validation of FBG-based needle shape sensing through 3-D CT

Kirsten R. Henken, S.J. Camiel Klink, Adriaan Moelker, Jenny Dankelman, John J. van den Dobbelsteen

This chapter has been submitted for publication.

ABSTRACT

BACKGROUND Medical needle tracking through shape sensing based on fiber Bragg grating technology has previously been demonstrated and evaluated in 2-D. This work aims to quantify the 3-D accuracy of needle shape reconstruction and to validate its functioning using computed tomography (CT).

METHOD An 18G medical needle with three optical fibers with five FBGs each was inserted in a gelatin phantom. After insertion, the needle shape was reconstructed based on the FBG measurements and compared to its shape retrieved from CT scans.

RESULTS The error at the needle tip is maximally 1 mm and on average approximately 10% of the tip deflection. The accuracy is less for a double curved needle than for a single curved needle.

CONCLUSION Highly accurate FBG-based reconstruction of the needle shape is feasible. For clinical applicability, the technique needs to be combined with sufficiently accurate and reliable tracking techniques to measure the needle's position relative to the patient's anatomy.

6.1 INTRODUCTION

In interventional radiology, needles are commonly inserted percutaneously for diagnostic and therapeutic purposes (e.g. biopsy, ablation, and brachytherapy). Accurate placement of the needle tip contributes to a successful intervention, but is hindered by deflection of the needle. To this end, intra-procedural information about the target location and the needle tip position is required. This is most commonly achieved through CT- or ultrasound-guidance. Shape sensing based on fiber Bragg grating (FBG) technology has previously been proposed [1, 2] for needle tip tracking in order to supplement or replace the spatial information about the needle's position obtained through these imaging modalities.

An FBG behaves as an optical strain sensor with a cross-sensitivity to temperature [3]. It is a grating that is incorporated in the core of an optical fiber. When broadband light is introduced in the fiber, the FBG reflects one wavelength that corresponds to the period of the grid. This period changes when the fiber is elongated or compressed, resulting in a shift in the wavelength that is reflected by the FBG. Multiple optical fibers can safely be incorporated in a medical needle thanks to their small diameter and the absence of electrical circuits for read-out. Additionally, multiple FBGs can be included in a single optical fiber, which are read out through multiplexing [4, 5].

Shape sensing requires multiple optical fibers with multiple FBGs embedded along its length. When three fibers are radially placed 120° apart and the FBGs in the fibers are aligned longitudinally, three strains can be measured in a cross section. From these strains the elongation in axial direction and the degree and direction of bending can be determined. The needle bending can also be determined in between the FBGs by interpolating the strains and translating these to the degree and direction of bending. Summing and rotating the parameters obtained from multiple sets of FBGs along the length of the needle enables retrieval of the 3-D coordinates that correspond to the entire needle shape.

Park et al. [1] report on an MRI-compatible needle that contains three optical fibers with two FBGs each for the purpose of shape sensing, with which the tip position can be estimated with an RMS error of 0.38 mm in case of 15 mm deflection in 2-D. A medical needle with three optical fibers with two FBGs with a similar 2-D accuracy is presented in [2]. In addition to this, the current authors presented a method for calibration in [6] and optimized the model for shape sensing and investigated the added value of increasing the number of FBGs and optimizing their distribution in [7]. 3-D needle shape reconstruction for needle deflections in free space was evaluated in [8]. In the above mentioned studies, various needle shapes were obtained by applying deflections at two different locations along the needle shaft. Error measurements were based on the measurements of the needle tip position while the exact needle curvature was only estimated from theoretical approximation techniques. Therefore, the accuracy of 3-D FBG-based reconstruction of the entire needle shape has yet to be determined.

This research aims to quantify the 3-D accuracy of a shape sensing needle with five FBGs in each of the three optical fibers and to validate its functioning using CT. CT allows us to generate a 3-D image of the needle from a large series of 2-D radiographic images taken around a single axis of rotation. In the experiment, an interventional radiologist inserted the needle in a gel phantom after which the needle was scanned. In the analysis we compared the FBG-based needle shape reconstruction with the needle shape that was retrieved from the CT images.

6.2 MATERIALS AND METHODS

6.2.1 Needle

Three optical fibers (HI-780 Specialty fiber, Corning Incorporated, Corning, USA) with five FBGs each were glued in 0.3 mm grooves in the cutting stylet of a trocar needle (18G/20cm, Cook Medical, Bloomington, USA). The manufacturing process is further elaborated on in [2]. The FBGs were situated 20, 60, 100, 140, and 180 mm away from the proximal end of the needle. The positions of the FBGs within one cross section were calibrated by placing the needle in a 1.4 mm groove with a constant radius of 350 mm

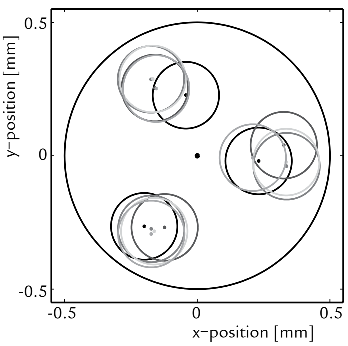

FIGURE 6.1 **The calibrated positions of the five FBG trios. The FBGs in one cross section are shown in the same color.**

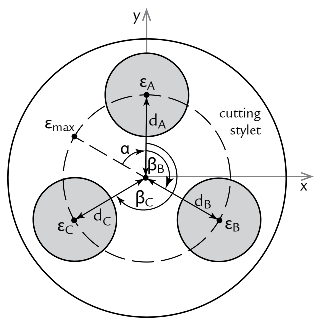

FIGURE 6.2 **Schematic view of a cross section of the needle. The degree of bending at this cross section is represented by the maximal strain (ε_{max}) at a distance d_A from the centerline, that is determined based on strains ε_A, ε_B, and ε_C in the fibers. The direction of bending (α) is determined with respect to fiber A. The positions of the fibers in this cross section are defined by the distances between their midlines and the midline of the cutting stylet (d_A, d_B, and d_C) and their orientations with respect to fiber A (β_B and β_C).**

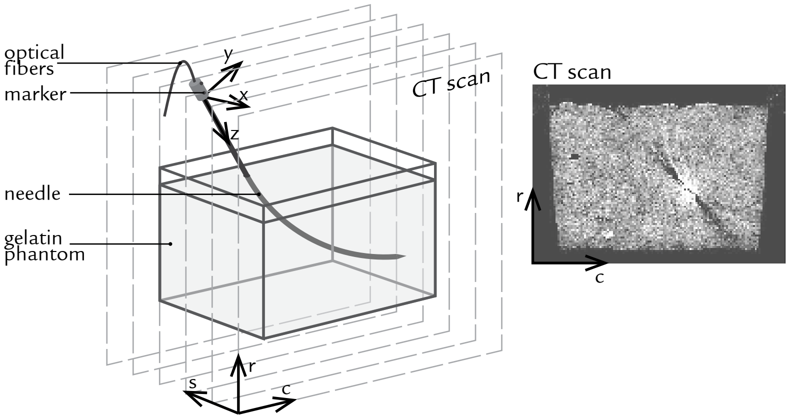

FIGURE 6.3 **Overview of the experimental set-up.**

and rotating the needle around its axis, while registering the output of the FBGs. The calibration process is further described in [6]. The calibrated positions of the five FBG trios are presented in Figure 6.1.

6.2.2 Experiment

The experiment (Figure 6.3) aimed to quantify the 3-D accuracy of FBG-based shape sensing. To this end, an interventional radiologist inserted the needle ten times in an inhomogeneous gel phantom, after which the needle shape was registered with CT (Somatom Definition Edge, Siemens). The inhomogeneous phantom was prepared in a transparent container (15x17x21 cm) and consisted of ~3 cm gelatin lumps with a concentration of 25m% in gelatin with a concentration of 5m%. The main aim of constructing a phantom with these properties was to inflict a certain amount of defection when the needle was inserted. Further, the original cannula of the needle was replaced by a cannula with a bevel tip to ensure significant deflection during insertion. Two markers (SL-15, Suremark, Simi Valley, USA) were placed on the distal end of the needle as reference in the CT. The proximal end of the needle served as the third marker.

After the needle was inserted, the FBG output was registered and a spiral CT scan was made. When the needle was removed, the output of the FBG was registered again to define the outputs of the FBGs in unstrained condition. The FBG measurements and CT scans were stored for processing afterwards.

6.2.3 Data processing

FBG-BASED NEEDLE SHAPE

The 3-D needle shape was determined based on the FBG measurements according to the model presented in [7]. The shift in the wavelength reflected by an FBG ($\Delta\lambda_B$) was determined by subtracting the mean output of each FBG in unstrained condition (λ_B) from the mean output after insertion. The strain in each FBG (ε) was calculated through

$$\varepsilon=\Delta\lambda_B/\lambda_B\,(1-P_\varepsilon) \tag{6.1}$$

where P_ε is the photo-elastic factor of the FBG. Then the strain was estimated at n positions in each of the fibers through linear interpolation based on the strain in the five FBGs.

The bending at each of the n positions along the needle was determined by relating the strains in the three fibers (ε_A, ε_B, and ε_C) to each other. Figure 6.2 provides a schematic view of the needle cross section. First the axial strain component (ε_0) was determined which includes strain due to axial stress and axial temperature changes.

$$\varepsilon_0=(A\cdot\bar{n}_\varepsilon)/\bar{n}_\varepsilon(3) \tag{6.2}$$

In this, $\bar{n}_\varepsilon$ was the normal vector of the plane through the three points $A=(0, d_A, \varepsilon_A)$, $B=(d_{Bx}, d_{By}, \varepsilon_B)$, and $C=(d_{Cx}, d_{Cy}, \varepsilon_C)$. The distances between the centerline of each FBG and the centerline of the needle or triplet were d_A, d_B, and d_C that depend on the orientations of Fiber B and C with respect to Fiber A (β_B and β_C). Radial temperature changes were disregarded, assuming that the FBGs in one cross section are subject to the same temperature change.

The degree of bending was represented by the maximal strain (ε_{max}) within the cross section of the needle. The maximal strain and the direction of bending (α) were implicitly defined by

$$\varepsilon_A=\varepsilon_{max}\cos(\alpha)+\varepsilon_0 \tag{6.3}$$

$$\varepsilon_B=d_B/d_A\,\varepsilon_{max}\cos(\beta_B+\alpha)+\varepsilon_0 \tag{6.4}$$

$$\varepsilon_C=d_C/d_A\,\varepsilon_{max}\cos(\beta_C+\alpha)+\varepsilon_0 \tag{6.5}$$

Then the strains in the fibers are compensated for the axial strain component and the differences in d_A, d_B, and d_C.

$$\varepsilon_A' = \varepsilon_A - \varepsilon_0 \tag{6.6}$$

$$\varepsilon_B' = d_A/d_B\,(\varepsilon_B - \varepsilon_0) \tag{6.7}$$

$$\varepsilon_C' = d_A/d_C\,(\varepsilon_C - \varepsilon_0) \tag{6.8}$$

After that, ε_{max} and α were determined.

$$\varepsilon_{max}^2 = (\varepsilon_A'^2 \cos\beta_B - 2\cos\beta_B\, \varepsilon_A' \varepsilon_B' + \varepsilon_B'^2)/\sin^2\beta_A \tag{6.9}$$

$$\tan\alpha = (\varepsilon_A' \cos\beta_B - \varepsilon_B')/\varepsilon_A' \sin\beta_B \tag{6.10}$$

To avoid large errors when the needle was almost straight, ε_{max} was set to zero in case ε_{max} was smaller than a threshold in accordance with the resolution of the interrogator (6 pm). The shape of the needle ($\bar{x}_{FBG}$) was reconstructed by summing and rotating the 3-D displacements (d_x, d_y and d_z) of each needle section in between the n points. L is the length of the needle.

$$d_x = L/n \sin(\alpha)\ \sin(\varepsilon_{max}(L/n)/2d_A) \tag{6.11}$$

$$d_y = L/n \cos(\alpha) \sin(\varepsilon_{max}(L/n)/2d_A) \tag{6.12}$$

$$d_z = L/n \cos(\varepsilon_{max}(L/n)/2d_A) \tag{6.13}$$

CT-BASED NEEDLE SHAPE

MeVisLab (Version 2.2.1, MeVis Medical Solutions AG, Bremen, Germany) was used to retrieve the 3-D needle shape from the CT images. Multiple (220-465) points on the needle were selected through clicking and were then exported as 3-D coordinates in the coordinate system of the CT scanner. The positions of the three markers were retrieved from the CT images in the same way. Three third-order polynomials were fitted between a reference vector and each of the three dimensions of the needle shape. The reference vector consisted of the distance between each point on the needle and the proximal end. The three polynomials were evaluated for n points equally spaced along the needle to obtain the 3-D CT-based needle shape ($\bar{x}_{CT}$). This process was executed for each of the ten measurements.

Procrustes analysis in MATLAB (R2011b, Mathworks, Natick, USA) was used to match the FBG-based needle shape with the CT-based needle shape. First, the degree of needle deflection based on the FBGs was evaluated by retrieving the optimal fit between the individual needle shapes based on the FBG measurements ($\bar{x}_{FBG}$) and CT images ($\bar{x}_{CT}$). Secondly, the orientation of the FBG-based needle shape was evaluated by taking the positions of the markers in account. Therefore, the individual fit of reference measurement #10 was used to relate the coordinate system of the FBGs to the CT-coordinate system of the markers. In the remaining measurements, the orientation of the needle with respect to the reference measurement was determined by matching the marker positions in the particular measurement with the marker positions in measurement #10. After this, the coordinates of the CT-based needle shape were translated and rotated to obtain the CT-based needle shape in the FBG coordinate system.

The FBG-based needle shapes were compared to the CT-based needle shapes by calculating the difference or distance between the two shapes, in which the CT shape served as the golden standard. Two errors were computed: the error at the tip of the needle and the mean error along the length of the needle.

6.3 RESULTS

Figure 6.4 shows a 2-D projection of each of the 3-D FBG-based and CT-based needle shapes. The CT-based needle shapes are individually matched with the FBG-based needle shapes. The tip deflection according to the FBG-based needle shape and the tip

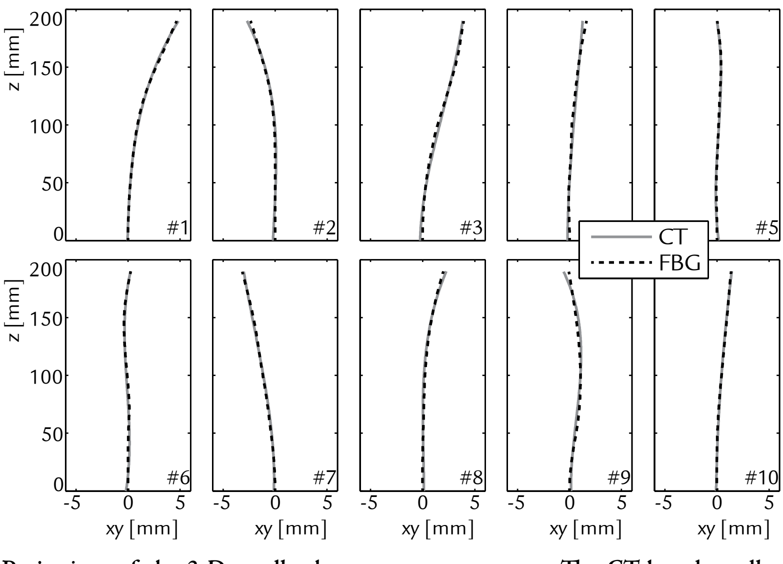

FIGURE 6.4 **Projections of the 3-D needle shapes per measurement. The CT-based needle shapes are individually matched with the FBG-based needle shapes.**

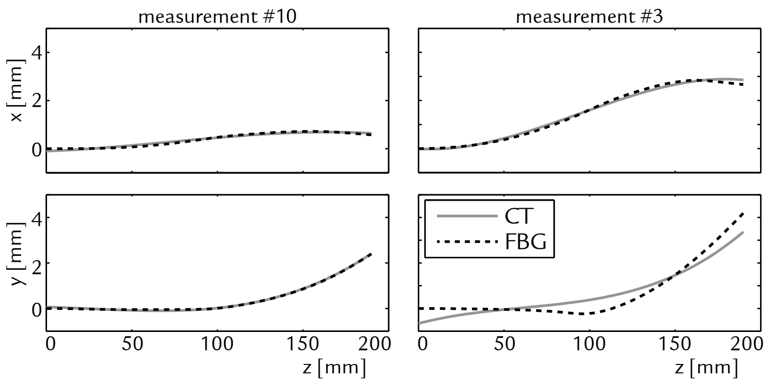

FIGURE 6.5 **Two orthogonal projections of the needle shapes in measurement #3 and #10. The CT-based needle shapes are individually matched with the FBG-based needle shapes.**

and mean error of the needle shapes are presented in Table 6.1. The mean tip error is 0.48 mm for a mean tip deflection of 4.43 mm. The mean error along the length of the needle is 0.18 mm. The smallest tip error is 0.07 mm for measurement #10, with a mean error along the length of 0.05 mm The largest tip error is 0.88 mm for measurement #3 with a mean error along the length of 0.37 mm. Two orthogonal projections of the needle shapes in measurement #3 and #10 are provided in Figure 6.5. The needle has a single curve in measurement #10, which is accurately reconstructed based on the FBG output. The needle is doubly curved in measurement #3 and the FBG-based needle shape does not correspond well to the CT-based needle shape.

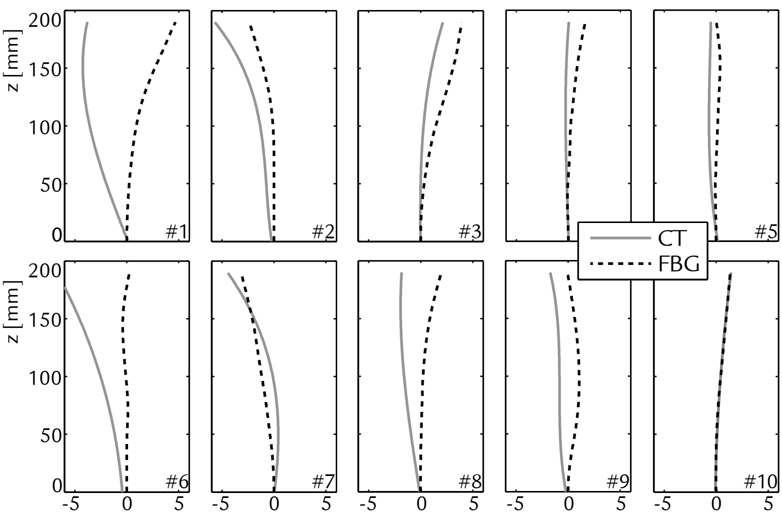

FIGURE 6.6 **Projections of the 3-D needle shapes per measurement. The CT-based needle shapes are matched with the FBG-based needle shapes based on measurement #10 and the marker positions.**

TABLE 6.1 Errors [mm] in the FBG-based shape reconstruction. The tip deflection [mm] is determined according to the FBG-based needle shape. The tip error is the distance between the FBG-based and the CT-based needle shape. The mean error is the mean distance between the FBG-based and the CT-based needle shape along the length of the needle. Both errors are determined for both matching methods.

#	1	2	3	4	5	6	7	8	9	10
Deflection at tip	6.27	2.71	5.21	2.30	3.69	2.61	7.97	2.20	8.62	2.71
Individually optimized fit										
Error at tip	0.18	0.50	0.88	0.71	0.23	0.48	0.58	0.51	0.68	0.07
Mean error	0.09	0.13	0.37	0.41	0.13	0.17	0.11	0.13	0.18	0.05
Fit based on #10 and markers										
Error at tip	8.62	3.39	1.88	1.97	0.35	7.99	1.42	6.41	1.70	0.07
Mean error	4.26	1.73	1.65	1.54	0.55	3.29	0.78	2.86	1.48	0.05

Figure 6.6 presents the same 2-D projection of the two 3-D needle shapes as presented in Figure 6.5. In this series, the CT-based needle shapes are matched with the FBG-based needle shapes based on the fit of reference measurement #10 and the fit of the marker positions. The corresponding tip errors and mean errors are provided in Table 6.1. Here, the mean tip error is 3.38 mm for a mean tip deflection of 4.43 mm. The tip errors range from 0.35 mm in measurement #5 to 8.62 mm in measurement #1. This is a combined result of errors in the FBG measurements and in (the fit of) the marker positions. Errors in the FBG measurements cause inaccurate reconstruction of the needle shape. Errors in (the fit of) the marker positions introduce a misalignment of the CT-based needle shape with the FBG-based needle shape, which hampers a realistic comparison between the two needle shapes. For example, the tip error in measurement #1 is 0.18 mm for the individual fit and 8.62 mm for the fit based on measurement #10 and the marker positions. Visualization of measurement #1 in Figure 6.6 shows the misalignment of the CT-based needle shape introduced by the errors in the marker positions.

6.4 DISCUSSION

The aim of this research was to quantify the 3-D accuracy of FBG-based shape sensing of medical needles in order to evaluate its suitability for providing intra-operative feedback about the needle's tip position in percutaneous needle interventions. Therefore, a medical needle with markers on the handle was equipped with three optical fibers with five FBGs each. The needle was inserted in an inhomogeneous gel phantom after which the FBG outputs were measured and a CT scan was made. Afterwards, the needle shape was reconstructed based on the FBG outputs. This shape was compared to the needle shape retrieved from the CT images.

Optimizing the fit between the FBG-based needle shape and the CT-based needle shape per individual measurement indicates that it is possible to accurately reconstruct the needle shape based on FBG measurements. After matching the two needle shapes, the tip error is maximally 1 mm and on average approximately 10% of the tip deflection. Some of the FBG-based and the CT-based needle shapes are misaligned, when matching is obtained via a reference measurement and the marker positions at the handle are retrieved from the CT images. This disturbs the comparison between the two needle shapes and the quantification of the accuracy of the FBG-based shape reconstruction.

The accuracy of the FBG-based reconstruction of the needle shape is less for a double curved needle than for a single curved needle, which is in line with the results in [2, 8]. The curvature of the needle is estimated based on a limited number of FBGs, since pre-procedural information about the exact loading profile is not available. When a double curve is present, the actual strain distribution along the needle is more complex, but still has to be retrieved from the same number of FBGs. In addition, the strain measured in the FBGs is not strictly local and is affected by the strain along the complete needle due to strain losses and strain distribution in the glue. This effect becomes more visible in double curved shapes, because the strains in the two curves cancel each other out by the strain distribution.

The high accuracy of the individual fits suggests that the errors in the FBG measurements do not affect the degree of bending substantially. However, the results of the second matching method suggest that these errors may affect the orientation of the needle deflection. This effect could not be quantified accurately based on the current data due to the limited accuracy of (the fit of) the marker positions. Errors in the marker positions may be small due to the high resolution of the CT images, but even these small errors add up to large errors in the estimation of the handle's orientation relative to the needle shaft as the markers are only a few millimeters apart.

The 1 mm accuracy found in this study is in line with previous findings [1, 2]. Such accuracy is presumably sufficient for application in percutaneous needle interventions. However, the current study shows that the accuracy that can be obtained in practice will be less due to the effect of errors in the FBG measurements on the reconstructed needle shape. Further, a highly accurate reference method is required to relate the coordinate system of the FBGs to the real world, to be able to estimate the needle tip position relative to the patients organs within the clinically accepted margins. Dedicated systems for instrument tracking are readily available in clinical practice for stereotaxy [9]. Alternatively, other real-time imaging techniques such as ultrasound could be used for global localization of the needle's position while the exact shape is reconstructed using FBGs.

6.5 CONCLUSION

We conclude that highly accurate FBG-based reconstruction of the needle shape is possible. For clinical applicability, the technique needs to be combined with sufficiently accurate and reliable tracking techniques to measure the needle's position relative to the patient's anatomy.

ACKNOWLEDGEMENT

We thank Marcel Dijkshoorn and Theo van Walsum for their support in obtaining and analyzing the CT images.

REFERENCES

[1] Park YL, Elayaperumal S, Daniel B, Ryu SC, Shin M, Savall J, Black RJ, Moslehi B, Cutkosky MR. *Real-time estimation of 3D needle shape and deflection for MRI-guided interventions*. IEEE ASME Trans Mechatron. 2010; 15(6): 906–915.

[2] Henken K, Van Gerwen D, Dankelman J, Van den dobbelsteen JJ. *Accuracy of needle position measurements using fiber Bragg gratings*. Minim Invasiv Ther, 2012; 21(6): 408-414.

[3] Hill KO, Meltz G. *Fiber Bragg grating technology fundamentals and overview*. J Lightwave Technol. 1997; 15(8): 1263-1276.

[4] Rao YJ. *In-fibre Bragg grating sensors*. Meas Sci Technol. 1997; 8(4): 355-375.

[5] Childs P, Wong ACL, Yan BB, Li M, Peng GD. *A review of spectrally coded multiplexing techniques for fibre grating sensor systems*. Meas Sci Technol. 2010; 21: 094007.

[6] Van der Heiden MS, Henken KR, Cheng LK, Van den Bosch BG, Van den Braber R, Dankelman J, Van den Dobbelsteen JJ. *Accurate and efficient fiber optical shape sensor for MRI compatible minimally invasive instruments*. Proc SPIE-Int Soc Opt Eng. 2012; 8550.

[7] Henken KR, Dankelman J, Van den Dobbelsteen JJ, Cheng LK, Van der Heiden MS. *Error analysis of FBG-based shape sensors for medical needle tracking*. ASME/IEEE T Mech. Published online 2013 Nov 11; doi: 10.1109/TMECH.2013.2287764.

[8] Roesthuis RJ, Kemp M, Van den Dobbelsteen JJ, Misra S. *Three-dimensional needle shape reconstruction using an array of fiber bragg grating sensors*. ASME/IEEE T Mech. Published online 2013 Jul 12; doi: 10.1109/TMECH.2013.2269836.

[9] Eggers G, Muhling J, Marmulla R. I*mage-to-patient registration techniques in head surgery*. Int J Oral Max Surg. 2006; 35(12): 1081-1095

7

FBG-based force sensing at the tip of a needle

Kirsten R. Henken, Mart C. Gahler, Jenny Dankelman,
John J. van den Dobbelsteen

This chapter has been submitted for publication.

ABSTRACT

BACKGROUND Needles are commonly used in clinical practice to take a biopsy or to deliver substances, while limiting damage to the healthy surrounding tissue. A force sensor at the tip of the needle allows for the registration of the interaction between needle and tissue and may assist in navigation. This study reports on the development of a needle with a force sensor in the tip based on fiber Bragg grating (FBG) technology.

METHOD The relation between the output of the FBG and the tip force was characterized at various temperatures. In addition, the needle was evaluated in vivo by inserting it in the liver of a porcine.

RESULTS The relation between the output of the FBG and the tip force was characterized at various temperatures. In addition, the needle was evaluated in vivo by inserting it in the liver of a porcine.

CONCLUSION Detection of force peaks with an FBG in the tip of a needle is feasible. Solutions for compensation of the effect of temperature include adding an FBG.

7.1 INTRODUCTION

Needles are commonly used in various clinical applications, which include biopsy, ablation, brachytherapy and many more. Accurate placement of the needle is essential to ensure a successful outcome of the procedure. Guidance is usually accomplished by means of imaging techniques such as ultrasound or CT. However, other information sources may contribute to accurate placement of the needle tip as well. One of these sources is the force that acts on the needle during insertion. Registering peak forces at the tip allows for the identification of different tissue layers, which may assist the physician to navigate to the target. For example, a sudden drop in force could inform the physician whether the needle has actually punctured a specific membrane or target organ, or has only pushed it away. In addition, force sensing at the needle tip can possibly be applied to distinguish between healthy and diseased tissue and help to ensure that the intervention (e.g. biopsy) is performed at the right location. However, limited opportunities are currently available to accurately quantify the force that acts on the needle tip. This research aims at the development of a needle that measures the axial forces at the tip during insertion.

Limited data are currently available on the forces that are present during needle insertion. Van Gerwen et al. [1] summarized literature that reports on experimentally determined needle-tissue interaction forces. The range of reported forces is wide due to large variation in the experimental methods, while the forces itself highly depend on the insertion velocity, needle properties, and tissue type that has been punctured. The forces are typically measured at the handle of the needle which provides information about the total axial insertion force, which is the sum of the friction force along the needle shaft ($F_{friction}$), the force that is exerted by the stiffness of the tissue on the needle tip ($F_{stiffness}$), and the force that is required to cut through the tissue ($F_{cutting}$) [2]. It is difficult to delineate the contribution of these individual components when only the total insertion force is measured. In an experimental setting partial solutions can be applied to estimate the magnitude of a single component. For instance, the friction force can be determined indirectly by measuring the total force at the handle during removal of the needle, because the other two components both equal zero in case the needle is withdrawn [3]. Another option to measure $F_{friction}$ separately is to move the needle through tissue while the tip is sticking out on the other side [2, 4, 5]. The forces that act only on the tip ($F_{stiffness}$ and $F_{cutting}$) can be determined indirectly by subtracting $F_{friction}$ from the total insertion force. These methods are not feasible though during real interventions.

The needle presented here measures forces at the tip ($F_{stiffness}$ and $F_{cutting}$) separately from the friction along the shaft through a glass fiber that is integrated in the needle. A fiber Bragg grating (FBG) is embedded in the core of the fiber that operates as a strain sensor by reflecting light with a wavelength that corresponds to the strain [6]. The small diameter of the fiber and the sensor allows for the incorporation in a thin device like a needle. Besides this, FBGs induce no risk for the patient as they contain no conductive materials and only require an optical signal. The use of fibers with FBGs for strain sensing on needles has been proposed in several previous studies. For instance, when three of such fibers are implemented, it is possible to measure bending of the needle for the purpose of shape sensing or to measure lateral forces [7-9]. Elayaperumal et al. [10] have combined shape sensing and axial tip force sensing. This force sensor is well able to distinguish friction forces from tip forces, but the open structure of the needle may not be eligible for use in clinical practice. Ho et al. [11] report on the integration of a single FBG in the tip of an ablation catheter aiming at a qualitative interpretation of the FBG output to avoid puncturing of the heart. In the current study, the goal is not only to develop a device that could identify such an event but also to accurately quantify the interaction forces with a needle that is appropriate for use in clinical practice.

This paper discusses the design of a needle with a single FBG in the tip for the purpose of measuring axial tip forces. It also reports on the identification of the relation between the tip force and the FBG output. Since FBGs are sensitive to variations in temperature and the temperature of the needle changes during insertion (i.e. from room temperature to body temperature), measurements are repeated at different temperatures. In addition, pilot experiments suggested that the FBG output may be influenced by the magnitude of the force that acts on the tip and by the rate at which it is applied, therefore these effects are investigated as well. Finally, the needle is validated in an in vivo experiment in a porcine model.

7.2 METHOD

7.2.1 Design of the needle

The design of the force sensing tip of the needle was guided by three main requirements:

I. It should be possible to integrate the sensor in existing needles that are currently available for medical purposes. For this study, we choose to use an 18 G/20 cm trocar needle of Cook Medical that is regularly used in nephrostomy, in which a catheter is placed in the kidney to directly drain urine;
II. The sensor should be able to measure the axial forces directly at the tip to eliminate the contribution of friction to the measured force. The measurement range of the sensor should be between 0 and 15 N with an accuracy of 0.01 N, based on forces that are previously reported to occur during needle insertion in the kidney [1];
III. The needle with the force sensing tip is required to be medically safe, biocompatible and sterilizable to allow for use of the needle in clinical practice.

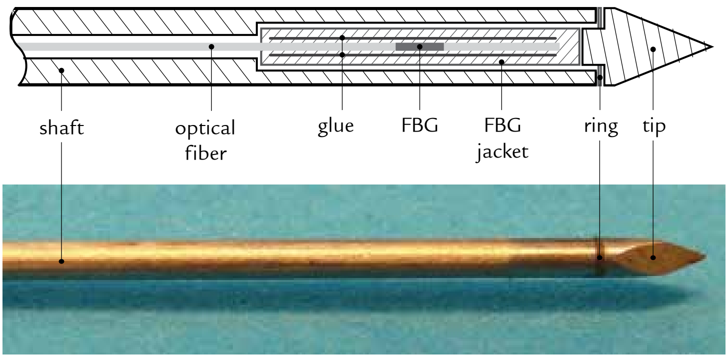

FIGURE 7.1 Design of the cutting stylet of the force sensing needle. The strain sensing FBG is fixated in a PVC jacket that is compressed in between the tip and the shaft when an axial force acts on the tip.

The trocar needle consists of the original outer sheath and a cutting stylet. The cutting stylet (Figure 7.1) is modified to integrate the fiber (Hi 780 specialty fiber, Corning, USA) with the FBG (central wavelength of 856 nm±0.5 nm) with the needle in such a way that the forces exerted on the tip result in strain of the optical fiber that is measurable by the FBG. Therefore, the FBG is situated in a 200 μm groove with a depth of 430 μm in a cylindrical PVC jacket (0.7 mm OD) that is positioned in a cavity in the shaft. The FBG is fixated with a bonding (Loctite 4061, Henkel, Germany) and the remaining space in the groove is filled up with a second bonding (Loctite 4031, Henkel, Germany). The cavity that holds the jacket is created by replacing the cutting stylet by two concentric tubes (1.0/0.7 mm and 0.7/0.35 mm OD/ID, respectively), of which the inner tube is 8.4 mm shorter. The tip is placed directly adjacent to the jacket, but a PVC ring is placed in between the shaft and the tip to transfer the movement of the tip with respect to the shaft to the jacket and the FBG, without leaving an open space in between where tissue could accumulate.

When the needle is inserted, the force acting on the tip is transferred to the FBG. Only forces in axial direction are transferred, because rotation and lateral translation of the FBG jacket is constrained by the shaft. The axial force (F) pushes the needle inward and compresses the jacket and the FBG, which will result in a strain (ε).

$$\varepsilon = F \,/\, AE \tag{7.1}$$

A is the cross sectional area of the jacket including the optical fiber and the ring. E is the Young's modulus of the PVC jacket, the fiber, and the PVC ring. Assuming that the Young's modulus equals the one of PVC (~3.3 GPa), a force of 0.01 N results in 7.9 $\mu\varepsilon$, which is higher than the resolution of the read-out of the FBG (~3 $\mu\varepsilon$). The strain results in a change in the wavelength that is reflected by the FBG ($\Delta\lambda_B$), which is theoretically presented by

$$\Delta\lambda_B/\lambda_B = (1\text{-}P_\varepsilon)\ \varepsilon + (\alpha_T+\xi)\ \Delta T \qquad (7.2)$$

in which P_ε is the photo-elastic factor. A shift in the wavelength can also be introduced by a change in temperature (Δ_T), of which the relation is determined by the thermo-expansion coefficient (α_T) and thermo-optic coefficient (ξ) of the FBG. λ_B is the Bragg wavelength, that is determined by the grating period Λ and the effective refractive index n_{eff} is in an unstrained FBG.

$$\lambda_B = 2n_{eff}\Lambda \qquad (7.3)$$

According to Rao [12], FBGs that operate around 830 nm have a sensitivity to strain and temperature of approximately 0.64 pm/με and 6.8 pm/°C, respectively. If the measurements are performed at a known, constant temperature, $\Delta\lambda_B$ relates purely to the axial force that acts on the tip.

7.2.2 In vitro experiments

Because both mechanical and thermal factors introduce a change in the wavelength that is reflected by the FBG, the relation between the axial force that acts on the tip and the FBG output was determined for two different temperatures and three different loading profiles in randomized order (Table 7.1). The FBG signal, the exerted force and the strain were registered and the slope that relates the FBG output to the exerted force was determined for each temperature.

The needle was attached to a load cell of a universal testing machine (Zwick Roell Allround-line Z005, Zwick Roell) in vertical position and clamped about 15 mm above the tip (Figure 7.2). Then the needle was moved down with a constant velocity (v) first until the needle tip touched the ground plate and then until the end force (F_{end}) was reached (loading stage). After that, the force was kept constant during 60 s (constant phase). Finally, the needle was moved upwards with the same velocity until the force measured by the load cell equaled zero again (unloading phase). The displacement of the universal tester and the force measured with the load cell were concurrently registered on a desktop and the output of the FBG was measured with an interrogator (Deminsys, Technobis, Uitgeest, the Netherlands) at a frequency of 100 Hz. The output of the FBG was provided in pixel value, which linearly relates to the peak wavelength it reflects. When the temperature was 38°C, the measurements were executed inside a temperature chamber (BW91250, Zwick Roell). The other measurements were carried out while the needle was placed in a beaker filled with water. The temperature of the water was monitored manually with a thermo couple and, when necessary, adjusted by adding cold water in between measurements.

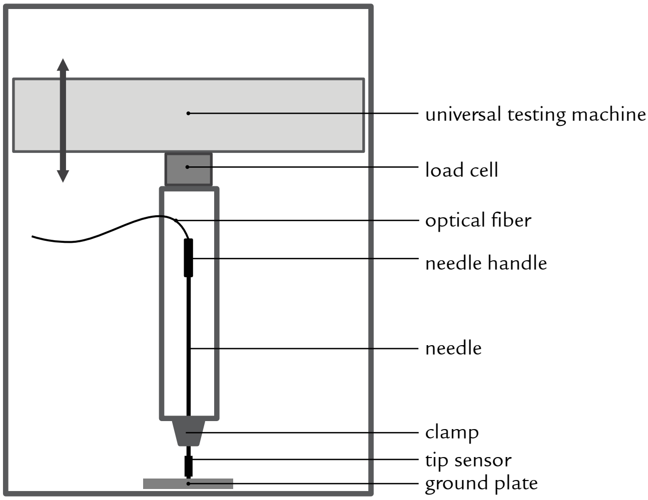

FIGURE 7.2 **Schematic view of the calibration set-up. The needle is clamped and attached to the load cell of the universal testing machine. In the calibration cycle, the needle is moved down with a constant velocity until the end force is reached. Then the end force is held for 60 s, after which the needle is moved up with the same constant velocity. The displacement of the testing machine, the forces measured with the load cell and the output of the FBG are registered concurrently.**

7.2.3 In vivo evaluation

The performance of the sensorized needle was evaluated in an in vivo experiment in which the needle was manually inserted in the liver of a living porcine. As shown in Figure 7.3, the handle of the needle was connected to a 6 DOF force/torque sensor (Nano 17 SI-12-0.12, ATI Industrial Automation, USA). This assembly was covered with an outer shell to make sure that all forces were transferred to the force sensor and to provide an easy grip to the physician.

As the calibration experiments showed high sensitivity to variations in temperature an additional calibration was carried out before the actual measurements were started. The needle was placed in a beaker filled with water of 38°C, which equals the body temperature of the porcine. The needle was held in a vertical position and manually pressed against the bottom of the beaker multiple times, while the output of the force sensor and the FBG was measured. One single calibration factor that linearly relates the FBG output to the tip force (the slope) was extracted from this calibration.

The porcine was a Norwegian land-race pig weighing 50 kg. It was treated according to the Guide for the Care and Use of Laboratory Animals. The study was approved by the Norwegian Experimental Animal Board in agreement with the Helsinki convention for the use and care of animals. The pig was intubated through a tracheostomy, fully anesthetized, mechanically ventilated during the length of the experiment, and after the experiments euthanized without waking up.

TABLE 7.1 Settings of all calibration cycles and the results -mean (standard deviation)- for the loading phase.

#	T	v	F_{end}	ΔF	Δz	ΔPV	dF/dPV	Mean fit error	Max fit error
	°C	μm/s	N	N	μm	-	N	N	N
6	20.5	85	10	9.98 (0.02)	95.1 (5.63)	0.278 (0.00)	36.9 (0.98)	0.169	0.667
5	20.5	17	2	2.01 (0.02)	77.0 (19.4)	0.055 (0.00)	39.0 (3.38)	0.039	0.114
6	20.5	17	10	9.97 (0.01)	84.9 (3.20)	0.270 (0.01)	33.1 (0.62)	0.179	0.439
6	38.0	85	10	10.0 (0.04)	81.1 (2.56)	0.485 (0.02)	20.8 (0.98)	0.268	0.690
6	38.0	17	2	2.12 (0.03)	64.4 (5.53)	0.068 (0.00)	32.4 (0.63)	0.044	0.239
6	38.0	17	10	10.0 (0.01)	75.9 (1.24)	0.511 (0.01)	16.7 (0.24)	0.295	0.927

T = temperature
v = insertion velocity
F_{end} = final force
ΔF = measured force difference
Δz = measured displacement of the universal tester
ΔPV = change in pixel value measured by the interrogator
dF/dPV = slope that relates pixel value to the force; mean and maximal error of the linear fit

An experienced physician first made a cut in the skin. The choice of the location and appropriate approach angle for inserting the needle was based on pre-operatively obtained X-ray images. After that, he inserted the needle manually through all intervening tissue layers into the liver. This was repeated ten times starting at different points of insertion. During the insertions, the forces and the output of the FBG were measured synchronously at a sample frequency of 100 Hz.

Afterwards, the outputs of the FBG were translated to tip forces through multiplication by the slope obtained from the measurements in the beaker. The tip forces were compared to the total insertion forces measured at the handle to investigate how the sensor had functioned in the in vivo experiment.

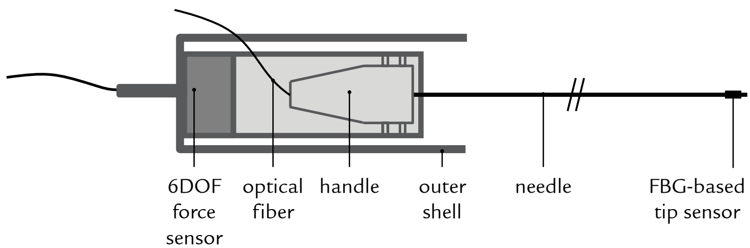

FIGURE 7.3 Schematic view of the needle handle during the manual insertions in the living porcine. A 6 DOF force sensor is attached to the needle and the whole is covered by an outer shell to allow for complete transfer of forces to the force sensor and to provide a convenient hand grip to the physician.

7.3 RESULTS

7.3.1 In vitro experiments

Figure 7.4 shows the relation between the change in FBG output and the force measured by the load cell of the testing machine of all measurements. One of the measurements (T=20.5°C, 17 μm/s and 2 N) was disregarded, because significant control issues of the testing machine were observed. The relation between the output of the FBG and the force is not strictly linear and hysteresis and relaxation occur. Different responses of the FBG are observed for different temperatures, loading rates and forces.

The actual difference in force, the displacement that is applied to reach the end force and the corresponding change in the FBG output are registered. The mean and standard deviation of these parameters per setting are summarized in Table 7.1 for the loading phase. The displacement and the change in FBG output were both scaled to match an end force of exactly 2 or 10 N. Table 7.1 also presents the slope of the loading phase of the FBG-force curve that was determined by means of a linear fit that was determined by minimizing the summed squared error as well as the corresponding mean and maximal error of the linear fit. The overall mean error of the fit was 0.17 N which gives an indication of the accuracy of the tip sensor.

Zooming in on the effect of temperature, the slope is smaller for the loading cycles at 38.0°C than those at 20.5°C irrespective of the other settings. This is partly caused by the larger output of the FBG for the higher temperature, which was expected based on the cross sensitivity of the FBG to temperature. However, the smaller displacement that is required to reach the end force also contributes to the difference in slope. This

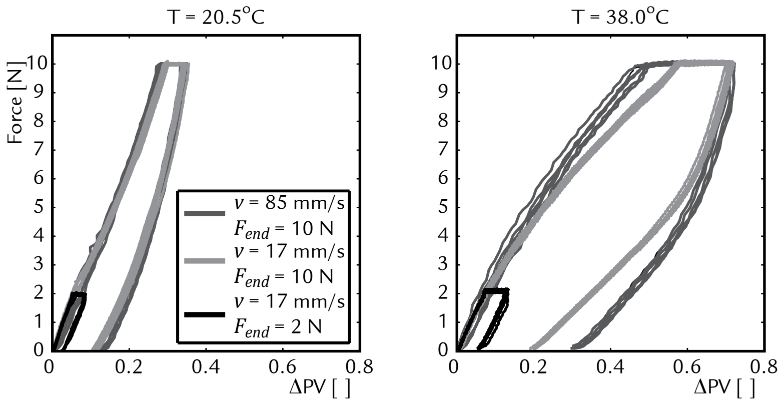

FIGURE 7.4 **The relation between the change in pixel value (ΔpV) of the FBG and the force for each measurement. Different responses are observed for different settings. Linearity is compromized by the friction between the needle and the jacket and hysteresis and relaxation occurs.**

indicates that the sensor is less compliant at higher temperatures, while normally the stiffness of materials (jacket and bonding) decreases when the temperature increases. Friction between the jacket and the shaft that increases as the jacket thermally expands may contribute to this.

7.3.2 In vivo measurements

Figure 7.5 shows the total axial force measured with the external force sensor and the force measured with the FBG at the tip. The tip force was calculated by multiplying the output of the FBG with the slope (17.1 N) that was determined based on the calibration measurements that were carried out just before the insertions. The peaks in the tip force coincide with the peaks in the total axial insertion force. However, it appears that the magnitude of the tip force is not representative due to warming of the needle to the body temperature of the pig. Consequently, approximately the first five seconds are influenced by a change in temperature. This effect is also observed when the needle is removed from the porcine again, where the force acting on the needle tip is zero and the FBG output is still changing because the temperature is decreasing to room temperature.

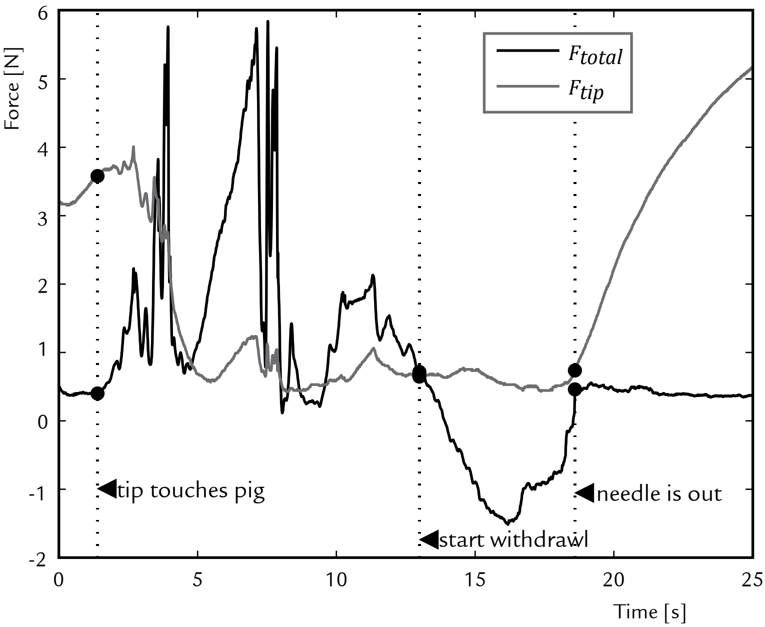

FIGURE 7.5 **Total force measured at the handle (F_{total}) and tip force measured with the FBG at the tip (F_{tip}) during one of the insertions in a porcine liver. The change from room temperature to the body temperature of the porcine affects the force measurement at the tip. The tip sensor is well able to register peak forces.**

When looking at the forces measured with the external force sensor, the maximum peak force during the different insertions range between 4.4 and 7.0 N. The maximum friction force (measured during withdrawal of the needle) is in between 1.0 and 2.2 N.

7.4 DISCUSSION

A needle with a force sensor at the tip was developed to measure forces that act on the tip separately from the friction force along the shaft. In the design, an optical fiber that was equipped with a strain sensor based on FBG-technology was successfully integrated in an existing needle. The FBG was assembled in such a way that, apart from temperature changes, only axial forces acting on the needle tip were affecting the output. These forces caused strain in the PVC jacket that could be measured by the FBG and the interrogator. The exterior of the needle remained almost the same compared to the original medical needle.

The results of the calibration show that the relation between the FBG output and the force that acts on the tip is not strictly linear and that hysteresis and relaxation occurs. In addition, the FBG output is affected by the temperature, insertion velocity and the magnitude of the exerted force, which cannot always be controlled well during needle insertion. This variability is partly introduced by the supporting structure around the FBG, for example through thermal expansion of the jacket or through variations in strain transfer by the bonding. These factors could be eliminated by measuring the strain directly with the FBG, but this is not practicable because of the fragility of the glass fiber. Therefore, calibration of FBG-based force sensors is inevitable to obtain sufficient accuracy.

Additionally, the FBG is influenced by the temperature. As shown in (7.2), a change in temperature introduces expansion of the FBG as well as a change in its optical properties, both of which affect the reflected wavelength in a direct manner. In addition to this, the temperature influences the FBG output indirectly via expansion of the jacket and changes in mechanical properties of the glue and the PVC. Other factors besides the temperature seem to play a role as well. Friction between the jacket and the shaft and other unknown interactions within the construction that supports the FBG were illustrated to be present by the higher apparent stiffness due to thermal expansion at higher temperatures. Therefore, it was not possible to relate the FBG output to the exerted force with the accuracy that was theoretically expected on the basis of the sensitivity for strain of the FBG and the sensitivity of the interrogator. However, the in vivo experiments show that that the current sensor is able to register force peaks during insertion in tissue, which suggests that accurate measurements of the tip forces using FBGs are feasible after improving the sensor design.

One improvement is to add an extra FBG for temperature compensation, so that extensive calibration is no longer needed and a higher accuracy can be obtained. Three configurations are available for temperature compensation. In the first configuration, two FBGs are placed in one fiber of which one is glued to the jacket and the other is not. This design is very similar to the current design and does not introduce any difficulties in production. However, the FBG for temperature compensation may not be located sufficiently close to the force sensing FBG, so that the temperature compensation is delayed with respect to the force measurement during needle insertion. In the second configuration, two fibers with one FBG each are incorporated in the jacket. Again only one FBG is glued to the jacket to measure the force and the other FBG serves for temperature compensation. This configuration allows for more precise temperature compensation, although still a temperature difference in lateral direction might deteriorate the results. In addition, the production of such a configuration will be challenging due the limited spaced that is available in the jacket. A third option is to use a more sophisticated FBG that is able to measure temperature changes and mechanical strain at the same time. An example is a partly covered FBG [13, 14] that responds differently to a force acting on the FBG than to a change in temperature. These FBGs will be more expensive and the read-out will be more complicated.

Despite the limitations of the currently developed needle, our study shows that accurate sensing of axial forces at the tip based on FBG technology is feasible. These results are in line with Elayaperumal et al. [10]. In addition, we show that it is possible to incorporate force sensing without altering the exterior of the needle thereby ensuring proper functioning with the current approach. This confirms that it is possible to accurately quantify the interaction forces with a needle that is appropriate for use in clinical practice.

It is generally assumed that providing feedback about forces assists physicians to accurately navigate the needle to the target. For example, peak forces that occur when various tissue types are punctured could provide information about the exact location of the needle tip. However masking of the forces by the friction between the needle and the tissue may complicates this. Further, the interaction mechanics in manual insertion are not only influenced by the type and condition of the tissue that is penetrated, but also by the rate at which the needle is introduced and the sharpness of the tip for example. In addition, it is yet unknown in what fashion force feedback should be provided to physicians to actually contribute to precise navigation. To gain more insight in these matters, experimental data about the tip forces are essential. Experimental data about the forces that occur at the tip are also valuable in characterization of the mechanical properties of different tissue types. Force sensing needles like the one that is presented here may support the development of models that describe needle-tissue interaction or in optimization of needle designs, thereby contributing to the improvement of the safety and effectiveness of minimally invasive interventions.

ACKNOWLEDGEMENT

The porcine was treated according to the Guide for the Care and Use of Laboratory Animals. The study was approved by the Norwegian Experimental Animal Board in agreement with the Helsinki convention for the use and care of animals. We would like to thank Thomas Langø and Tore Amundsen from "The Future OR" at St. Olavs Hospital in Trondheim, Norway, who provided the infrastructure for the validation experiment.

REFERENCES

[1] Van Gerwen DJ, Dankelman J, Van den Dobbelsteen JJ, *Needle–tissue interaction forces–A survey of experimental data*. Med Eng Phys. 2012; 34(6); 665-680.
[2] Okamura AM, Simone C, O'Leary MD. *Force modeling for needle insertion into soft tissue*. IEEE T Bio-med Eng. 2004; 51(10): 1707-1716.
[3] Hing JT, Brooks AD, Desai JP. *A biplanar fluoroscopic approach for the measurement, modeling, and simulation of needle and soft-tissue interaction*. Med Image Anal. 2007; 11(1): 62-78.
[4] Kobayashi Y, Sato T, Fujie MG. *Modeling of friction force based on relative velocity between liver tissue and needle for needle insertion simulation*. Annual Inernational Conference of the IEEE EMBC. USA, Minneapolis, 2009.
[5] Abolhassani N, Patel R, Moallem M. *Experimental study of robotic needle insertion in soft tissue*. Int J Comput Assist Radiol Surg. 2004; 1268: 797-802.
[6] Hill KO, Meltz G. *Fiber Bragg grating technology fundamentals and overview*. J Lightwave Technol. 1997; 15(8): 1263-1276.
[7] Henken K, Van Gerwen D, Dankelman J, Van den dobbelsteen JJ. *Accuracy of needle position measurements using fiber Bragg gratings*. Minim Invasiv Ther, 2012; 21(6): 408-414.
[8] Park YL, Elayaperumal S, Daniel B, Ryu SC, Shin M, Savall J, Black RJ, Moslehi B, Cutkosky MR. *Real-time estimation of 3-D needle shape and deflection for MRI-guided interventions*. IEEE ASME Trans Mechatron. 2010; 15(6): 906–915.
[9] Iordachita I, Sun Z, Balicki M, Kang JU, Phee SJ, Handa J, Gehlbach P, Taylor R. *A sub-millimetric, 0.25 mN resolution fully integrated fiber-optic force-sensing tool for retinal microsurgery*. Int J Comput Assist Radiol Surg. 2009; 4(4): 383-390.
[10] Elayaperumal S, Bae JH, Christensen D, Cutkosky MR, Daniel BL, Black RJ, Costa JM, Faridian F, Moslehi B. *MR-compatible biopsy needle with enhanced tip force sensing*. World Haptics Conferences, South-Korea, Daejeon, 2013.
[11] Ho SC, Razavi M, Nazeri A, Song G. *FBG sensor for contact level monitoring and prediction of perforation in cardiac ablation*. Sensors. 2012; 12(1): 1002-1013.
[12] Rao YJ. *In-fibre Bragg grating sensors*. Meas Sci Technol. 1997; 8(4): 355-375.
[13] Alemohammad HR, Foroozmehr E, Cotton BS, Toyserkani E. *A dual-parameter optical fiber sensor for concurrent strain and temperature measurement: design, fabrication, packaging, and calibration*. J Lightwave Technol. 2013; 31(8): 1198-1204.
[14] Yang Z, Xu H, Ni K, Dong X. *Simultaneous measurement of force and temperature with a single FBG partially encapsulated with a metal cannula*. Microw Opt Techn Let. 2011; 53(7): 1656-1658.

8

Master-slave system for MRI-guided needle steering in liver interventions

Kirsten R. Henken, Cesar A. Lopez Martinez, Maurits S. van der Heiden, Joris E.N. Jaspers, Maarten Steinbuch, Jenny Dankelman, John J. van den Dobbelsteen

This chapter has been submitted for publication.

ABSTRACT

BACKGROUND Robotic systems for needle steering are suggested to improve target accuracy in percutaneous needle interventions. This work aims at the development of an MRI-compatible master-slave system for needle interventions in the liver.

METHOD The system consists of a steerable needle with shape sensing capabilities and units for control and actuation. The orientation of the compliant tip of the steerable needle can be adjusted through manipulation of the steering cables that are integrated in the needle. Optical fibers with fiber Bragg gratings (FBGs) are also integrated in the needle for the purpose of shape sensing. Actuation of the cables and needle insertion is initiated by the physician through manipulation of a master device that controls a set of piezoelectric actuators. The system is experimentally evaluated by steering the needle to a target in a gelatin phantom based on real-time FBG-based visual feedback about the needle shape.

RESULTS Technical evaluations demonstrated the technical feasibility of the system. The preclinical experiment illustrated that the needle could successfully be steered toward a target using the master input device, guided by a projection of the needle's position relative to the target.

CONCLUSION The master-slave system could become a valuable tool for needle steering in percutaneous interventions.

8.1 INTRODUCTION

Target accuracy is crucial for the success of percutaneous needle interventions (e.g. during biopsy taking, ablation procedures, brachytherapy). However, placement errors easily arise during procedures in deep-seated tissue structures, which may lead to faulty diagnosis and suboptimal therapeutic outcomes. Placement errors generally originate from human factors, limitations in visualizing the target, target movement associated with changes in the body (e.g. breathing), and the mechanical interaction between needle and biological tissue [1]. The latter includes errors due to tissue deformation and needle deflection that are influenced by a large number of variables, including the insertion method and the characteristics of the needle and the tissue [2].

Recent approaches to improve the targeting accuracy in percutaneous interventions include path planning based on models that predict tissue deformation and needle deflection [3-7] and the use of robotic systems for steering the needle. Steerable needles allow for active control of the needle trajectory and can compensate for target movement and needle deflection during insertion. Additionally, delicate tissue (e.g. nerves or vessels) can be circumvented and deep structures can be accessed. Well-studied principles in needle steering include needle base manipulation [4, 5], steering with bevel or pre-curved needle tips [8-10], and telescopic mechanisms [11, 12]. The clinical applicability of these robotic systems rely on accurate control that is based on predictive models [1] that describe the interaction between the needle and tissue with unknown properties. This work aims to develop a master-slave system for needle steering that does not require predictive models.

Navigation of steerable needles without using predictive models calls for accurate spatial information about the needle tip and the target while the needle is moving through the human body. Previous research used various imaging techniques, such as ultrasound (US), computed tomography (CT) and magnetic resonance imaging (MRI), to acquire needle position during insertion [13]. US is safe and easy and can be used in real-time, but its contrast is low. CT provides high-contrast images, but is time-consuming and uses ionizing radiation. MRI has excellent contrast in soft tissue and uses magnetic fields and radiofrequency pulses instead of ionizing radiation. Therefore, MRI may be the ideal modality for image-guided needle interventions in the liver, but this requires positioning of the instrument while the patient is situated in the scanner bore. Within the limited space in the scanner, ferromagnetic materials are subject to high magnetic interaction forces, and heating may occur in long conducting parts. Besides this, the use of electricity in the scanner may cause interference leading to imaging artifacts. To this end, nonmagnetic and dielectric instruments and actuators need to be developed that are small enough to be used in confined spaces to ensure the compatibility with MRI.

When such MRI-compatible equipment is available, the next challenge is to provide the position and orientation of the needle relative to the target to the physician. Real-time registration at appropriate update rates of the position of the instruments with respect to the patients anatomy is essential for navigation and exact therapy delivery. Information about the needle position can be obtained from the images of the MRI. However, the current state of the art is slow and can only be used real-time at the expense of resolution or size of the imaged area. Besides this, the time lag of the systems needs to be small to allow for dexterous navigation. A promising approach to accurately obtain needle position in real-time is based on the use of fiber Bragg grating technology.

A fiber Bragg grating (FBG) is a grid etched onto the core of an optic fiber and acts as a strain sensor [14]. Multiple FBGs can be incorporated in a single fiber and the small size of the fibers allows for integration of multiple fibers in thin devices such as needles. The fiber itself serves as the signal conduit, so that no electrical circuit is required for read-out, which makes the technology suitable for application in MRI. FBGs have the property to reflect specific wavelengths of light that shift when strained. FBGs can be used to measure the axial strain along the length of the needle and can thereby be used to measure its deflection. A number of studies integrated FBGs in needles [15-18] and illustrated tracking of needle deflection at high sampling rates (>20 kHz). The reconstructed shape of the needle inside the body of the patient can be used for robotic control or as visual feedback through an overlay in the MR images. This will reduce problems with uncertainties in needle position due to needle deflection and target movement.

The objective of this study is to develop a master-slave system consisting of a steerable MRI compatible needle with precise position sensing for navigation in percutaneous interventions. The system is designed for needle insertion in the liver, but is suitable for a variety of procedures in the abdominal or thoracic area. To obtain this goal, the following technologies are combined: needles with cable-actuated compliant tips to allow for readjustment of the tip orientation and steering angle; real-time FBG-based sensors for the measurement of needle shape; and nonmagnetic piezoelectric actuators and driving mechanisms to enable positioning of instruments within the MRI scanner. Extensive modelling of needle-tissue interactions and real-time imaging with high update rate are not needed in this system, because the needle path can be adjusted at any time through manipulation of the needle tip based on the real-time FBG-based shape sensing. The driving mechanism to steer and to insert the needle is controlled by the physician through a master input device to ensure the safety of the interventions.

The overall accomplishment of the work is the realization of a fully actuated needle with precise position sensing that can remotely be steered in an MRI environment. An experiment is performed in which the needle is inserted into a gelatin phantom towards a target using the master input device. To the best of the authors' knowledge, no other studies have realized a setup that integrates all these components into one system. The first section of this paper presents the main components of the system: the cable-actuated compliant needles; integrated FBG-based shape sensing; the driving system based on piezoelectric actuators and capacitive rotary sensors; and the master device and control algorithms used to drive the actuators. The second section describes the experimental setup with which the functioning of the system is validated. The experimental results on steering a needle towards a target in a gelatin phantom are also presented in this section. Finally, this work is concluded and directions for future work are provided.

8.2 SYSTEM DESIGN

8.2.1 Overview

An overview of the robotic system is provided in Figure 8.1. Since large parts cannot be positioned in the limited space of the scanner bore, the actuator unit that takes care of the insertion and steering of the needle has to be situated outside of the scanner bore. The distance between the actuator unit and the point of insertion in the patient is bridged by means of a guiding tube. The steerable needle with FBGs for shape sensing runs through this guiding tube and accesses the body through a trocar that is attached to the patient. Markers on the trocar enable alignment of the coordinate systems of the scanner and the FBG-based shape sensors. The master device and the control unit drive the actuators and can be placed inside or outside the MRI room together with the interface for the physician. The specifications of the steerable needle, the guiding tube and trocar, the shape sensing with FBGs, the actuation system, and the master device and control unit are elaborated on in this section.

The process of applying the system in clinical practice comprises the following steps. The physician determines the point of insertion and the pathway based on an initial MRI scan. After that, the trocar is attached to the patient, the actuators are positioned above the patients legs, and the guiding tube is mounted to the trocar. Then, the patient is moved into the MRI scanner and needle insertion can be initiated. The physician steers the

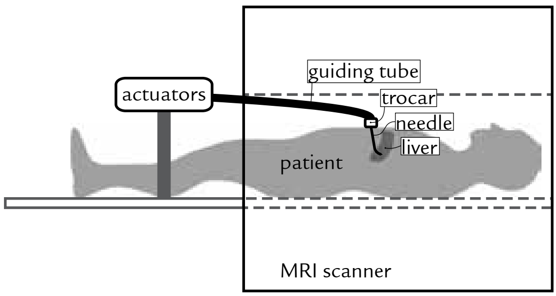

FIGURE 8.1 **Overview of robotic system for MRI-guided needle steering in liver interventions.**

needle to the target position, while MRI scans provide visual feedback about the target position and real-time FBG-based shape sensing provides spatial feedback about the needle tip position. Once the target has been reached, the patient is positioned outside of the scanner and the needle stylet is removed, leaving the outer needle at the target location to serve as a working channel for placement of dedicated interventional tools.

8.2.2 Steerable needle

The needle was designed according to the following three requirements:

- The needle has to be compatible with current instruments. A lumen with a diameter of at least 2 mm is required to provide space to these instruments;
- MR-safety is required. The use of elongated conducting parts or ferromagnetic materials has to be avoided;
- A steering angle (the angle between the direction of the tip and the neutral line of the needle) ranging between 0 and 10° in all directions is required. According to literature [9, 19, 20] and previous findings of the authors this should facilitate a deflection up to approximately 50% of the insertion depth.

Figure 8.2 presents a schematic view of the steerable needle. The needle can be divided in three parts in longitudinal direction: the proximal part; the passively flexible shaft; and the bendable tip with lengths of ca. 1000, 180, and 37 mm, respectively. The proximal part is completely situated in the guiding tube. Its function is to bridge the distance between the actuators and the trocar and to transmit needle insertion and actuation of the tip. The curvature of the passively flexible shaft is not controlled directly, but follows the direction of insertion introduced by the needle tip. Eight compliant hinges are integrated in the bendable tip to allow for the initiation of steering. The degree and direction of bending of the tip can be adjusted by pulling one or two of the steering cables that run through the wall of the needle and are attached to the distal end of the needle.

The steerable needle consists of a working channel with an outer and inner diameter of 3.2 and 2.0 mm, respectively and a cutting stylet with a diameter of 1.9 mm. The cutting stylet runs through the working channel and can be replaced by a therapeutic instrument

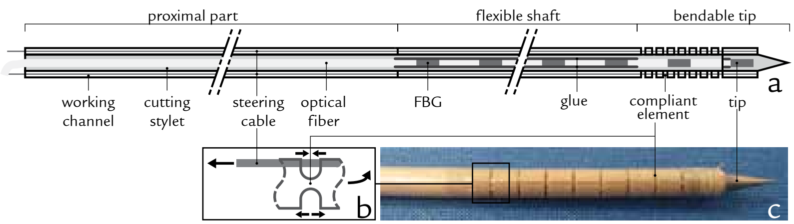

FIGURE 8.2 Overview of the needle with the actuated tip and its working principle.

when the target has been reached. The cutting stylet consists of a PEEK tube, a flexible part made out of Teflon, and a titanium conical tip that are connected to each other by means of press fittings. Grooves of 0.30 mm are milled along the length of the cutting stylet in which the optic fibers for shape sensing are integrated. The working channel is a PEEK tube in which four grooves are milled in longitudinal direction to provide space for the Dyneema steering cables (Nanofil, Berkeley, USA). In addition, four pairs of radial grooves are milled in the distal part of the working channel to create hinges in the tip. The four pairs are oriented in 45° with respect to each other to allow for deflection of the tip in all directions. The working channel is covered with a PET shrinking tube (103-0302, Vention Medical – Advanced Polymers, USA).

8.2.3 Guiding tube and trocar

The function of the guiding tube is to support the needle part that bridges the distance between the actuator and the point of insertion. Sufficient stiffness is required to avoid buckling of the needle during insertion and to make sure that actuation of the steering cable only affects the steerable tip. At the same time, sufficient flexibility is required to allow for adjustment of the point of insertion and initial needle orientation and to compensate for breathing motions of the patient's thorax. The function of the trocar is to provide a passage between the guiding tube and the patient and to fixate the point of insertion and initial orientation of the needle. Both the guiding tube and the trocar have to be MRI safe and biocompatible.

The guiding tube and the trocar are visualized in Figure 8.8. The 720 mm guiding tube is made out of POM and Teflon and has an inner and outer diameter of 4.0 and 10 mm, respectively. The trocar consists of three main parts: the fixation unit, the orientation unit, and the trocar itself. The fixation unit is a Ø75x30 mm cylindrical block made of POM with a flange that can be attached to the abdomen by means of a large plaster. The cylindrical orientation unit provides a passage for the trocar and can be rotated in the fixation unit to adjust the orientation of the trocar. The trocar is a PEEK cannula that is inserted through the orientation unit after the abdominal wall has been punctured.

8.2.4 Shape sensing

FBG-based shape sensing is integrated in the needle to provide information about the position and orientation of the needle tip. Three fibers that contain multiple FBGs each need to be incorporated in a needle to allow for shape sensing. When the FBGs in the fibers are aligned with each other, strain is measured at three locations within one cross-section. The degree and direction of bending can be reconstructed at this position based on these three strains. The shape of a device (e.g. the needle) can be reconstructed through interpolation of the strains and translation of the bending properties to spatial coordinates along the needle.

Three optical fibers (HI-780 Specialty fiber, Corning Incorporated, Corning, USA) with six FBGs each are integrated in the cutting stylet of the current device (Figure 8.2). The most distal FBGs are positioned 7.0 mm away from the tip and serve as temperature sensors, because they are not glued to the cutting stylet and consequently experience no strain. The spacing in between the FBGs is 40 mm. The FBGs in the bendable tip are glued to the cutting stylet just before and just after the bendable tip, so that they register the mean bending of the bendable tip. The other FBGs are glued along the complete length of the flexible shaft and register local bending.

The FBGs in the optical fibers are aligned with each other to enable reconstruction of bending at the sensor locations and estimation of the shape of the complete needle. A schematic view of a cross section of the cutting stylet at the location of three FBGs is shown in Figure 8.3. The maximal strain (ε_{max}), which represents the degree of bending, and the direction of bending (α) relative to Fiber A are implicitly defined by

$$\varepsilon_A = \varepsilon_{max} \cos(\alpha) + \varepsilon_0 \tag{8.1}$$

$$\varepsilon_B = d_B / d_A \, \varepsilon_{max} \cos(\beta_B + \alpha) + \varepsilon_0 \tag{8.2}$$

$$\varepsilon_C = d_C / d_A \, \varepsilon_{max} \cos(\beta_C + \alpha) + \varepsilon_0 \tag{8.3}$$

where ε_A, ε_B, and ε_C are the strains measured by the FBGs in Fiber A, B, and C, respectively. The distances between the centerlines of the fibers and the cutting stylet are d_A, d_B, and d_C and the orientations of Fiber B and C relative to Fiber A are β_B and β_C, respectively. The degree and direction of bending are interpolated and translated to 3-D coordinates of the needle. The model for FBG-based shape sensing is further elaborated on in previous work [17].

The shape sensing cutting stylet was calibrated to evaluate the actual cross sectional geometry (d_A, d_B, d_C, β_B, and β_C) of each trio of FBGs. The complete needle (i.e. cutting stylet and working channel) was subsequently placed in two different 3.0 mm grooves (one straight and one curved with a constant radius of 700 mm) and manually rotated around its longitudinal axis, while the output of the FBG was registered with an interrogator (Deminsys, Technobis, the Netherlands). The strain in each FBG in the curved groove was determined relative to the mean output of each FBG in the straight groove. Plotting the strains in two FBGs of one cross section results in an elliptical curve. The angulation of the ellipse corresponds to the orientation of the FBGs relative to each other. The horizontal and vertical extremes relate to the distances of the two FBGs to the centerline of the needle. The geometry per FBG trio is shown in Figure 8.4. Previous works [17, 18] describe the calibration method more extensively.

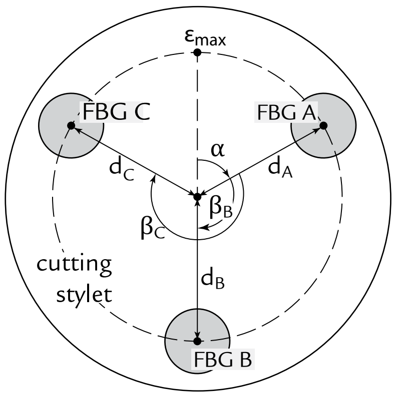

FIGURE 8.3 **Schematic view of the cross section of the cutting stylet. The maximal strain (ε_{max}) due to bending at a distance d_A from the centerline is determined based on strains measured by the FBGs. The direction of bending (α) and the orientations of Fiber B and C (β_B and β_C, respectively) are defined relative to FBG A.**

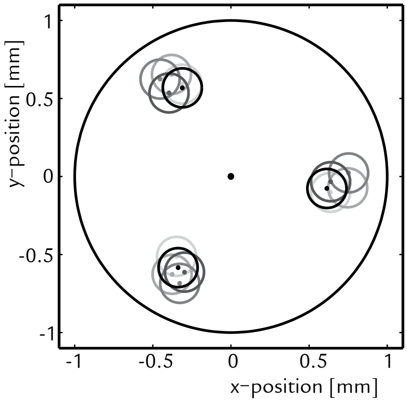

FIGURE 8.4 **Calibrated positions of the FBGs. The FBGs in one cross section are shown in the same color.**

8.2.5 Actuation unit

The actuation was designed according to two main requirements.

- The actuators have to control three degrees of freedom: the insertion of the needle in z-direction and the deflection of the tip in x- and y-direction by pulling one or two of the four steering cables. The required insertion force, velocity and stroke in z-direction were estimated to be 20 N, 10 mm/s, and 250 mm, respectively. The corresponding required accuracy was estimated to be 354 μm (500/√2 μm). The required steering force, velocity and stroke for actuation of the needle tip in x- and y-direction were estimated to be 10 N per cable, 14 mm/s, and 14 mm, respectively. The corresponding required accuracy was estimated to be 20 μm.
- The actuation unit, including the actuators, sensors, and supporting structures has to be compatible with the MRI environment. No significant distortions or artefacts in the MR images are allowed to be introduced by the presence of the actuation unit in or around the MRI scanner. No unsafe effects can be introduced by the MRI in the functioning of the actuation unit.

The materials applied in the actuation unit are selected based on the following experiment that aimed at verifying the distortion of MR images introduced by various materials. First a cylindrical phantom filled with 3L mineral oil was positioned in a head-coil for signal reception and inserted in the bore of a 7T MRI scanner (Achieva 7T whole body MRI, Philips Healthcare, the Netherlands). A 3-D scan with demanding settings (field-of-view: 200x200x101 mm3; voxel size: 1 mm; echo time: 5 ms; repetition time: shortest;

read-out bandwidth: 1325.7 Hz; scan duration: 1 min 1s) was made for reference. Then three or four samples (Ø25x50mm) and a water bottle were attached to the cylindrical phantom. The samples were made out of Pertinax, PA, POM, PI, PEI, PSU, PPSU, PMMA, PTFE, PVC, PEEK, bearing bronze, brass, bronze, copper, aluminum 6082, titanium and stainless steel (304 and 316). This set-up was positioned in the scanner bore and imaged according to the previously described settings. Afterwards, the resulting MR images were compared to the reference images of the phantom. Figure 8.5 presents two examples: Figure 8.5a-b show the artefacts introduced by samples of Pertinax, POM, PTFE, and PVC in the horizontal images at 12 mm above the bottom; Figure 8.5c-d show the artefacts introduced by samples of bearing bronze, brass, bronze, and copper at 10 mm above the bottom. Materials that did not disturb the image in the field-of-view and can consequently be applied include plastics except Pertinax and particular metals when used in small dimensions (copper, aluminum 6082 and stainless steel 316).

The actuator unit is presented in Figure 8.6. The actuator unit (410x180x125 mm) consists of three main units: the base unit; the steering unit; and the insertion unit. The POM base unit consists of a base plate with two linear guides with aluminum rails that guide the steering unit during insertion. The insertion unit is attached to the base unit and houses a piezoelectric actuator (HR-2, Nanomotion, Israel) with a capacitive rotary encoder (DS-25, Netzer, Israel) with a resolution of 0.011°. Rotation of the actuator introduces a forward or backward movement of the steering unit through a belt transmission. The steering unit contains four of the same piezoelectric actuators with four optical rotary encoders. Each of the steering cables is attached to one of the actuators so that each steering cable can be controlled individually through rotation of one of the actuators. All requirements regarding force, velocity and stroke were accomplished in this actuator unit, except for the insertion force and stroke which were measured to be 13 N and 200 mm, respectively.

The encoders are situated in a dedicated copper enclosure to suppress the disturbing RF-field. The rotary shaft and the optical fibers for signal output run through small copper pipes that serve as 'waveguides beyond cut-off' to minimize the compromising effect of the passages. The electrical power supply is provided through a coaxial cable that enters the enclosure through a separate compartment with RF-and lowpass-filters.

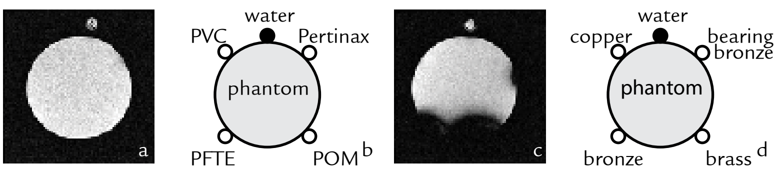

FIGURE 8.5 **MR images of the phantom with material samples. Horizontal MR image at 12 mm (a) or 10 mm (c) from the bottom of the set-up displayed in (b) and (d), respectively.**

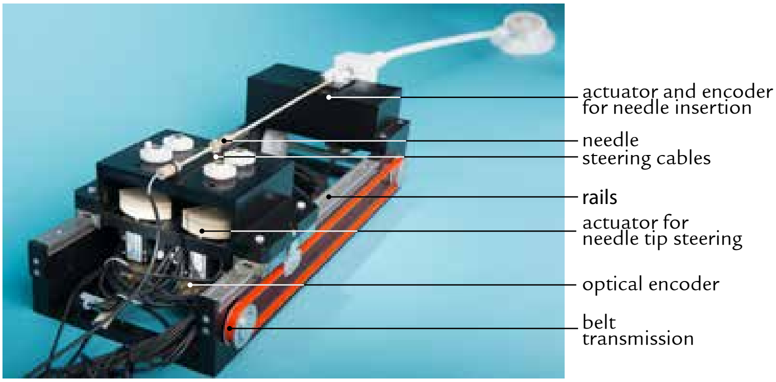

FIGURE 8.6 Actuator unit with five actuators and encoders that control needle insertion and steering through four steering cables.

An experiment was executed to verify the influence of the MRI on the encoders. The complete actuator unit was switched on and placed in the bore of an MRI scanner. A scan was made according to the same settings as describe previously, while the output of the encoders was registered and stored for analysis afterwards. The maximal distortion on the output signal was 0.033°. This corresponds to 15 μm elongation of the steering cables, which results in an angular error of 1.0° at the steerable needle tip. In addition to this, preprogrammed motions of the actuators were executed while scanning. Visual inspection revealed no distortion of the actuator motions and the homing position after movement was always within the distortion of 0.033°.

8.2.6 Master device and control

The physician or operator interacts with a master device to remotely provide the steering commands which are processed by a control system that sends reference positions to the needle actuators. The haptic master device (OMEGA 3, Force Dimension, Nyon, Switzerland) has three translational degrees of freedom and a USB-interface. Figure 8.8 depicts the device together with its strictly local coordinate system. At the initialization phase, the master device is set to its initial position. To facilitate the steering process,

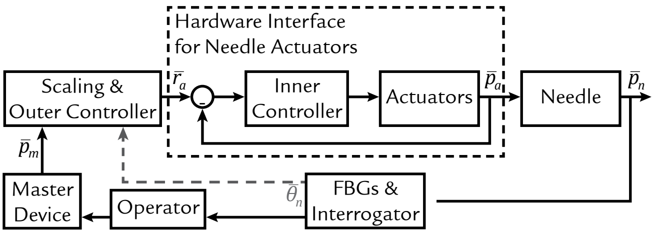

FIGURE 8.7 Diagram of the control software for needle steering.

a virtual spring is implemented around the zero position. The operator can move the device along the x_m and y_m-axis to control the actuators that drive the steering cables. The position of the master device is taken as a velocity command, which is used to compute the desired position of the actuators. Manipulation of the device along the z_m-axis controls the insertion of the needle and is only effective when the knob in the handle is pushed in simultaneously. The z_m-position is also interpreted as a velocity command in the control software.

The control software runs in a Linux PC under Ubuntu operating system. The software is developed in Matlab & Simulink and runs at a sample rate of 1024 Hz. The control software diagram is presented in Figure 8.7. The position vector of the master device $\bar{p}_m=[x_m, y_m, z_m]$ is taken as a velocity command, which is integrated and scaled by the control software to compute the actuators reference vector $\bar{r}_a$. The hardware interface for the needle actuators has a build-in controller, which steers the needle actuators such that the desired $\bar{r}_a$ is followed by the actuators position $\bar{p}_a$, which is coupled to the needle position $\bar{p}_n=[\theta_{nx},\theta_{ny}, z_n]$, where θ_{nx} and θ_{ny} are the needles tip angles and z_n represents the translation of the needle.

8.3 EXPERIMENT

The aim of the experiment was to demonstrate that the needle trajectory could be controlled using visual feedback about the needle shape based on FBG measurements. The set-up of the master-slave system during the experiment is presented in Figure 8.8. The needle was inserted and steered in a gel phantom (10% gelatin in 5L water in a 15x17x21 cm transparent box) to reach a 2 cm target. The operator manipulated the master device to insert and steer the needle towards the target without direct vision of the phantom and the target. Spatial information about the needle and target was provided to the operator on the navigation interface. In this interface, a virtual representation of the target was shown within a projection of an orthogonal 3-D coordinate system. The FBG-based shape of the needle part that was inserted in the phantom was displayed relative to the target with an update-rate of 100 Hz. The z-axis of the 3-D coordinate system coincided with the initial direction of insertion and the x- and y-axes were oriented in horizontal and vertical direction, respectively. The two projections of the 3-D needle shape were displayed in two separate 2-D graphs that showed left-right and up-down motions of the needle, respectively. The position of the needle tip in the gelatin phantom was verified when the operator indicated that the virtual target in the navigation interface had been reached.

The following steps were executed before the experiment was started.

- Connecting the steerable needle to the actuators - The needle was placed in the guiding tube, the guiding tube was attached to the actuator unit, the actuators and the master device were activated, and the actuators were moved to their initial position. The steering cables were attached to the actuators in such way that manipulations of the master device corresponded to the steering directions at the needle tip.
- Calibrating the FBG-based shape sensing - The coordinate system of the FBG-based shape sensing was aligned with the coordinate system of the steerable needle by rotating the FBG-coordinate system around the z-axis until a visual match was obtained. The wavelengths reflected by the unstrained FBGs were registered when the needle was straight to serve as a reference, based on which the strain in the FBGs could be determined during needle insertion.
- Assembling the system on the phantom - The trocar was positioned on top of the gelatin phantom and the guiding tube was attached to the trocar. The needle was inserted through the trocar until the needle tip was just penetrating the phantom.
- Measuring the position of the target - The position of the target in the phantom was determined relative to the point of insertion and orientation of the tube. The target position was [-17.5,-8.2,128.7 mm], which was implemented in the navigation interface.

In the experiment, the needle tip was advanced until it successfully reached the target. All navigation could be performed with the master-slave system, while guidance was provided solely based on FBG-based visualization of the needle shape and its tip position. During testing, it was observed that the stiffness of the guiding tube was insufficient to keep the proximal part of the needle straight, so that actuation of the needle tip resulted in a slight curvature along the entire length of the needle instead of the intended local deflection of the tip. In addition, occasionally slip occurred in the actuators and in the connection between the steering cables and the actuators, resulting in disturbances in the transfer of the input signal provided at the master device to the actual steering motion.

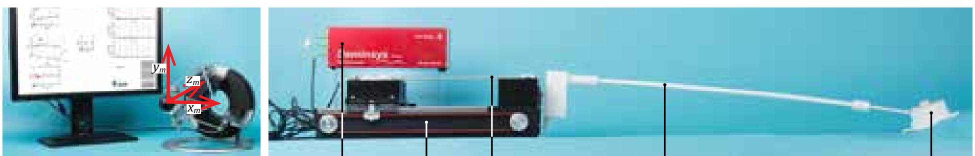

FIGURE 8.8 **Overview of the master-slave system.**

8.4 DISCUSSION

Performing procedures in anatomical structures that cannot be reached with currently available instruments remains a major challenge in the field of interventional radiology. This study establishes the feasibility of master-slave systems to support needle steering in MRI guided percutaneous interventions. The proposed solution does not only serve to compensate for targeting errors caused by various sources such as needle deflection, tissue deformation, and target motion, but may also help in targeting areas that cannot be reached in a straight-line trajectory. To this end, a master-slave system was designed that is capable of driving a needle with an actuated tip. FBG-based strain sensing was integrated in the needle for accurate real-time shape reconstruction. The latter enabled visualization of the needle's position for remote control. All components were designed such that the system is suitable for in an MRI environment. In a preclinical study, it was demonstrated that the needle could successfully be steered toward a target using the master input device, guided by a projection of the needle's position relative to the target.

To be accepted in clinical practice, master-slave systems need to fulfill many demands for the technology to have true added value. Cleary et al. [21] discuss the main technical challenges related to the user workflow, the compatibility with imaging techniques, and the registration of the needle position relative to the coordinate system of the image. The workflow of the current system is according to existing workflows for image-guided interventions. However, application of the current master-slave system requires less steps, because the iterative process of moving the patient in and out of the scanner is avoided. Moreover, the safety of the system is one of the first properties that needs to be satisfied. In medical applications, the stability and reliability of the control system for positioning the effector are critical elements of safety. In the case of percutaneous interventions, the needle path is highly influenced by the variability in the mechanical properties of the penetrated tissue. Therefore, control systems that directly monitor the needle's position are essential to ensure the safety of the techniques.

Several MRI-compatible needle placement systems for percutaneous procedures have been reported before, most of them specifically designed for prostate interventions [22-27]. A major contribution of the current work is the development of a complete master-slave system for interventions in the liver or other organs in the abdominal or thoracic area. The system can operate safely in an MRI environment. This was accomplished by applying only MRI safe materials in the final design of the needle and the actuator unit. The actuator unit combines inserting the needle and cable-driven actuation of the steerable needle tip and consists of piezoelectric actuators with capacitive rotary encoders in copper enclosures to minimize their interaction with the MRI. Experiments in a 7T MRI scanner showed that the developed components did not affect the image quality. So far, the MRI safety and robustness of this actuator unit was only evaluated in terms of distortion of the encoder. No heating tests, MRI quality assessment, or extensive failure analysis have been performed.

Needle steering has been suggested to enable accurate targeting. Several steering strategies and corresponding models for control have been suggested [1, 4, 5, 8-12]. Reed et al. [28] present a portable system for needle steering under fluoroscopy for thin (< 1 mm) needles with a pre-curved, beveled tip. Bernardes et al. [29] report on a closed-loop robotic system that steers a beveled needle based on intra-operative imaging feedback to (re)plan the needle trajectory. Burgner et al. [30] present a robotic system for needle steering in the brain based on the telescopic mechanism. The MRI-compatible robotic system described in [26, 27] enables control over the direction of the needle inside the tissue using the principle of bevel-tip steering. In our approach, steering is based on actuation of the needle tip. We developed a system that controls the direction of the needle by adjusting the orientation of the needle tip through a combination of compliant hinges and steering cables. To achieve sufficient axial and torsional stiffness, most of the needle was fabricated from PEEK. At the same time, elasticity of PEEK was sufficiently high to allow for sufficient bending at the tip. Another major benefit of this material is that it can easily be machined, which allows for introduction of the compliant hinges and the grooves that accommodate the steering cables and optical fibers. The Dyneema steering cables have sufficient stiffness and strength, but it was difficult to ensure equal pretension on the cables and some limitations were observed during testing of the robustness of actuation. When the guiding tube is curved, a slack is introduced in some of the steering cables. This reduces the responsiveness of the needle tip to the user's steering actions. Additionally, slip between the wires and the pulleys of the actuators was observed during the experimental testing.

The possibility to integrate FBG-based shape sensing in the needle for active tracking of needles in MRI environments has been successfully applied before [15, 16]. FBGs are ideal for application in MRI, because of their insusceptibility to electromagnetic interference, biocompatibility and sterilizability, which makes them inherently safe. Their ability to detect very small strains allows for highly accurate measurements of local deformations. Henken et al. [16] found an accuracy of less than 1 mm in the estimation of the needle tip position for single deflections of an 18G trocar needle, which seems sufficient for most existing applications. However, the need for calibration and robust alignment of the coordinate system of the sensors relative to the coordinates systems of the actuators, master device, and MRI scanner is still a challenge [17]. In the current study the coordinate system in which the needle operates was only visually aligned with the coordinate system in which the reconstructed shape was projected. The alignment needs to be improved before accuracy and reproducibility of the system can be quantified.

Master-slave systems allow for various user interfaces, but the most suitable and intuitive interface for an interventional robot has yet to be determined. For the current experiment, a commercially available master device was used that offers three active translations. The position of the master device's handle was taken as a velocity command to drive the needle. Alternatively, a position signal could have been used as the workspace of the master device is sufficiently large to accommodate the full needle trajectory. The exact choice of interface may influence the required operator training and corresponding learning curve as well as the physicians dexterity in the most complex and stressful situations [31]. From the safety perspective, it is preferred to keep the physician firmly in control, because the current master-slave systems do not offer bilateral control that is sufficiently robust to ensure safe use in medical applications. In the current study, shape sensing was only used to visualize the needle, while the user was in full control over the needle path. In the future, FBG-based shape sensing could be used to control the needle tip via a feedback loop as indicated in Figure 8.7. Optimization of the system is needed to avoid undesired movement of the needle introduced by signal noise and inaccuracies in order to guarantee safety. However, despite the possible advances of such automation, it may be desirable to keep a human operator in the loop that can mediate the uncertainties in the environment and manage the complexities of the procedures.

8.5 CONCLUSION

This paper presents a novel concept for an MRI-compatible master-slave system for percutaneous interventions. It introduces a novel needle steering approach based on active control of the needle tip together with a visual feedback concept based on FBG-based needle shape reconstruction. A basic preclinical test in a gelatin phantom showed that our system could become a valuable tool for the performance of percutaneous procedures in difficult to reach anatomical structures.

REFERENCES

[1] Gao DD, Lei Y, Zheng HJ. *Needle steering for robot-assisted insertion into soft tissue: a survey.* Chin J Mech Eng. 2012; 25(4): 629-638.
[2] Van Gerwen DJ, Dankelman J, Van den Dobbelsteen JJ, *Needle–tissue interaction forces–A survey of experimental data.* Med Eng Phys. 2012; 34(6); 665-680.
[3] DiMaio SP, Salcudean SE. *Needle steering and motion planning in soft tissues.* IEEE T Bio-Med Eng. 2005; 52(6): 965-974.
[4] Glozman D, Shoham M, *Image-guided robotic flexible needle steering.* IEEE T Robotic Autom. 2007; 23(3): 459-467.
[5] Misra S, Reed KB, Schafer BW, Ramesh KT, Okamura AM. *Mechanics of flexible needles robotically steered through soft tissue.* Int J Robot Res. 2010; 29(13): 1640-1660.
[6] Park W, Wang Y, Chirikjian GS. *The path-of-probability algorithm for steering and feedback control of flexible needles.* Int J Robot Res. 2010. 29(7); 813-830.

[7] Webster RJ, Kim JS, Cowan NJ, Chirikjian GS, Okamura AM. *Nonholonomic modeling of needle steering.* Int J Robot Red. 2006; 25(5-6): 509-525.

[8] Majewicz A, Marra S, Van Vledder M, Lin M, Choti M, Song D, Okamura A. *Behavior of tip-steerable needles in ex vivo and in vivo tissue.* IEEE T Bio-Med Eng. 2011; 59(10): 2705-2715.

[9] Engh JA, Podnar G, Kondziolka D, Riviere CN. *Toward effective needle steering in brain tissue.* 28th IEEE/EMBS, USA, New York, 2006.

[10] Webster R, Okamura AM, Cowan NJ. *Toward active cannulas: Miniature snake-like surgical robots.* International Conference on IEEE/RSJ. China, Beijing, 2006.

[11] Dupont PE, Lock J, Itkowitz B, Butler E. *Design and control of concentric-tube robots.* IEEE T Robot. 2010; 26(2): 209-225.

[12] Crocetti L, Della Pina C, Cioni D, Lencioni R. *Peri-intraprocedural imaging: US, CT, and MRI.* Abdom Imaging. 2011; 36(6): 648-660.

[13] Hill KO, Meltz G. *Fiber Bragg grating technology fundamentals and overview.* J Lightwave Technol. 1997; 15(8): 1263-1276.

[14] Park YL, Elayaperumal S, Daniel B, Ryu SC, Shin M, Savall J, Black RJ, Moslehi B, Cutkosky MR. *Real-time estimation of 3-D needle shape and deflection for MRI-guided interventions.* IEEE ASME Trans Mechatron. 2010; 15(6): 906–915.

[15] Henken K, Van Gerwen D, Dankelman J, Van den dobbelsteen JJ. *Accuracy of needle position measurements using fiber Bragg gratings.* Minim Invasiv Ther. 2012; 21(6): 408-414.

[16] Henken KR, Dankelman J, Van den Dobbelsteen JJ, Cheng LK, Van der Heiden MS. *Error analysis of FBG-based shape sensors for medical needle tracking.* ASME/IEEE T Mech. Published online 2013 Nov 11; doi: 10.1109/TMECH.2013.2287764.

[17] Van der Heiden MS, Henken KR, Cheng LK, Van den Bosch BG, Van den Braber R, Dankelman J, Van den Dobbelsteen JJ. *Accurate and efficient fiber optical shape sensor for MRI compatible minimally invasive instruments.* Proc SPIE-Int Soc Opt Eng. 2012; 8550.

[18] Okazawa S, Ebrahimi R, Chuang J, Salcudean SE, Rohling R. *Hand-held steerable needle device.* IEEE/ASME T Mech. 2005; 10(3): 285-296.

[19] Sitzman BT, Uncles DR. T*he effects of needle type, gauge, and tip bend on spinal needle deflection.* Anesth Analg. 1996; 82(2): 297-301.

[20] Cleary K, Melzer A, Watson V, Kronreif G, Stoianovici D. *Interventional robotic systems: applications and technology state-of-the-art.* Minim Invasiv Ther. 2006; 15(2): 101-113.

[21] Schouten MG, Bomers JGR, Yakar D, Huisman H, Rothgang E, Bosboom D, Scheenen TWJ, Misra S, Futterer JJ. *Evaluation of a robotic technique for transrectal MRI-guided prostate biopsies.* Eur Radiol. 2012; 22(2): 476-483.

[22] Van den Bosch MR, Moman MR, Van Vulpen M, Battermann JJ, Duiveman E, Van Schelven LJ, De Leeuw H, Lagendijk JJW, Moerland MA. *MRI-guided robotic system for transperineal prostate interventions: proof of principle.* Phys Med Biol. 2010; 55(5): 133-140.

[23] Srimathveeravalli G, Kim C, Petrisor D, Ezell P, Coleman J, Hricak H, Solomon SB, Stoianovici D. *MRI-safe robot for targeted transrectal prostate biopsy: animal experiments.* Brit J Urol. 2013. Published online 2013 Dec 2; doi: 10.1111/bju.12335.

[24] Elhawary H, Tse ZTH, Rea M, Zivanovic A, Davies BL, Besant C, Desouza NM, McRobbie D, Young I, Lamperth MU. *Robotic system for transrectal biopsy of the prostate real-time guidance under MRI.* IEEE Eng Med Biol. 2010; 29(2): 78-86.

[25] Seifabadi R, Cho NBJ, Song SE, Tokuda J, Hata N, Tempany CM, Fichtinger G, Iordachita I. *Accuracy study of a robotic system for MRI-guided prostate needle placement.* Int J Med Robot Comp. 2013; 9(3): 305-316.

[26] Seifabadi R, Song SE, Krieger A, Cho N, Tokuda J, Fichtinger G, Iordachita I. *Robotic system for MRI-guided prostate biopsy: feasibility of teleoperated needle insertion and ex vivo phantom study.* Int J Med Robot Comp. 2012; 7(2): 181-190.

[27] Reed KB, Majewicz A, Kallem V, Alterovitz R, Goldberg K, Cowan NJ, Okamura AM. *Robot-assisted needle steering.* IEEE T Robotic Autom. 2011; 18(4): 35-46.

[28] Bernardes MC, Adorno BV, Poignet P, Borges GA. *Robot-assisted automatic insertion of steerable needles with closed-loop imaging feedback and intraoperative trajectory replanning.* Mechatronics. 2013; 23(6): 630-645.

[29] Burgner J, Swaney PJ, Lathrop RA, Weaver KD, Webster RJ. *Debulking from within: a robotic steerable cannula for intracerebral hemorrhage evacuation.* IEEE T Bio-Med Eng. 2013; 60(9): 2567-2575.

[30] Chen JY, Haas EC, Barnes MJ. *Human performance issues and user interface design for teleoperated robots.* IEEE T Syst Man Cy C. 2007; 37(6): 1231-1245.

9

Discussion

Various percutaneous therapies for liver cancer have been introduced over the past few decades, including ablation and brachytherapy. In these therapies, a needle is used to administer the therapy locally at the target site. Accurate positioning of the needle is crucial in these procedures in order to maximize the effect of the treatment and minimize the damage to the surrounding tissue. Accurate needle positioning can be impaired by unintended needle deflections initiated by the interaction between the needle and the tissue that it encounters during insertion. The straight and rigid needles that are currently utilized in clinical practice do not allow for adjustment of the trajectory once the needle has entered the tissue. Consequently, accurate targeting can be challenging to the physician and reinsertion of the needle is commonly required.

A second challenge in percutaneous needle interventions is the visualization of the target and the needle during insertion. Currently, US or CT are most commonly used for visualization. Yet, US provides only limited spatial resolution and CT carries the risks of ionizing radiation. MRI has been suggested to be superior in these interventions because of its high contrast in soft tissue, flexibility in selection of the position and orientation of the imaging planes or volumes, and absence of ionizing radiation. Still, it is rarely applied in clinical practice for guidance of percutaneous needle interventions, for fast imaging sequences with appropriate resolution and field-of-view as well as MRI-compatible instruments are scarcely available.

The work presented in this thesis focused on the development of 'smart needles' that aim at improving the needles that are used for MRI-guided percutaneous interventions in the liver by utilizing dexterous navigation and visual guidance during insertion to allow for accurate targeting. The major goals were: (I) to add steerability to needles for MRI-guided interventions; (II) to enable tracking by incorporating FBG technology in the needles; and (III) to integrate steerability and FBG-based needle tracking in a robotic device. The current chapter reflects on the approach that was taken, the challenges that needed to be overcome to reach these goals, and the results that were obtained so far. This chapter also provides an outlook to further developments and future research.

9.1 NEEDLE STEERABILITY

Three main steering mechanisms were previously proposed in literature: base manipulation; telescopic mechanisms; and asymmetric needles. The steering concept presented in this thesis builds on the steering method that uses the inherent steering induced by asymmetric tips. The needles utilized in this steering method had either a bevel tip or a pre-curved tip. The degree and direction of steering can only be adjusted by rotating the needle. The new concept enables actuating the needle tip in order to control the degree of the asymmetry and its orientation, so that rotation is no longer required. This allows for more intuitive control of the needle compared to previously suggested steering methods. Besides this, the current concept, in contrast to the other steering mechanisms, does not require extensive a priori planning of the needle trajectory and complex control strategies. The main challenge in designing this concept was to combine axial rigidity, required to avoid buckling, with radial flexibility, required to allow for the adjustment of the curvature and the orientation of the tip. In addition, we aimed to integrate the steering mechanism in a needle that is compatible with MRI and to develop a handle that allows for intuitive manual control.

Two prototypes of MRI-compatible, steerable needles were realized. Axial rigidity and radial flexibility were combined in a cable-hinge mechanism that was first presented in Chapter 2 Several techniques were considered for manufacturing of the hinges, including laser cutting and rapid prototyping. This first prototype was used to gain insight in the range of curvatures and tip angles that are required for needle steering in tissue. The cable-hinge mechanism was simplified through the introduction of compliant hinges in the second prototype (Chapter 3), which dramatically reduced the number of parts and confined the manufacturing process to conventional techniques. This second prototype contains a handle for manual control and allows to introduce the required steering angles that were identified with the first prototype. The materials used in this prototype were carefully selected for MRI-compatibility. The performance of this second prototype was demonstrated in an MRI-guided procedure in which multiple locations in a gel model were successfully targeted.

The work on needle steering mechanisms presented in this thesis demonstrates the feasibility of actively controlling the needle trajectory during insertion and obtaining high targeting accuracy. The challenge that remains is to further develop the design into an instrument that is ready for implementation in clinical practice. The steering mechanism should be integrated with the therapeutic function (e.g. ablation). The interaction between the steering mechanism, the therapeutic function, and the MRI environment in the application of such a combined device should be investigated. Because of the utmost importance of instrument safety, it might be desirable to further reduce the number of individual parts in the needle (the cables, the shrinking tube, the tip, and many more). Finally, the value of this new needle for clinical practice has to be demonstrated to both physicians and managers.

9.2 FBG-BASED NEEDLE TRACKING

Accurate targeting requires intra-procedural information about the needle tip position. Currently, such information is typically retrieved from the intra-procedural MR-images through the integration of passive or active trackers. The number of active trackers that can be integrated in a needle is limited by the signal conduits required for each tracker. This is not the case in passive trackers, but these only provide visualization of the needle rather than quantification of its position and orientation. The update rate of both active and passive trackers depends on the imaging frequency, which can be increased at the cost of field of view or spatial resolution. In this work, spatial information about the needle was acquired by utilizing FBG technology. Multiple FBGs can be incorporated in small devices like medical needles, because a single optical fiber with a typical diameter of 250 μm is able to carry multiple FBGs and to serve as conduit for its output signal at the same time. In addition, FBGs can be read-out at frequencies up to 20 kHz without compromising the field of view or resolution and allow for accurate quantification of the needle shape and the tip position.

We expected that FBG-based sensing could be operationalized quickly, yet significant work was required. Accurate positioning of the FBGs within the fibers was found to be difficult and assembling the sensors in a needle was challenging because of the small size of the optical fibers and the needle, the brittleness of the glass, and the difficulties that accompany a gluing process. Besides this, an appropriate configuration of the FBGs (number of sensors and their positioning and spacing), a model for estimating the shape of a needle based on the FBG outputs, and a method for calibration of the FBGs had to be defined.

Despite the challenges mentioned above, three prototypes for shape sensing and one prototype for force sensing were realized and evaluated. Initial insights regarding assembling optical fibers in a medical needle, defining a model for FBG-based shape sensing, and 2-D accuracy of shape sensing were discussed in Chapter 4. It was expected that a higher accuracy was feasible by increasing the number of FBGs, optimizing the shape sensing model and the positioning of the FBGs, and applying calibration to find the true geometry of the FBGs. These expectations were verified in Chapter 5 where the separate and combined effect of these factors on the accuracy and the hierarchy of error sources were presented. This study also provided insight in the factors that need to be considered when designing an FBG-based shape sensor, including the shapes that are expected to occur, the length of the instrument, and the accuracy that is required by the application. Based on the previous findings, a third prototype with an optimized model for shape sensing was prepared (see Chapter 6). The performance of this prototype was evaluated in a clinical setting by quantifying the 3-D accuracy based on CT images. Finally, a force sensing needle was manufactured and evaluated (Chapter 7). This research provided knowledge about the challenges in measuring forces with an FBG and the accuracy that is required to be relevant for the detection of tissue types.

Currently we are investigating the feasibility of producing autonomous shape sensors for general use in medical instruments. In Chapter 5 a shape sensor consisting of three optical fibers that are glued directly to each other was discussed. Insufficient torsional stiffness in combination with the cross sectional asymmetry of this sensor resulted in limited accuracy. Four other concepts are currently being evaluated. The first concept consists of three optical fibers that are integrated in a PVC rod with a diameter of 1 mm. This shape sensor is designed to be compatible with MRI and is suitable for flexible instruments with a lumen of at least 1 mm. The second concept is a triplet of three miniature fibers (Ø105 μm) that have circular cross sections of approximately 0.3 mm diameter. The potential success of this sensor is determined by its torsional stiffness, which depends on the quality of the glue between the fibers. The bending radii that can theoretically be measured with this sensor approximately range from 5 m to 15 mm, making it more suitable for application in highly flexible instruments, such as catheters. In the third concept, the shape sensor is a single fiber with multiple cores that each contain independent FBGs. Such a shape sensor would enable detecting bending radii of even less than 5 mm. In the fourth and final concept, glass fibers are replaced by plastic fibers that have a higher fracture strain. A sensor of plastic fibers can be subjected to smaller bending radii and would be more robust.

The small size of FBGs and the absence of electronics can be advantageous in demanding environments. The work presented in this thesis provides a framework for designing FBG-based sensors, but still each sensor needs to be designed according to the specific requirements of the application. Limitations of FBGs that have to be considered include the following. Firstly, glass fibers are brittle and therefore vulnerable, which introduces the need for the glass fibers to be handled with utmost care during production, assembly, calibration, and practical use. When the application requires robustness, which is the case in medical applications, strain on the fibers should be bounded to make sure that the sensing system does not fail during use. Alternatively, a possibility to replace the sensing system during use could be incorporated. A second limitation is the cross-sensitivity of FBGs to temperature. Small changes in the temperature of the environment of the sensor affect the output of the FBG (see Chapter 7), which hampers the accuracy of absolute strain measurements with a single FBG. In applications that require stable, accurate, and absolute strain measurements (e.g. in force sensing), compensation for temperature differences has to be incorporated. A third limitation results from the effect of the components or structures that surround the FBG. For example, significant effects of the PVC jacket around the FBG were observed in the force sensing needle. These limitations indicate that each FBG-based sensor needs to be designed and produced meticulously. Unfortunately, no accurate off-the-shelve solutions are available yet.

9.3 INTEGRATION OF STEERABILITY AND TRACKING

The last goal of this thesis was to integrate steerability and FBG-based tracking in a needle for MRI-guided interventions. The confined space in the bore of an MRI-scanner calls for remote control of the needle. This could either be realized through the development of a steering mechanism that is able to bridge the distance, a master-slave system, a computer-controlled robot, or a combination of these options. The accomplishment of the work presented in this thesis is the realization of an MRI-compatible master-slave system for fully actuated needle steering with FBG-based tracking. To the best of our knowledge, this is the first study to demonstrate integration of FBG-based needle tracking into an MRI-compatible system.

The design and evaluation of the steerable needle with FBGs, the actuators, and the control of the system was presented in Chapter 8, together with an initial demonstration of the function of the integrated system. Since the system was intended for use in MRI-guided interventions, all parts had to be designed to be compatible with the magnetic field and radiofrequency pulses of the MRI. Basically no ferromagnetic materials or elongated conductors -and consequently no electromagnetic motors- could be applied in the system, which limited the material choices to different materials (e.g. PEEK) and working principles (e.g. piezoelectric motors) than conventionally used in clinical practice. Besides that, the aim was to develop a system that improves the accuracy of the intervention without complicating the process. Reliability of the system, ease of integration of disposable and reusable parts, clarity of the visual interface, and intuitive control of the master device or manipulator were key factors in achieving this aim.

The function of the master-slave system presented in this thesis has been demonstrated in vitro. The next step would be to test the system in an in vitro MRI-guided procedure, much like the experiments with the manually steerable needle presented in Chapter 3. The aim of such an experiment would be to demonstrate the function of the system and to evaluate the compatibility of the system as a whole with MRI. After that, two development tracts are of interest. The first tract would consist of registering the needle shape obtained through FBG-based sensing on the MR images, which would provide visual feedback to the physician. A secondary goal of such integration could be to develop imaging sequences that use the spatial information (e.g. position and orientation) obtained with the FBGs for selecting the field of view and the orientation of the imaging planes to maximize the update rate of the MRI without compromising the accuracy of the images. The second tract would consist of extending the current master-slave system to a robotic system with hybrid control in which the manipulations of the physician are complemented by computer-based manipulations. When these steps are finished successfully, the system should be optimized for clinical use and in vitro and in vivo testing can be initiated.

The master-slave system presented in this thesis demonstrates the technical feasibility of integrating steerability and FBG-based tracking in a needle for MRI-guided interventions. The added value of such a system has to be presented convincingly in order for the system to be widely adopted by patients, physicians, and managers. The added value exists of increased accuracy of treatments, improved patient outcomes and reduced treatment times. Technical malfunction and difficulty of use (i.e. incompatibility with current processes, complicated preparations, unclear interfaces) will hamper the success of such a system. Elaborate optimization and extensive testing will be required to tailor the system to suit the needs of specific applications in clinical practice.

9.4 RECENT DEVELOPMENTS: A MANUAL SYSTEM WITH TRACKING

In concurrence with the realization of this thesis, a new project that aims at the integration of steerability and tracking in a needle for application in clinical practice was launched. In this project, the needle is controlled manually, which builds upon the findings with the manually steerable needle presented in Chapter 3. The idea behind this project is that physicians prefer manual control of the needle whenever possible, which is the case in interventions executed in an open-bore MRI or interventions that are guided by means of ultrasound. A combination of steerability and visualization of the needle shape is advantageous, because such a needle can be actively controlled based on clear real-time information about the needle shape.

We developed a third manually steerable needle (Figure 9.1) in which the number of hinges is adjusted to allow for a larger tip angle and to increase tip curvature smoothness compared to the previous prototype. The handle of the needle was adapted to match the increased maximum tip angle and to reduce the number of parts. Further testing with this prototype is necessary for several reasons. Firstly, the performance of steering should be assessed in (animal) tissue to validate the effectiveness of the mechanism in tough and inhomogeneous tissue. Secondly, usability testing is required to assess if the working principle, the design and the control interface are in line with the experience and expectations of the user. Thirdly, the current clinical process should be studied to obtain the full set of boundary conditions and requirements that would lead to successful integration of the new needle in clinical practice.

The approach in this project is to combine the manually steerable needle with the shape sensor consisting of three optical fibers that are integrated in a PVC rod (Figure 9.2). The initial focus will be on the integration of shape sensing with ultrasound images, but integration with MRI may be implemented in a later stage. Adding FBG-based visualization of the needle shape to ultrasound images may be beneficial, because the majority of the ultrasound systems that are currently used in clinical practice provide 2-D images with limited spatial resolution. A major challenge will be to align the spatial information based on the FBG measurements with ultrasound images and to create a visual interface that is easily interpreted by physicians. When the technical function of the steerable needle with shape sensing and the visual interface have both been validated, in vivo experiments in living animals or cadavers can be conducted to demonstrate the added value of a steerable needle with integrated shape sensing. The manually controlled system may be fit for application in clinical practice on a shorter term than the robotic system.

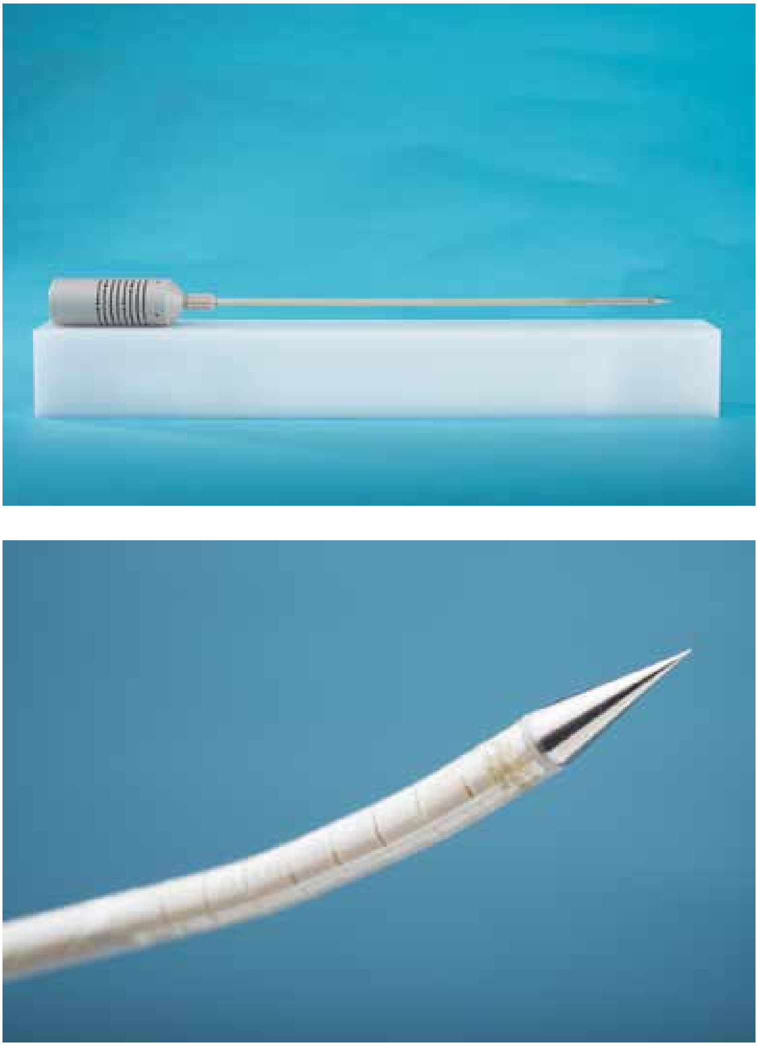

FIGURE 9.1 Latest prototype of steerable needle.

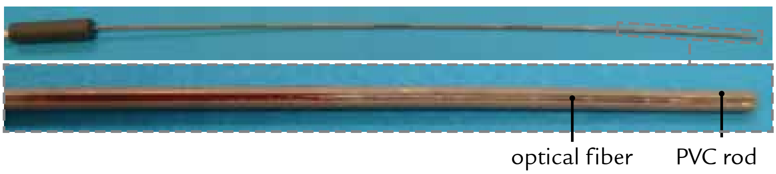

FIGURE 9.2 Shape sensor consisting of a PVC rod with three optical fibers.

9.5 CONCLUSION

The aim of this thesis was to develop 'smart needles' by improving the needles that are used for percutaneous interventions in the liver. The goals and corresponding achievements were the following.

I. The first goal was to develop steerable needles that are compatible with MRI. A concept of needle steering was developed, which was implemented and optimized in three prototypes. The prototypes were technically evaluated and an initial step towards clinical practice was taken by evaluating the second prototype in a clinical environment.
II. The second goal was to develop sensorized needles for spatial tracking and tissue characterization. A methodology for shape sensing based on FBG measurements was identified. The appropriateness of this method was assessed by means of an error analysis and the technical evaluation of multiple prototypes. The third prototype was evaluated in CT to illustrate the function in clinical practice. A first step towards tissue characterization was taken through the development of a FBG-based force sensing needle.
III. The third goal was to integrate steerability and sensors in a robotic needle insertion system. A master slave system for MRI-guided percutaneous needle insertions was developed and demonstrated.

The work presented in this thesis provides a framework for practical implementation of steerability and FBG-based shape sensing in needles that are controlled either manually or robotically. The main contribution of this work is the technological advancement of needles for percutaneous interventions. Future work should aim at the translation of these developments to clinically relevant devices as well as at integration of the devices in the clinical workflow. Development of practicable instruments and methods is vital for successful implementation in clinical practice. The work presented in this thesis will aid in achieving spot-on targeting and optimal therapeutic results in percutaneous liver interventions in the future.

Dankwoord

DANKWOORD

Hoewel alleen mijn naam op de voorkant prijkt, zijn vele anderen betrokken geweest bij de totstandkoming van dit proefschrift. Ik wil graag iedereen die direct of vanaf de zijlijn heeft geholpen hartelijk bedanken voor alle inspanning en goede raad. Een aantal mensen wil ik in het bijzonder bedanken.

John, bedankt voor het aandragen van het project, de fijne werkplek, de goede begeleiding en de gezelligheid. Je bent de beste co-promotor die ik me kon wensen!

Jenny, bedankt voor je adviezen, enthousiasme en vertrouwen als promotor. Ik heb met heel veel plezier in jouw MISIT-groep gewerkt.

Collega's, Arjan, Tim, Dennis, Nick, Linda, Filip, Annetje, Arjo, Marit, Helene, Chunman, Gabriëlle, Hans, Nisse, Andries, Arjan, Diederik, Loubna, Eelko, Nicole, Tom, Edo, Paul, Mona en iedereen die ik vergeten ben, dankjulliewel voor alle gezelligheid tijdens het werken, bij vakgroepuitjes en op congressen.

Anne, dankjewel dat je mij de vakgroep (en de wetenschappelijke wereld) hebt ingelokt. Zonder jou was ik niet aan een promotie begonnen.

Alle mensen die een inhoudelijke bijdrage hebben geleverd aan de technische ontwikkelingen, het wetenschappelijke onderzoek en het schrijven van publicaties, hartelijk dank voor jullie inzet! Ik wil een aantal mensen in het bijzonder bedanken:

- Jules van DEAM; Jurgen, Luca, Marco en Sjoerd van Hemolab; Rolf, Ellen, Iskander en Pim van Technobis; Joris, Peter en Matthijs van het UMC U; Rens en Lun van TNO, bedankt voor jullie bijdrage in het PITON project;
- Cesar, thanks for our fruitful cooperation and your co-authorship;
- Maurits, dank voor de plezierige samenwerking aan de simulaties en bijbehorende publicaties;
- Peter, bedankt voor je medewerking aan de experimenten in MRI en je grote bijdrage als coauteur;
- Adriaan en Camiel, bedankt voor alle klinische input en het beschikbaar stellen van faciliteiten;
- Geert, Mario en Rick, hartelijk bedankt voor het maken van alle prototypes.

Alle studenten die projecten voor mij hebben gedaan, in het bijzonder Mart, Abidemi, Toon en Frank en Roel, bedankt voor jullie inspanning.

Diones en Anouk en later ook Sabrina en Nancy, dank voor alle praktische ondersteuning en gezellige kletspraatjes!

Papa, mama, Tamara en Tom, familie, vriendjes en vriendinnetjes, bedankt voor alle steun, begrip en afleiding. Vanaf nu heb ik weer meer tijd om met jullie leuke dingen te doen.

Femke en Linda, superleuk dat jullie mijn paranimfen wilden zijn! Ik vond het een eer. En natuurlijk bedankt voor alle hulp bij het lay-outen.

Sander, dankjewel voor al je liefde en geduld. Zonder jou (en GAAP) was dit proefschrift er niet gekomen.

About the author

March 31, 1983

Born in Rotterdam, the Netherlands.

1995–2001

Gymnasium at the Norbertuscollege in Roosendaal.

2002–2009

B.Sc. in Mechanical Engineering and M.Sc. in Biomedical Engineering at Delft University of Technology. The master thesis regarded 'Biodegradable high-strength composite for medical implants' and was executed at DSM Biomedical in Geleen.

2009–2010

Researcher at the department of Biomechanical Engineering at the Delft University of Technology.

2010–2014

Ph.D. candidate at the department of Biomechanical Engineering at the Delft University of Technology. The thesis regarded the development of smart needles for percutaneous interventions.

2014–present

Medical physicist in training at the St Antonius hospital in Nieuwegein.